

# Inferring forces from geometry in biology

Thèse de doctorat de l'Université Paris-Saclay  
préparée à l'Université Paris-Sud

École doctorale n°564 Physique en Île-de-France (EDPIF)  
Spécialité de doctorat: Physique

Thèse présentée et soutenue à Orsay, le 21 Novembre 2019, par

**Luca Barberi**

## Composition du Jury :

Aurélien Roux Professeur, Université de Genève Genève, Suisse	Président
Rudolf Podgornik Professeur, University of Ljubljana Ljubljana, Slovénie	Rapporteur
Anđela Šarić Professeur, University College London Londres, Royaume-Uni	Rapporteur
Clément Campillo Maître de conférences, Université d'Evry Val d'Essonne Evry, France	Examineur
Antonio De Simone Professeur, Scuola Internazionale Superiore di Studi Avanzati Trieste, Italie	Examineur
Pierre Sens Directeur de Recherche, Institut Curie Paris, France	Examineur
Martin Lenz Directeur de Recherche, Université Paris-Sud Orsay, France	Directeur de thèse





*"Let's not quarrel about it, Narcissus. You don't see all my struggles either. And I don't know whether or not you are able to understand how I feel when I think that this work will soon be finished, that it will be taken away and set in its place. Then I will hear a few praises and return to a bare workroom, depressed about all the things that I did not achieve in my work, things you others can't even see, and inside I'll feel as robbed and empty as the workshop."*

*"That may be so," said Narcissus. "Neither of us can ever understand the other completely in such things. But there is one realization all men of good will share: in the end our works make us feel ashamed, we have to start out again, and each time the sacrifice has to be made anew."*

*Narcissus and Goldmund, Herman Hesse*



# Acknowledgements

I would have never written this thesis without Martin. In the last three years, Martin has taught me how to think, which is something possibly more profound than physics. Through the numerous discussions we have had in front of the whiteboard in his office, Martin has given me access to some previously unused parts of my brain. I will prove him my gratitude in my future career, by keeping up with the standards for science quality and work ethic that he has set in my head.

I owe a lot also to the fantastic collaborators I have worked with during this adventure. Françoise, Amélie, Aurélien and Joachim have forced me to learn how to both present and defend my theoretical models without making use of equations. Thanks to this tough exercise, I have ended up understanding theory much better!

I have managed to develop many aspects of this work thanks to the inputs of exceptional researchers that I have come across in the last years. I would have never figured out DNA electrostatics without the help of Emmanuel and Ivan, which have explained me strong coupling infinitely many times. Similarly, I owe the parametrization of DNA twisted toroids to Greg Grason and his student, Daria Atkinson, from UPenn.

At this point, I have to admit that CESFO cafeteria has played a major role in my personal growth. By providing awful food, it has redirected all of my attention to the great conversations I could enjoy over lunch, most often with Ananyo, Guglielmo, Giulio and Mehdi.

Although my (very Italian) biological clock did not let me have lunch with them all the time, the gang of PhD students at LPTMS has been so welcoming with me. The memories of the bluesy nights at Samuel's place, the bloody fights during "The Game" and the freezing cold trips to Normandy will always remain in a special place of my heart.

Outside the lab, I have received tons of love from special people around me, that have made me feel home in Paris since my arrival. Some of them deserve a special mention: my French family (Zia Rosanna, Zio Jean-Baptiste, Iris, Samantha and Claude), my sweet flatmates (Ivan, Bartolo and Orazio), my Cité-U buddy Θεανώ, my lovely girlfriend Rachele and the beautiful friends she has brought into my life, like Eleonora and Davide.

Finally, I have to say thank you to my parents and sister, to which I wish I were physically closer than I currently am, for their never-ending love and support.

# Contents

<b>1</b>	<b>Introduction: the springiness of polymers and membranes</b>	<b>8</b>
<b>I</b>	<b>DNA</b>	<b>12</b>
<b>2</b>	<b>A long chain in a small box</b>	<b>13</b>
<b>3</b>	<b>The microscopics of inter-helical adhesion</b>	<b>17</b>
3.1	Some experiments: DNA arrays under osmotic pressure . . . . .	18
3.2	Hydration forces . . . . .	20
3.3	Electrostatic “zipper” . . . . .	22
3.4	From Van der Waals attraction to Wigner crystal matching . . . . .	23
3.5	Ion bridging . . . . .	24
3.6	Bottom line: the importance of being correlated . . . . .	25
<b>4</b>	<b>The geometry of DNA toroids</b>	<b>27</b>
4.1	Generating toroids of controlled size . . . . .	27
4.2	Hexagonal packing, twist and correlations . . . . .	28
4.3	Curvature correlates with inter-helical spacing . . . . .	30
4.4	Summary . . . . .	33
<b>5</b>	<b>Theoretical modeling</b>	<b>34</b>
5.1	Preliminary: how twist redistributes filaments’curvature in DNA toroids	35
5.2	A minimal model of DNA toroid: bending stiffness vs. interactions . . .	39
5.3	Perturbative solution of force-balance equations . . . . .	41
5.4	Fitting the experimental data . . . . .	45
<b>6</b>	<b>Discussion</b>	<b>46</b>
<b>II</b>	<b>ESCRT-III</b>	<b>50</b>
<b>7</b>	<b>Membrane budding away from the cytoplasm</b>	<b>51</b>
<b>8</b>	<b>Experiments</b>	<b>57</b>
8.1	ESCRT-III filaments stabilize helical membrane tubes . . . . .	57
8.2	Polar and equatorial filaments . . . . .	59
8.3	Tube-less helices . . . . .	59
8.4	Summary and relevant data . . . . .	62

<b>9</b>	<b>Theoretical modeling</b>	<b>64</b>
9.1	Preliminary: differential geometry of helical tubes . . . . .	64
9.2	Straight or helical? A phase diagram for membrane tubes . . . . .	66
9.2.1	An instructive failure: helical tubes from high surface tension . .	67
9.2.2	Asymmetric membrane binding of polar and equatorial monomers	68
9.3	Bending and torsional rigidities of ESCRT-III filaments . . . . .	70
9.3.1	A lower bound for bending rigidity and membrane-binding asym-	
	metry . . . . .	72
9.3.2	Realistic estimate of torsional rigidity and membrane-binding	
	asymmetry . . . . .	73
<b>10</b>	<b>Discussion</b>	<b>74</b>
<b>11</b>	<b>Conclusion</b>	<b>78</b>
<b>12</b>	<b>Résumé de la thèse en français</b>	<b>80</b>
	<b>Bibliography</b>	<b>86</b>

# Chapter 1

## Introduction: the springiness of polymers and membranes

*Ut tensio, sic vis*<sup>1</sup>. So wrote Robert Hooke, almost three hundred years ago, to describe the proportionality between the restoring force of a spring and its elongation. Hooke also coined the term “cell”<sup>2</sup>, inspired by the observation of plant cells under the microscope. Could Hooke imagine that cells’ constituents were as springy as his springs? In this thesis, we use the elastic deformation of cells’ constituents in the same way as we would use the elongation of a spring in a dynamometer: to read out forces.

Biological assemblies often owe their stability and evolution to inter-molecular forces on which we have poor prior knowledge. Maybe the main difficulty in modeling such forces is their sensitivity to the chemical composition of the interacting molecules, as well as of their surrounding environment. However, the biological role of inter-molecular forces may be due to just few of their features, that emerge from the underlying chemical complexity. If these forces are critically involved in the deformation of biological matter, we can infer these features by reconciling the deformation geometry with simple mechanical models. We adopt this approach to investigate two such inter-molecular forces. In the rest of this chapter, we provide an outline of the thesis and introduce basic notions on the elasticity of polymers and membranes, which we extensively resort to in the manuscript.

In the first part of the thesis, we investigate the forces exerted by DNA helices onto each other (for a detailed introduction, see Ch. 2). DNA is a negatively charged polymer [Fig. 1.1a], implying that its units tend to repel each other. However, in the presence of multivalent cations, negatively charged DNA helices can attract each other. Attraction between DNA helices is a fascinating phenomenon, whose physical origin is still not completely clear [Ch. 3]. Inter-helical attraction is fundamental to compensate DNA resistance to bending when packing large quantities of DNA in comparatively small environments, such as the nuclei of sperm cells. We study the competition between inter-helical attraction and DNA bending rigidity by looking at the geometry of dense DNA toroidal bundles [Ch. 4], which spontaneously form, *in vitro*, when DNA is in the presence of multivalent cations. Like physiological DNA assemblies, DNA toroids are both tightly packed and curved. Interestingly, geometrical data on DNA toroids show that the more helices are curved, the less tightly packed they are.

---

<sup>1</sup>Robert Hooke, *De Potentia Restitutiva, or of Spring. Explaining the Power of Springing Bodies*, London, 1678.

<sup>2</sup>Robert Hooke, *Micrographia: or some physiological descriptions of minute bodies made by magnifying glasses : with observations and inquiries thereupon*, London, 1667.

To rationalize this experimental evidence, we develop a simple mechanical model in which inter-helical attraction compensates for DNA bending rigidity [Ch. 5]. Our findings suggest that curvature weakens inter-helical attraction [Ch. 6]. To the best of our knowledge, this aspect was overlooked in the previous literature and we think it may be relevant in physiological DNA packings.

What is the energy cost of bending DNA? There are several contributions to DNA stiffness. Base pairs, for instance, are stacked by means of covalent bonds that get stretched as soon as DNA gets bent. Moreover, the charges distributed on DNA surface get closer when DNA gets bent, which costs further energy. Possibly more complicated microscopic contributions could be named. However, when bending happens at much larger scales than the DNA helical pitch ( $\simeq 3$  nm, Fig. 1.1a), meaning that the radius of curvature  $r$  of the DNA central axis satisfies  $r \gg 3$  nm, the elastic response of DNA can be approximated with that of a thin isotropic rod. In this limit, we only need to consider the curvature  $c = 1/r$  of the rod [Fig. 1.1b]. All bending directions are equivalent for isotropic rods, implying that bending energy is even in  $c$ . For small deformations, the local cost of bending is thus proportional to  $c^2$ , and we denote the proportionality coefficient by  $k_b/2$ . The bending stiffness  $k_b$  is generally expressed in terms of the so-called *persistence length*  $\ell_p = k_b/k_B T$ , where  $k_B$  is Boltzmann's constant and  $T$  is temperature.

Persistence length is the typical DNA length above which thermal agitation can significantly bend the chain. To be more precise, imagine having a DNA chain of length  $S$  and constant radius of curvature  $r$ . When  $S \approx \ell_p$ , the thermal energy  $k_B T$  can pay the energy cost of giving the chain a radius of curvature  $r \approx S \approx \ell_p$ ,

$$k_B T = \frac{k_b S}{2r^2} \approx \frac{k_b \ell_p}{2\ell_p^2} \quad (1.1)$$

yielding a dependence of  $\ell_p$  on  $k_b$  and  $k_B T$  consistent with its definition. In solution, a DNA segment much shorter than  $\ell_p$  behaves as a rigid stick, while a DNA segment much larger than  $\ell_p$  is very flexible.

Since entropy participates in DNA rigidity, one generally talks of bending *free energy* (rather than energy). For a chain of length  $S$ , arc length  $s$  and spatially varying curvature, the bending free energy reads:

$$\mathcal{F}_{\text{WLC}} = \frac{k_B T \ell_p}{2} \int_0^S ds [c(s)]^2 \quad (1.2)$$

where the subscript WLC stands for Worm Like Chain, the name of the model we just derived [Phillips et al., 2012].

In the second part of the thesis, we turn to the binding force of a particular protein complex, ESCRT-III, to cellular membranes. ESCRT-III proteins assemble into membrane remodeling polymers that constrict and sever membrane necks from their inner volume. To the best of our knowledge, ESCRT-III is involved in all known biological processes that require such kind of event, ranging from HIV release from the plasma membrane to the constriction of the cytokinetic bridge during cell division (for a detailed introduction, see Ch. 7). Despite their ubiquity, it is still unclear how ESCRT-III polymers shape and sever membrane necks. In vitro, ESCRT-III helical polymers can grow helical tubular protrusions on the surface of spherical membrane vesicles [Ch. 8]. By means of simple mechanical models, we show that helical membrane tubes can result from the positioning of membrane-binding sites on the surface of ESCRT-III polymers relative to their preferred curvature [Ch. 9]. Interestingly, our findings can reconcile two previous models of ESCRT-III membrane remodeling mechanisms [Ch. 10].

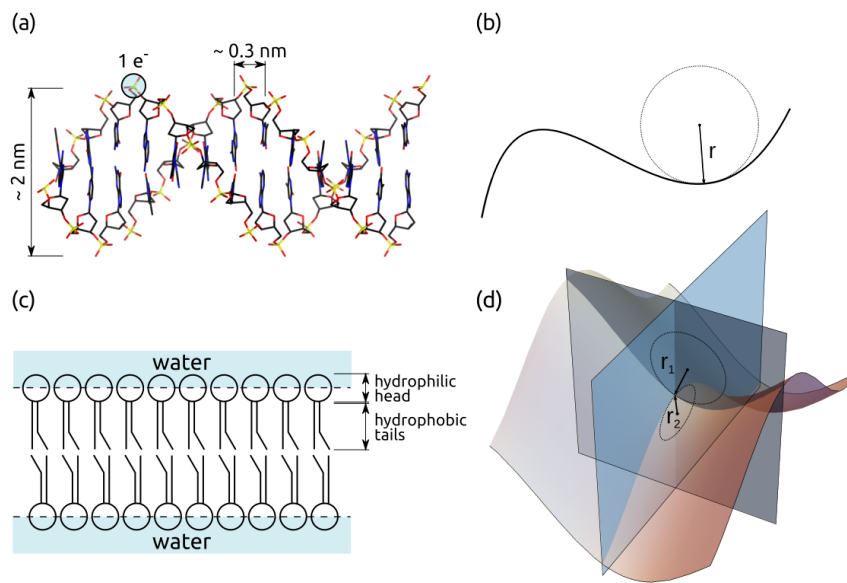


Figure 1.1: **Geometry of DNA and lipid bilayers.** (a) DNA double helix. There is one naked electron ( $1e^-$ ) in correspondence of each *phosphate group* (yellow). Axial rise per base pair ( $\simeq 0.3$  nm) and helix diameter ( $\simeq 2$  nm) estimates from Mandelkern et al. [1981]. Adapted from [https://en.wikipedia.org/wiki/Nucleic\\_acid\\_double\\_helix](https://en.wikipedia.org/wiki/Nucleic_acid_double_helix), authored by Mauroesgueroto and licensed under CC BY-SA 4.0. Labels not present in the original version. (b) Local radius of curvature  $r$  of a space curve. (c) Bilayer of phospholipids. Water is excluded from the tail region. (d) Local principal radii of curvature,  $r_1$  and  $r_2$ , of a surface.

Furthermore, we estimate the membrane-binding force of ESCRT-III monomers by feeding our model with geometrical data on the shape of helical membrane tubes.

What is the cost of deforming a membrane? To answer, we recall what makes membranes stable in the first place. Cellular membranes are mainly composed of *phospholipids*. Phospholipids are small *amphiphilic* molecules, meaning that they comprise a hydrophilic head and two hydrophobic tails. Due to this structure, in water, phospholipids isolate their hydrophobic tails from the aqueous environment by spontaneously assembling into *lipid bilayers* [Fig. 1.1c]: the prototype of cell membranes. Due to the cylindrical shape of phospholipids and their will to stay as laterally packed as possible, bilayers are spontaneously flat. To bend a bilayer, one has to reduce local lipid packing and pay the energy cost associated with the consequent tail exposure to water. Similarly to what we did with DNA, we consider bending deformations at much larger scales than the bilayer's thickness (*i.e.*, few nanometers), such that the membrane surface can be approximated with an infinitely thin sheet. We can further assume that the sheet is liquid, since phospholipids stick together mainly because of their tails' common dislike for water molecules, and are thus relatively mobile with respect to each other. If we consider a membrane that is homogeneous, and symmetric with respect to the middle plane between its two lipid layers, the lowest order of its bending energy is proportional to the square of its total curvature  $2H = 1/r_1 + 1/r_2$ , where  $r_1$  and  $r_2$  are its principal radii of curvature [Fig. 1.1d]. We denote the proportionality coefficient by  $\kappa/2$ . Since we only consider membrane deformations that do not alter the surface topology and that do not involve membrane boundaries, Gaussian curvature  $1/r_1 r_2$  contributes a physically irrelevant constant to the free energy, due to Gauss-Bonnet theorem.

To complete the elastic free energy of a membrane, we need a further contribution related to local surface area variations. When a protrusion grows on the surface of a membrane, like the tubular ones generated by ESCRT-III, the protrusion expands mainly by importing lipids from the surrounding bilayer. This transfer requires working against the tension of the bilayer reservoir, and we denote by  $\sigma$  the energy cost per unit area of the protrusion.

Summarizing, bending and surface energy contributions define the celebrated Helfrich [1973] free energy:

$$\mathcal{F}_{\text{Helfrich}} = \int_{\mathcal{A}} d\mathcal{A} \left[ \frac{\kappa}{2} (2H)^2 + \sigma \right]. \quad (1.3)$$

Eqs. (1.2) and (1.3) constitute the standard results used to formulate the theories presented in this thesis. To deal with the geometry of curves and surfaces, we sometimes resort to differential geometry. We suggest the book of Kreyszig [1991] as an excellent reference on the subject.

Finally, we summarize our results and future perspectives in Ch. 11.

**Part I**  
**DNA**

## Chapter 2

# A long chain in a small box

The nucleus of a human sperm cell can be thought of as a small box, with a linear size of  $5\ \mu\text{m}$  [Fig. 2.1a]. This microscopic box, which could fit ten times in the width of a human hair, can contain a 1 m long DNA chain! 2% of the box volume is occupied by DNA [Phillips et al., 2012] [Fig. 2.1b]. The head (*capsid*) of a *bacteriophage*, a virus that infects bacteria, is an even smaller box, one hundred times smaller than a sperm cell nucleus [Fig. 2.1c]. 60% of a capsid volume is occupied by DNA [Phillips et al., 2012], yielding DNA packings as dense as crystals [Fig. 2.1d]. These numbers become even more impressive when one considers the two main energetic costs associated with DNA packing. First of all, the surface of DNA is negatively charged, meaning that its subunits would like to stay as far apart from each other as possible. Second, it is not possible to pack a long DNA chain in a small box without bending it. The DNA mechanical response becomes especially not negligible in phage capsids, since their diameter is comparable to DNA persistence length. How does nature deal with the formidable task of packing DNA in phage capsids and sperm cells?

Confining DNA in a phage capsid is a work of brute force: a molecular motor, placed at a vertex of the capsid, consumes ATP to push the DNA inside [Smith et al., 2001]. Once the whole viral genome is stored in the capsid, the hole from which it entered closes by joining with the *tail* of the phage, which self-assembles separately from the rest [Fig. 2.1c]. The mechanical and electrostatic pressure accumulated in the packing process is then used to inject DNA in a bacterial victim organism, by expelling DNA from the capsid and making it pass through the tail, which serves as the needle of a syringe. DNA ejection starts when the phage “docks” on the outer membrane of the bacterium, where cell-surface-exposed molecules (known as *receptors*) trigger the opening of the hole from which DNA initially entered. The electrostatic pressure in phage capsids is usually reduced by the presence of positive ions in physiologic conditions, which screen the Coulombic repulsions between DNA helices. Examples of ions found in T-even phages are the *polyamines* spermidine (3+) and putrescine (2+) [Ames et al., 1958; Ames and Dubin, 1960; Tabor and Tabor, 1985].

The role of external positive charges is more dramatic in sperm cells, where repulsions are not only screened, but over-screened, to the point that two negatively charged DNA helices end up attracting each other. Stepping back from sperm cells, we stress here that the physical mechanism by which cations drive inter-helical attraction is not yet fully understood. Probably, several kinds of interaction participate in DNA *condensation*, some of which we will illustrate in Ch. 3. Now going back to sperm cells, we know that in mammals the positive charges responsible for DNA condensation are provided by *protamines*, proteins with a high content of positively charged

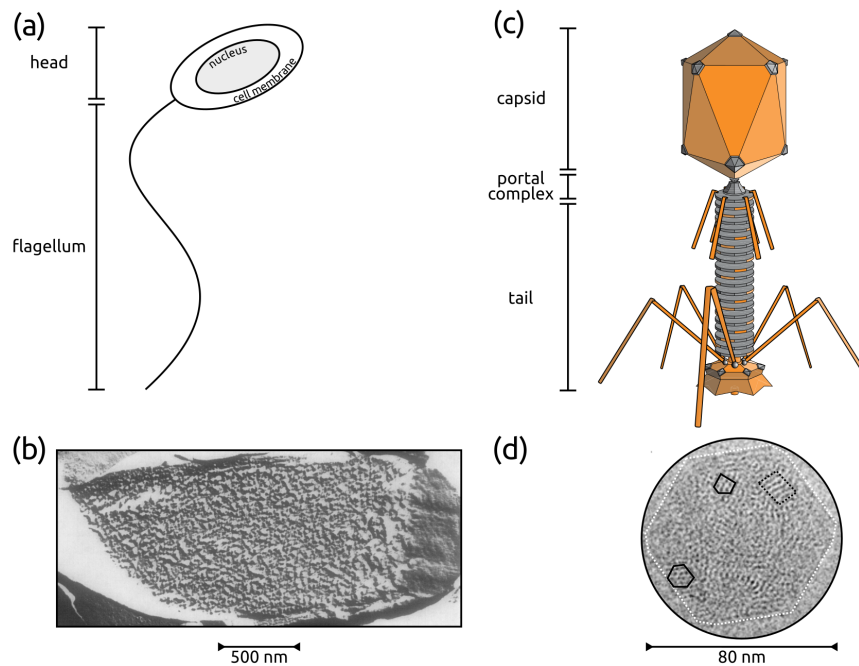


Figure 2.1: **DNA packing in bacteriophages and sperm cells.** (a) Anatomy of a sperm cell. DNA is conserved in the nucleus. (b) Cross fracture of human sperm nuclei, imaged by freeze-etching technique in the electron microscope. Reprinted from Koehler [1972], with permission from Elsevier. (c) Anatomy of a bacteriophage virus. DNA is conserved in the capsid. Figure from <https://en.wikipedia.org/wiki/Bacteriophage>, authored by Adenosine and licensed under CC BY-SA 3.0. Labels not present in the original version. (d) CryoEM micrograph of DNA organization within a phage capsid (dashed white contour). DNA helices appear as black dots (solid black contours) when they are perpendicular to the page, or striations (dashed black contour) when they are parallel to it. Local hexagonal packing can be recognized within solid black contours. Adapted from Leforestier and Livolant [2009], with permission from the authors.

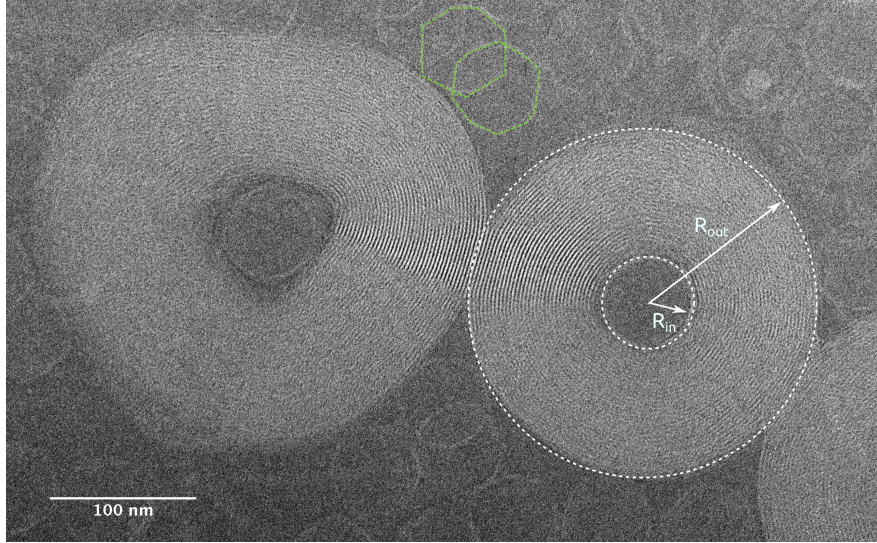


Figure 2.2: **DNA toroidal bundles.** CryoEM micrograph of two toroids made up of multiple DNA helices condensed by spermine (4+). DNA comes from  $\lambda$ -phages, whose empty capsids (green dashed contour) are dispersed in the sample, both around the toroids and at their center. *Courtesy of A. Leforestier and F. Livolant, Laboratoire de Physique des Solides, CNRS, Université Paris Sud, Orsay, France.*

amino-acids. In humans, between 85% and 95% of DNA is condensed by protamines, and the rest of the work is left to *histones* [Balhorn, 2007]. Interestingly, altered concentration of protamines correlates with infertility in mice and humans, suggesting that protamines are key to the correct function of sperm cells [Oliva, 2006].

In this part of the thesis, we use experimental data on the geometry of DNA condensates to infer properties of cation-mediated inter-helical forces. Unfortunately, high resolution imaging of DNA condensates is not possible *in vivo*, because the physiological density of DNA in cells' nuclei is too high (see, e.g. Koehler 1966, 1970, 1972; Koehler et al. 1983) [Fig. 2.1b]. Hence, we use data from DNA condensates realized *in vitro*. *In vitro*, one is free to choose among a set of DNA condensing agents, some of the most commonly used being cobalt hexammine III ( $\text{Co}(\text{NH}_3)_6^{3+}$ ), spermidine (3+), spermine (4+) and protamines [Laemmli, 1975; Chatteraj et al., 1978; Widom and Baldwin, 2004; Hud et al., 1993]. Interestingly, independently of the condensing agent species, DNA generally condenses into hexagonally packed bundles, which can be either toroidal [Fig. 2.2] or straight. Our study focuses on DNA toroidal bundles. Although we do not know whether DNA toroids exist *in vivo* (for instance, in the nuclei of sperm cells) they have at least two features in common with physiological DNA: tight packing and curvature. Therefore, we think that our results may be transferred to biologically relevant cases.

Specifically, we investigate the correlation between DNA packing density and curvature in DNA toroids. This correlation is supported by two recent experimental findings. First, within a DNA toroid of inner radius  $R_{\text{in}}$  and outer radius  $R_{\text{out}}$  [Fig. 2.2], inter-helical spacing decreases going from  $R_{\text{in}}$  to  $R_{\text{out}}$ . Second, average spacing is larger in “small” toroids ( $R_{\text{out}} \leq 40$  nm) than in “giant” ones ( $125 \text{ nm} \leq R_{\text{out}} \leq 175$  nm). We propose a simple mechanical model to interpret the first experimental finding, in which the spacing dependence on position is connected to DNA local curvature (hence, to its local elastic response) and inter-helical forces are assumed to be

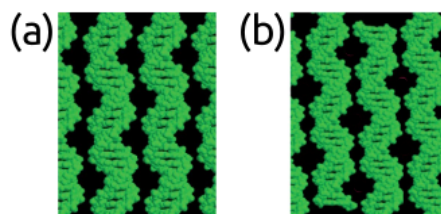


Figure 2.3: **DNA grooves' correlation.** (a) In straight bundles. (b) In toroidal bundles. Adapted from Leforestier and Livolant [2009], with permission from the authors.

curvature independent. This model predicts that small toroids should be, on average, more tightly packed than giant ones, in clear contradiction with the second experimental finding. We speculate that this is due to a dependence of inter-helical forces on curvature.

Why should curvature affect inter-helical forces? A DNA molecule has negative surface charges distributed along its two phosphate helices. Due to this inhomogeneous charge distribution, the interaction between two parallel DNA molecules depends on the spatial correlation between their grooves. High resolution images of spermine-condensed DNA bundles from Leforestier and Livolant [2009] show that curvature alters groove correlation between neighboring helices [Fig. 2.3]. In straight bundles, the major grooves of each helix face the minor grooves of its neighbors [Fig. 2.3b]. Conversely, in toroidal bundles, the major grooves of each helix face the major grooves of its neighbors [Fig. 2.3a]. We think this certifies a non trivial influence of curvature on inter-helical interactions.

In Ch. 3, we substantiate our intuition on the influence of groove correlation on inter-helical forces by proposing a historical review of the microscopic theories that have been developed to understand cation-mediated inter-helical forces. In Ch. 4, we present the experiments that motivate our theoretical study. In Ch. 5, we present our theoretical models. Finally, in Ch. 6, we discuss our results and propose future perspectives.

## Chapter 3

# The microscopics of inter-helical adhesion

### Contents

---

3.1	Some experiments: DNA arrays under osmotic pressure . . . . .	18
3.2	Hydration forces . . . . .	20
3.3	Electrostatic “zipper” . . . . .	22
3.4	From Van der Waals attraction to Wigner crystal matching . . . . .	23
3.5	Ion bridging . . . . .	24
3.6	Bottom line: the importance of being correlated . . . . .	25

---

The goal of this chapter is to provide convincing arguments on the importance of spatial (groove) correlation between neighboring DNA helices for their adhesion. We briefly review the historical development of cation-mediated DNA condensation theories and stress the role played by spatial correlations in each of them. Where possible, we comment on the validity of old models in the light of more recent findings.

In Sec. 3.1, we present some important experiments, conducted between the late eighties and the early nineties, in which inter-helical forces were probed by measuring the response of DNA hexagonal bundles to controlled external pressures, at different ionic conditions. The key finding was that inter-helical forces decay exponentially with the distance at short enough inter-helical separations, with a decay length that is independent of ionic conditions. An analogous behavior was observed between interacting lipid bilayer surfaces, leading some authors think that the force probed in the two cases had a common, non Coulombic origin. In Sec. 3.2, we detail an early theory proposed to rationalize these experimental findings in terms of *hydration* forces. In Sec. 3.3, we present a development of hydration theory in which the ability of DNA helices to *chemisorb* positive ions onto their surface is considered. In Sec. 3.4, we illustrate how the modeling of Coulombic forces evolved to account for cation-mediated inter-helical attraction, starting from Van der Waals like forces, due to the correlated thermal fluctuations of cation clouds surrounding DNA helices, and arriving to the modern theory of *strong coupling*. In Sec. 3.5, we present recent progress made in the modeling of inter-helical forces mediated by dumbbell shaped cations. Finally, in Sec. 3.6, we summarize the lessons learned from the review and comment on the influence of spatial correlations on inter-helical forces.

### 3.1 Some experiments: DNA arrays under osmotic pressure

Maybe the biggest obstacle in the development of predictive theories of DNA condensation is that different cation species behave differently. For example, the critical cation concentration at which DNA condenses is cation-specific, and it does not correlate with valency in a way that we understand. Mono- and di-valent salts are generally unable to condense double-stranded DNA, independently of their concentration. Two exceptions are  $\text{MnCl}_2$  and  $\text{MgCl}_2$ . The first can condense DNA at high temperature or under external pressure [Rau and Parsegian, 1992b], while the second can condense DNA in a solution of water and methanol [Rau and Parsegian, 1992a].

Fortunately, there are some features of the cation-mediated inter-helical forces are not cation-specific, many of which emerged from pioneering experiments performed by Parsegian and coworkers (see, *e.g.* Rau et al. 1984; Rau and Parsegian 1992a; Todd et al. 2008). In their typical experiment, the forces between DNA helices under different ionic conditions are probed by measuring the inter-helical spacing of a DNA hexagonally packed phase under controlled osmotic pressure. In particular, they leverage the fact that DNA phase separates in solutions where polyethylene glycol (PEG) is present. The resulting DNA phase is hexagonally packed, with long-range bond orientational order at separations smaller than  $\simeq 32 \text{ \AA}$  or long-range cholesteric order at larger separations [Podgornik et al., 1996]. Both water and DNA condensing ions freely diffuse in both phases, such that the system can reach osmotic equilibrium. At equilibrium, the distance between DNA helices depends on the ionic conditions, as well as on the osmotic pressure exerted by PEG.

One can construct osmotic pressure vs. spacing curves by varying PEG concentration at different ionic conditions, obtaining plots like those shown in Fig. 3.1. In Figs. 3.1a and 3.1b, ionic conditions are such that DNA does not condense and inter-helical forces are purely repulsive. In this case, inter-helical spacing increases indefinitely with decreasing pressure. Conversely, in Fig. 3.1c, cations drive spontaneous DNA condensation and inter-helical forces are short-range repulsive and long-range attractive. In this case, repulsions and attractions balance out at some cation-specific inter-helical spacing, corresponding to the zero pressure spacings in the plot. In Fig. 3.1d, we show an example of pressure-induced DNA condensation with divalent salt  $\text{MnCl}_2$ . At spacings larger than  $\simeq 30 \text{ \AA}$ ,  $\text{MnCl}_2$  mediates purely repulsive inter-helical forces and the pressure-spacing curve is similar to that obtained with the monovalent salt  $\text{NaCl}$ . At  $\simeq 30 \text{ \AA}$ , something reminiscent of a first order phase transition occurs and the pressure-spacing curve assumes a behavior similar to that registered with cobalt hexamine III.

Notice that, at spacings smaller than  $\simeq 30 \text{ \AA}$ , pressure decays exponentially with a decay length between  $1.5 \text{ \AA}$ , when DNA is condensed, and  $3 \text{ \AA}$ , when DNA is not condensed [Figs. 3.1a, 3.1b, 3.1c]. Due to the weak dependence of this decay length on cation valency and concentration, Rau et al. [1984]; Rau and Parsegian [1992a] argued that the forces they probed were not standard electrostatic ones, because these were predicted to decay with a screening length proportional to ionic strength by the electrostatic double layer theory [Levin, 2002]. Hence, they proposed to rationalize their findings in the framework of hydration forces.

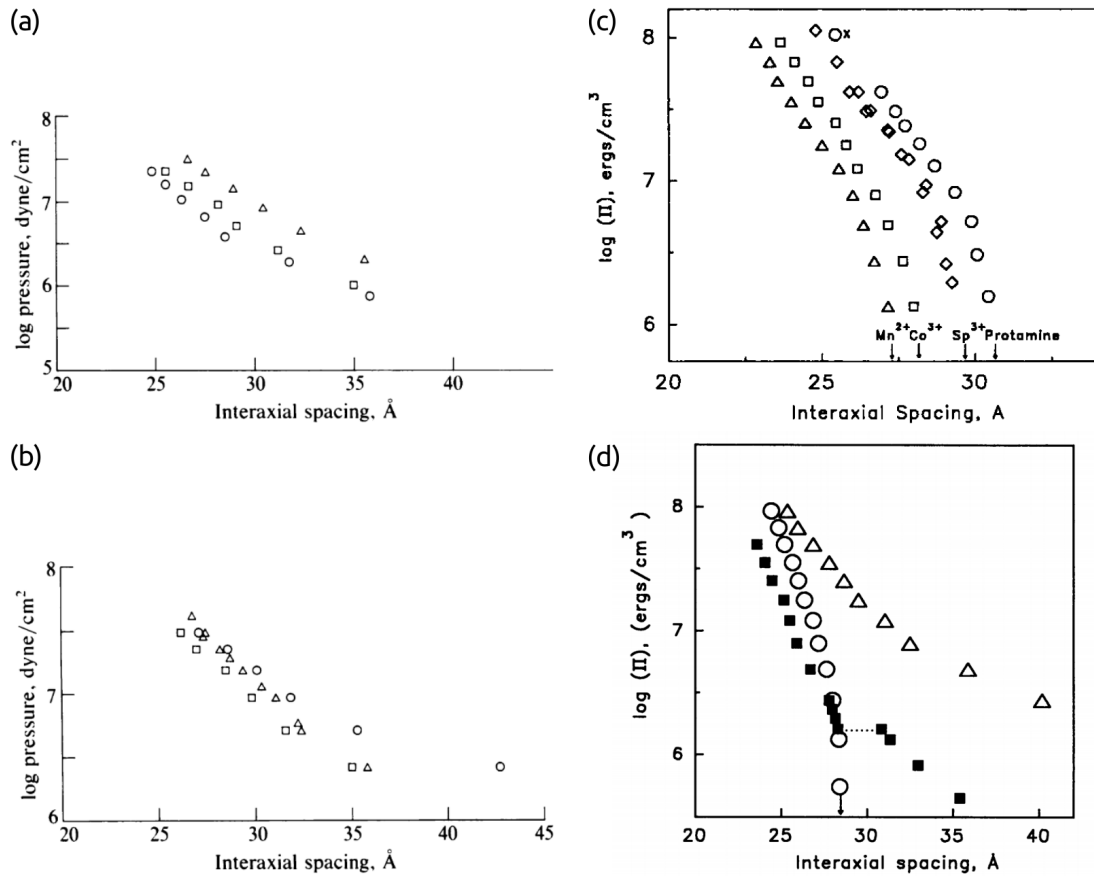


Figure 3.1: **Pressure vs. inter-helical spacing in osmotic stress experiments on DNA hexagonal arrays.** (a,b) Cationic conditions in which DNA is not condensed. Decay length at small separations is  $\simeq 3 \text{ \AA}$  independently of ionic species and concentration. (a) Divalent cations. ( $\square$ ) 25 mM  $\text{MgCl}_2$ . ( $\circ$ ) 25 mM  $\text{CaCl}_2$ . ( $\Delta$ ) 10 mM putrescine. (b) Monovalent cations. 0.5 mM ( $\circ$ )  $\text{LiCl}$ , ( $\Delta$ )  $\text{NaCl}$ , ( $\circ$ )  $\text{CsCl}$ . *Reproduced from Rau et al. [1984], with implicit permission from the National Academy of Sciences.* (c) Cationic conditions in which DNA is spontaneously condensed. Arrows indicate the spontaneous spacing at zero applied pressure. The decay length at small separations is  $1.4 \pm 0.1 \text{ \AA}$  at all ionic conditions. ( $\circ$ ) Salmon protamine, 10 mM  $\text{TrisCl}$  (pH 7.5). ( $\diamond$ ) 2 mM spermine (3+), 0.1 M  $\text{NaCl}$ , 10 mM  $\text{TrisCl}$ . ( $\square$ ) 5 mM  $\text{Co}(\text{NH}_3)_6\text{Cl}_3$ , 0.1 M  $\text{NaCl}$ , 10 mM  $\text{TrisCl}$ . ( $\Delta$ ) 150 mM  $\text{Mn}(\text{ClO}_4)_2$ , 10 mM  $\text{TrisCl}$ . *Reprinted from Rau and Parsegian [1992a], with permission from Elsevier.* (d) Comparison of different ionic conditions. ( $\Delta$ ) 0.5 M  $\text{NaCl}$ , 10 mM  $\text{TrisCl}$ , 1 mM  $\text{EDTA}$ . DNA is not condensed, inter-helical forces are purely repulsive. Decay length is  $3 \text{ \AA}$  at small separations. ( $\circ$ ) 5 mM  $\text{Co}(\text{NH}_3)_6\text{Cl}_3$ , 0.1 M, 10 mM  $\text{TrisCl}$ . DNA is spontaneously condensed, inter-helical forces are attractive at long distances. The arrow indicates spontaneous spacing at zero pressure. Decay length is  $1.5 \text{ \AA}$  at small separations. ( $\blacksquare$ ) 50 mM  $\text{MnCl}_2$ , 10 mM  $\text{TrisCl}$ . DNA is not spontaneously condensed. At low pressures, interactions are purely repulsive. At high pressures, DNA condenses and interactions become attractive at large separations. *Reprinted from Rau and Parsegian [1992b], with permission from Elsevier.*

## 3.2 Hydration forces

The onset of exponential repulsions at separations shorter than  $30 \text{ \AA}$ , with salt-independent  $1 - 3 \text{ \AA}$  decay lengths was also found between lipid bilayer surfaces separated by water (for a review, see Rand and Parsegian 1989). This repulsion, first observed between zwitterionic lecithin bilayers [Leneveu et al., 1976], was also reported between uncharged [McIntosh et al., 1989] and charged lipid membranes, overwhelming the coulombic repulsion of these latter at small enough separations [Cowley et al., 1978].

These findings were first rationalized by Marčelja and Radić [1976], who suggested that a repulsive non Coulombic interaction may originate from the ordering of water molecules in the proximities of membrane polar surfaces. They supported their hypothesis with a phenomenological model, that we detail below. Given the striking similarity between the behavior of membranes and DNA helices, Parsegian and coworkers adapted Marčelja’s model to interpret their osmotic stress experiments on DNA arrays [Rau and Parsegian, 1992a; Leikin et al., 1993].

Before presenting the details of Marčelja’s model, we explain its fundamental physics in words. Bulk water molecules organize into a hydrogen bond network. A polar surface, like that of DNA or a lipid bilayer, can perturb this network. In fact, suppose a water molecule is close to one of the naked charges provided by DNA phosphate groups. The slightly positively charged hydrogen atoms of water feel attracted to DNA phosphates, resulting in a local polarization of water molecules. Notice that naked electric charges are not required to structure water. DNA grooves’ base atoms, for example, can form hydrogen bonds with water molecules, thus participating in the water hydrogen bond network. Polarization is just one possible form local water ordering. Other possibilities are, for example, the density, positional order and tetrahedral coordination of water molecules. Atomistic simulations with explicit solvent represent a particularly useful tool in the study of water structuring phenomena [Zavadlav et al., 2017]. The perturbation in water structure generated by a polar surface can propagate away from the surface, up to a certain distance, thanks to the ability of water molecules to order each other by forming hydrogen bonds. What happens when the perturbations emanating from two close-by polar surfaces overlap? There are two possibilities. If the perturbations weaken each other, then water structuring mediates a repulsion between the polar surfaces. Conversely, if the two perturbations reinforce each other, then water structuring mediates attraction. Interestingly, some experiments supported the existence of attractive hydration forces both between bilayers [Rand et al., 1988] and DNA helices [Rau and Parsegian, 1992a]. Two recent simulations supported the emergence of water-structuring repulsions as strong as Coulombic ones at short inter-helical spacings [Yoo and Aksimentiev, 2016; Zavadlav et al., 2017]. In particular, Zavadlav et al. [2017] reported a correlation between the emergence of hydration repulsion and the structuring of water molecules in the interstitial region between DNA helices, using different definitions of water order. None of the simulations registered attractive hydration forces.

We now derive the hydration pressure between two planar parallel surfaces *à la* Marčelja and Radić [1976]. We call  $x$  the axis normal to the planes, whose respective coordinates are  $x = -d/2$  and  $x = d/2$ . We relegate all the information about local water ordering to a scalar order parameter,  $\eta(x)$ . This is obviously a simplifying assumption, since one could introduce more complex vectorial or tensorial order parameters instead [Zavadlav et al., 2017]. However, our current goal is to predict a salt-independent exponential pressure with minimal assumptions on the order pa-

parameter. We assume that the two surfaces impose the same ordering to the water molecules they are in contact with, *i.e.*  $\eta(d/2) = -\eta(-d/2) = \eta_0$ . For example, if  $\eta$  represented water polarization along the  $x$  axis and the two surfaces had a naked negative charge, these boundary conditions would correspond to the slightly negatively charged oxygen atoms of water molecules orienting away from the nearest surface. Water structuring propagates in the bulk, up to some typical distance  $\xi_0$  from each plate, which is the correlation length of  $\eta(x)$ . We assume that water is weakly ordered in the bulk, such that we can approximate the excess free energy  $\Delta F$  due to the water ordering with a Landau-like quadratic expansion in powers of  $\eta$ . With the proper choice of units, we can write

$$\Delta F[\eta, \eta'] = \int_{-d/2}^{d/2} dx \left\{ \eta^2 + \xi_0^2 (\eta')^2 + \mathcal{O}(\eta^3) \right\}, \quad (3.1)$$

in which the prime denotes differentiation with respect to  $x$ . Notice that we can neglect higher order derivatives by assuming that the order parameter has smooth spatial variations. The stationarity of  $\Delta F$  relative to  $\eta$  boils down to

$$\eta'' = \xi_0^{-2} \eta, \quad (3.2)$$

which is solved for

$$\eta_{\text{eq}}(x) = \eta_0 \frac{\sinh(x/\xi_0)}{\sinh(d/2\xi_0)}. \quad (3.3)$$

At equilibrium, the pressure  $P(d)$  between the plates is

$$P(d) \propto -\frac{\partial}{\partial d} \Delta F_{\text{eq}} = \frac{\eta_0^2}{\sinh^2(d/2\xi_0)}, \quad (3.4)$$

where  $\Delta F_{\text{eq}} = \Delta F[\eta_{\text{eq}}, \eta'_{\text{eq}}] = 2\xi_0\eta_0^2 \coth(d/2\xi_0)$  is the excess free energy at equilibrium.

We have obtained a positive pressure, *i.e.* a net repulsive hydration force between the two plates. Coherent with the experiments, the pressure decays exponentially at large enough inter-surface separations,  $P(d \ll \xi_0) \approx e^{-d/\xi_0}$ . The decay length is a property of water only, and can be experimentally estimated as  $\xi_0 \simeq 4 \text{ \AA}$  [Xie et al., 1993]. This value of decay length is slightly larger than that measured in osmotic stress experiments between DNA helices [Sec. 3.1]. However, Rau and Parsegian [1992a] pointed out that such discrepancy may be just an effect of the DNA cylindrical geometry, which generates a hydration pressure that is expressed in terms of Bessel functions rather than simple exponentials. The fact that we obtain a repulsive hydration interaction is a direct consequence of our choice of boundary conditions. In fact, the choice  $\eta(d/2) = -\eta(-d/2)$  implies that the two perturbations emanating from the plates have opposite sign, and therefore weaken each other. Conversely, if we choose two complementary boundaries ( $\eta(d/2) = \eta(-d/2)$ ), the theory above predicts a negative pressure, *i.e.* an attractive hydration interaction.

How can the spatial correlation between neighboring helices affect their hydration interaction? As we illustrated earlier in this section, the surface of DNA is inhomogeneous, since it is made of different *solvated groups*: *e.g.*, negatively charged phosphates and grooves' base atoms. This inhomogeneity is arguably reflected in the perturbation emanating from the helix, which we expect to vary along the helical axis. Depending on how two neighboring helices are aligned, the overlap between emanating perturbations can change, yielding mixed attractive and repulsive contributions (see, *e.g.* Kornyshev and Leikin 1989).

### 3.3 Electrostatic “zipper”

**Disclaimer.** *This and the next sections deal with the crucial ability of DNA to trap some of the positive charges dispersed in the environment within a thin layer close to its surface, by virtue of its elevated surface charge density. We should stress that there are two kinds of positive charges: those coming from the dissociation of DNA phosphate groups and those coming from the dissociation of salt. Making analytical predictions of this phenomenon, known as Manning condensation [Manning, 1969], proves particularly hard in the presence of salt (see, e.g. Trizac and Téllez 2006). However, since salt is necessary for DNA condensation, we cannot pretend it is absent in the following. We then keep the discussion to a qualitative level, relying more on indications provided by experiments and simulations rather than by analytical models.*

Marčelja’s theory yields a linear, second order differential equation for the order parameter  $\eta$  that governs the equilibrium state [Eq. (3.2)]. Interestingly, a one-to-one mapping exists between this and the renowned linearized Poisson-Boltzmann (PB), or Debye-Hückel (DH), equation of screened electrostatics, in which the electrostatic potential plays the role of  $\eta$  and the Debye length that of the correlation length  $\zeta_0$ . Although built upon different physical mechanisms, both Marčelja’s and DH theory rely on the existence of a mean field that mediates the relevant interaction.

Technically speaking, the conditions of validity of DH are not met in DNA arrays. DH was developed for situations in which the electrostatic energy is weak compared to thermal energy. While this is always true at large enough distances from any charged surface, DNA surface charge density proves too high for DH to hold in the typical range of inter-helical separations of DNA bundles.

One dramatic consequence of the elevated DNA surface charge density is that positive ions tend to dress the negatively charged helix by forming a dense cloud around it. This is a nonlinear effect of PB theory, not predicted in the linear DH regime. In the early days of DNA electrostatic theories, DH was corrected so as to account for ion condensation around the helix [Oosawa, 1968]. In this approach, pioneered by Manning [1969], the nonlinearity is relegated to a renormalization of DNA charge, which is effectively reduced by the condensed ion cloud. The interaction between the DNA helix with renormalized charge and non-condensed ions in the environment is then modeled with DH.

From Manning’s perspective, it is for merely electrostatic reasons that some positive ions condense around the negatively charged DNA helix: keeping opposite charges spatially separated would cost a lot of energy. However, DNA can also trap (*chemisorb*) ions via hydrogen bonds. In fact, the highly valent cations that drive DNA condensation are often dressed by a cloud of water molecules (also said *solvation shell*), which can form hydrogen bonds with DNA base atoms. This idea is supported by experiments and simulations, from which it appears that different cation species have different preferential binding sites along the DNA surface, some of which are located within the electrically neutral grooves (for a review, see e.g. Egli 2002).

Kornyshev and Leikin [1999] have developed a theory of DNA condensation in which helices adsorb positive ions essentially through chemisorption. In their model, DNA molecules have a fixed distribution of negative and positive charges along their backbone, from phosphates and chemisorbed cations respectively. In particular, ions can chemisorb in three locations: along phosphate helices, in minor grooves or major ones. The ion densities at each of these locations are free parameters of the theory. Two DNA helices with chemisorbed positive ions can adhere by matching their charge

distributions, forming what the authors call an electrostatic “zipper”. This theory is thus all about inter-helical spatial correlations. Since the interaction between DNA helices and any non chemisorbed charge is modeled with DH, Kornyshev’s model is mathematically equivalent to Marčelja’s one. As a consequence, the two models make qualitatively similar predictions (as Kornyshev and Leikin [1997] themselves pointed out).

### 3.4 From Van der Waals attraction to Wigner crystal matching

In the model described at the end of the previous section, the ions condensed on the surface of DNA are assumed to be static. However, we know that the cloud of condensed ions is a quite dynamic environment. Due to thermal agitation, ions have finite residence times at their binding positions [Egli, 2002; Yoo and Aksimentiev, 2016; Zavadlav et al., 2017].

Correlated thermal fluctuations between the ion clouds of neighboring DNA helices can generate attractions *à la* Van der Waals. In the context of rod-like macromolecules, this mechanism was first rationalized by Oosawa [1968], who modeled the condensed ion clouds dressing DNA molecules as ideal gases, including their density fluctuations as Gaussian corrections to a mean field (PB) theory. With his approach, Oosawa obtained an attractive pair potential, suitable at large inter-helical separations, which is inversely proportional to the square of the separation and that increases linearly with temperature for macromolecules of high enough surface charge. The applicability of Oosawa’s result to DNA arrays was long debated. Podgornik and Parsegian [1998] pointed out that the interactions resulting from correlated fluctuations between ideal-gas like ion clouds are not pairwise additive in DNA arrays, due to the long-range of Coulomb potential, except in the presence of high amounts of salt.

However, the mean field (PB) hypothesis of ion clouds behaving like ideal gases was questioned with time. Simulations suggested that ion clouds around DNA helices looked more like a correlated liquid (or even a crystal, at low enough temperatures) than an uncorrelated gas [Rouzina and Bloomfield, 1996; Grønbech-Jensen et al., 1997]. On this basis, it was proposed that the Coulombic repulsion between ions can be much larger than thermal energy, creating the conditions for their crystallization on the negative background provided by DNA (like in the jellium model of solid state physics). The regime of temperature and ion valency in which ion-ion correlations emerge is known in the literature as strong coupling (SC) regime. The opposite regime is known as the weak coupling (WC) one, in which thermal agitation dominates ion-ion Coulombic repulsions and the uncorrelated mean field (PB) approximation holds (for a review, see Naji et al. 2013).

In a famous paper, Shklovskii [1999a] rationalized the behavior of  $Z$ -valent positive counter-ions within a maximum density bundle of parallel, cylindrical macroions of radius  $r$ , length  $L \gg r$ , and linear charge density  $e/b$ ,  $e$  being the electron charge. He introduced the dimension-less parameter  $Zb/r$  and argued that two limiting cases exist, depending whether  $Zb/r \gg 1$  or  $\ll 1$ . When  $Zb/r \gg 1$ , *i.e.*, cylinders are thin and weakly charged, then sufficiently packed macroions create an uniform negatively charged background, in which positive ions can form a three-dimensional *Wigner crystal* [Wigner, 1934]. Since the crystal exists thanks to long-range inter-ion Coulombic repulsions, the interactions responsible for the stability of the bundle are not pair-wise additive in this case. When  $Zb/r \ll 1$ , macroions are thick and highly charged and positive ions can crystallize on their surfaces. If the cylinders are uniformly charged,

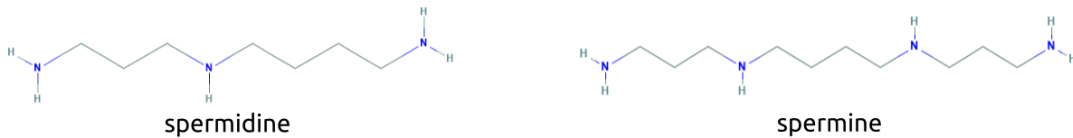


Figure 3.2: **Chemical structure of spermidine and spermine.** Figures from National Center for Biotechnology Information. PubChem Database. *Spermidine*, CID=1102 and *Spermine*, CID=1103.

the result is a two-dimensional Wigner crystal lying on a cylinder. If the cylinders have their negative charges located along helices, like the DNA phosphates, then the positive ions condense onto the helices, forming one-dimensional Wigner crystals. In both cases, two neighboring cylinders can adhere by matching their surface ion crystals. In fact, an ion shared by two crystals is in a deeper potential well than an ion belonging to a single crystal. By virtue of this surface-crystal matching mechanism, the interactions responsible for the bundle stability are pairwise additive in this case.

Assuming DNA is a cylinder of radius 1 nm and homogeneous linear charge density  $1/b = 1/(0.17 \text{ nm})$  [Fig. 1.1a], we have that ions with valency  $Z = 6$  are required for  $Zb/r \simeq 1$ . This implies that  $Zb/r \ll 1$  is the relevant regime in DNA arrays, in which inter-helical adhesion is thus expected to rely on the matching of surface ion crystals, which requires precise inter-helical spatial correlations. On a cautionary note, we should stress that Wigner crystals represent a zero-temperature ground state and are not expected in real DNA condensates. Rather, one can expect ions to arrange into two-dimensional correlated liquids in between DNA helices, which proves enough to mediate attraction [Rouzina and Bloomfield, 1996; Shklovskii, 1999a,b]. Interestingly the structuring of ions around DNA was predicted to overscreen its charge, giving it an effective (renormalized) positive charge [Shklovskii, 1999b; Nguyen et al., 2000], something that was later verified by measuring the electrophoretic mobility of condensed DNA [Besteman et al., 2007]. Charge inversion is not predicted by the earlier theory of Manning [1969], which further underlines the important role of ion structuring in the context of DNA condensation.

### 3.5 Ion bridging

So far, we mentioned DNA condensation theories based on the assumption that the positive ions driving DNA condensation are point-like. Actually, some common DNA condensing agents, like spermine (4+) and spermidine (3+), are elongated [Fig. 3.2]. Since such dumbbell-shaped cations have naked charges at their ends, they can bind each of their ends to a different DNA molecule, thus mediating attraction by *bridging*.

If ion bridging were the major contribution to DNA condensation, one would expect the equilibrium inter-helical spacing to strongly correlate with ion size. Although such correlation seemed to be supported by an early X-ray diffraction study performed by Schellman and Parthasarathy [1984] on DNA condensates stabilized by dumbbell-shaped cations of variable size, Rau and Parsegian [1992a] have later proposed two experimental arguments against ion bridging. The first argument was based on the fact that, in a solution of water and methanol at 25% concentration,  $\text{Mg}^{2+}$  can make DNA condense at an equilibrium spacing (32 Å) slightly larger than that imposed by spermidine at the same methanol concentration (28 Å), regardless of spermidine being a  $\simeq 10 \text{ Å}$  long dumbbell and  $\text{Mg}^{2+}$  an atom. Moreover, the equi-

librium spacing was shown to decrease of several angstroms at increasing methanol concentrations for a given condensing ion. The second argument was that different ion bridges should respond differently to external compression, whereas a common  $\simeq 1.5 \text{ \AA}$  exponential repulsion was registered with condensing agents of various nature at inter-helical distances smaller than their equilibrium values [Fig. 3.1c].

Both arguments, especially the second one, seem to originate from the intuition that the hypothetical ion bridges are perpendicular to the DNA helical axis. However, recent analytical and numerical studies have shed light on a more complex phenomenology of elongated DNA condensing ions [Kim et al., 2008; Cha et al., 2018]. In particular, dumbbell-shaped cations are predicted to serve as perpendicular bridges in the WC regime, in which point-like ions would not mediate attraction because of the absence of ion-ion correlations. In this case, the predicted equilibrium spacing between DNA helices is close to dumbbell size. Conversely, in the SC regime, dumbbells orient parallel to the DNA axis and form a correlated liquid as point-like ions would. In this case, the predicted equilibrium spacing between DNA helices is shorter than dumbbell size.

Recent atomistic simulations of either spermine- or spermidine-condensed DNA arrays have provided evidence in favor of ion bridging. Yoo and Aksimentiev [2016] have shown that, in spermine-condensed DNA arrays, only those spermine molecules found in the interstitial region between neighboring helices contribute to inter-helical attraction, whereas those adsorbed onto the surface of one DNA molecule do not. Zavadlav et al. [2017] have shown that, in spermidine-condensed DNA arrays, lateral inter-helical correlations fluctuate much less than in the absence of spermidine. In their simulation, lateral correlations can fluctuate either because of the rotation of individual base pairs around the helical axis, either because of vertical translations of the whole DNA helices. Weakened rotational fluctuations of DNA molecules around their axis were interpreted as the effect of spermidine acting as an “azimuthal lock” between neighboring DNA molecules. If this is true, then ion bridging implies a certain alignment of neighboring helices, yielding inter-helical spatial correlations.

### 3.6 Bottom line: the importance of being correlated

To conclude this chapter, we briefly summarize why inter-helical lateral correlations can influence the strength of adhesive forces.

In Sec. 3.2, we show that water ordering in the interstitial space between two DNA helices can, in principle, give rise to both attractive and repulsive interactions. In this framework, the competition between attraction and repulsion depends on the overlap between the perturbations to water ordering emanating from the two helices. Since helices are composed of alternating solvated groups of different nature along their length, the way two helices are aligned influences their net interaction.

In Sec. 3.3, we show that positive ions can chemisorb at specific sites along a DNA helix. As a result, the surface charge of a DNA molecule can become a spatially periodic pattern of positive and negative charges. Two DNA helices can adhere by forming an electrostatic zipper, in which the positive charges of one helix face the negative charges of the other. Clearly, this requires that the two helices are properly aligned relative to each other.

In Sec. 3.4, we show that the DNA negative surface charge density is so high that positive ions can condense in its vicinity and form a two- or one-dimensional correlated liquid around a DNA helix. Two DNA helices can attract each other by matching

the correlated ion liquids surrounding them. Since negative charges are not homogeneously distributed along the DNA surface, the ion liquid is probably more strongly structured along the phosphates than far from them. Hence, once again, depending on how two DNA helices are laterally correlated they can match their charge distributions more or less easily.

Finally, in Sec. 3.5, we show that dumbbell shaped condensing ions like spermidine and spermine can mediate inter-helical adhesion by creating ionic bridges between them. One can imagine that the ends of a dumbbell ion have preferred anchoring sites on the surface of a DNA molecule. In fact, numerical simulations suggest that such ion bridges can act as azimuthal locks, promoting spatial correlations between bridged helices.

## Chapter 4

# The geometry of DNA toroids

### Contents

---

4.1	Generating toroids of controlled size . . . . .	27
4.2	Hexagonal packing, twist and correlations . . . . .	28
4.3	Curvature correlates with inter-helical spacing . . . . .	30
4.4	Summary . . . . .	33

---

In this chapter, we illustrate the experiments that motivate our research. Unless stated otherwise, these were conducted by Amélie Leforestier and Françoise Livolant at the Laboratoire de Physique des Solides in Orsay, France. The goal of these experiments is to reconstruct the three-dimensional architecture of DNA toroids. The condensing agent used in the experiments was spermine. To test the robustness of our findings relative to ionic strength variations, experiments were performed at both 4 mM or 40 mM spermine concentration. For reasons that we clarify in the next section, the following cation cocktail had to be present in the samples: 10 mM Tris, 100 mM NaCl, 1 mM MgCl<sub>2</sub>, 1 mM CaCl<sub>2</sub>.

In Sec. 4.1, we present how DNA toroids of variable sizes can be generated by using bacteriophage capsids. In Sec. 4.2, we illustrate known geometrical features of DNA toroids, namely: the hexagonal packing of DNA helices, their collective twist around the toroid center line and the lateral groove correlations between neighboring helices. Finally, in Sec. 4.3, we present recent measurements pertaining the dependence of inter-helical spacing on curvature in toroids.

The data in Secs. 4.1 and 4.3 are still unpublished, while those in Sec. 4.2 are available in Leforestier and Livolant [2009].

### 4.1 Generating toroids of controlled size

In a sample where multiple DNA helices are in the presence of spermine at high enough concentration, multiple DNA toroids can form. DNA toroids tend to aggregate into clusters, which limits the structural analysis of individual toroids under the electron microscope. To prevent toroid clustering, Leforestier and Livolant [2009] proposed the clever strategy of isolating individual toroids in phage capsids. The idea is to use a capsid as a semipermeable cage, in which DNA is trapped while water and ions are free to flow through its walls.

Additionally, this technique allows to generate toroids of variable size, either confined in the capsids or outside them. In the presence of the phage protein receptor

[Sec. 2], DNA is spontaneously ejected from the capsid. The ejection is primarily driven by the pressure difference inside and outside the capsid. The presence of spermine, which diffuses through the capsid, reduces the inner pressure, which is expected to limit the amount of ejected DNA. However the ejected segment condenses into a toroid outside the capsid that exerts a pulling force that drives the DNA transfer to completion [De Frutos et al., 2005]. If DNase is added, this external unprotected segment is degraded and the pulling force suppressed. The ejection stops when the force due to internal pressurization drops down to zero [De Frutos et al., 2005; Evilevitch et al., 2003], leading to partially filled capsids. It is thus possible to dispose of populations of DNA toroids outside (fully transferred out) or inside (trapped in after partial ejection) capsids, by adding or not DNAase at different times.

In the absence of DNase, giant toroids form from many molecules ejected by a group of phages [Fig. 4.1a]. These toroids tend to aggregate and form chains or even large compact clusters at 4 mM spermine (not illustrated). This impedes a proper visualisation of individual toroids that are more easily analyzed in the presence of 40 mM spermine, where the aggregation is reduced. Giant toroids are relatively monodisperse. Their outer radius  $R_{\text{out}}$  varies from 125 to 175 nm (average value of  $144 \pm 15$  nm). Toroids may be trapped with different orientations, allowing the visualization of top [Figs. 4.1a, 4.1b] and side views [Fig. 4.1d]. Side views reveal that they are generally not “true” tori with circular sections, but rather hollow cylinders, as already reported by [Lambert et al., 2000], or cone-shaped barrels, whose heights vary from 130 to 250 nm ( $190 \pm 30$  nm) (not illustrated). In most cases, a viral capsid is found within the toroid central hole and serves as a scaffold around which the toroid organizes. The internal radius  $R_{\text{in}}$  is therefore imposed by the capsid, whose “radius” is 40 nm for the T5 phages used in the experiments (leading to  $R_{\text{in}} = 42 \pm 2.5$  nm).

In the presence of DNase, small toroids, confined within capsids [Fig. 4.1b], form after partial ejection. These are made of a single DNA molecule, corresponding to a segment of the phage genome trapped in the capsid. Here, the toroid outer radius  $R_{\text{out}}$  is imposed by the capsid, leading to outer radii in the range of 36 – 37 nm. Inner radii vary from 7 to 20 nm.

It is thus possible to prepare toroids with a wide range of well defined sizes and access curved DNA configurations with radii of curvature varying continuously from 7 to 175 nm. In giant toroids, the inner radius is fixed, while the outer one is free. The reverse situation occurs in small confined toroids, where the inner radius is free, while the outer one is fixed.

## 4.2 Hexagonal packing, twist and correlations

Looking at a toroid from the side, its cross-sections reveal local hexagonal packing of neighboring helices [Fig. 4.1e]. Looking at a toroid from the top, we identify striated domains alternating with blurry ones [Fig. 4.1c]. Striated domains are expected when the helices’ hexagonal lattice is favorably oriented relative to the direction of observation. Blurred domains are expected when the lattice is not favorably oriented. In theory, two kinds of striations could be observed, associated to the lattice vectors  $\theta_2$  [Fig. 4.1g] and  $T_2$  [Fig. 4.1h]. Imaging conditions in the experiments only allow the observation of the  $T_2$  kind of striations. Blurry domains are thus associated to all crystal orientations different from  $T_2$ , meaning that the crystal undergoes a  $60^\circ$  rotation within each blurry domain. The lattice rotates very little within striated domains, because few degrees would be enough to lose the periodicity along the direction of

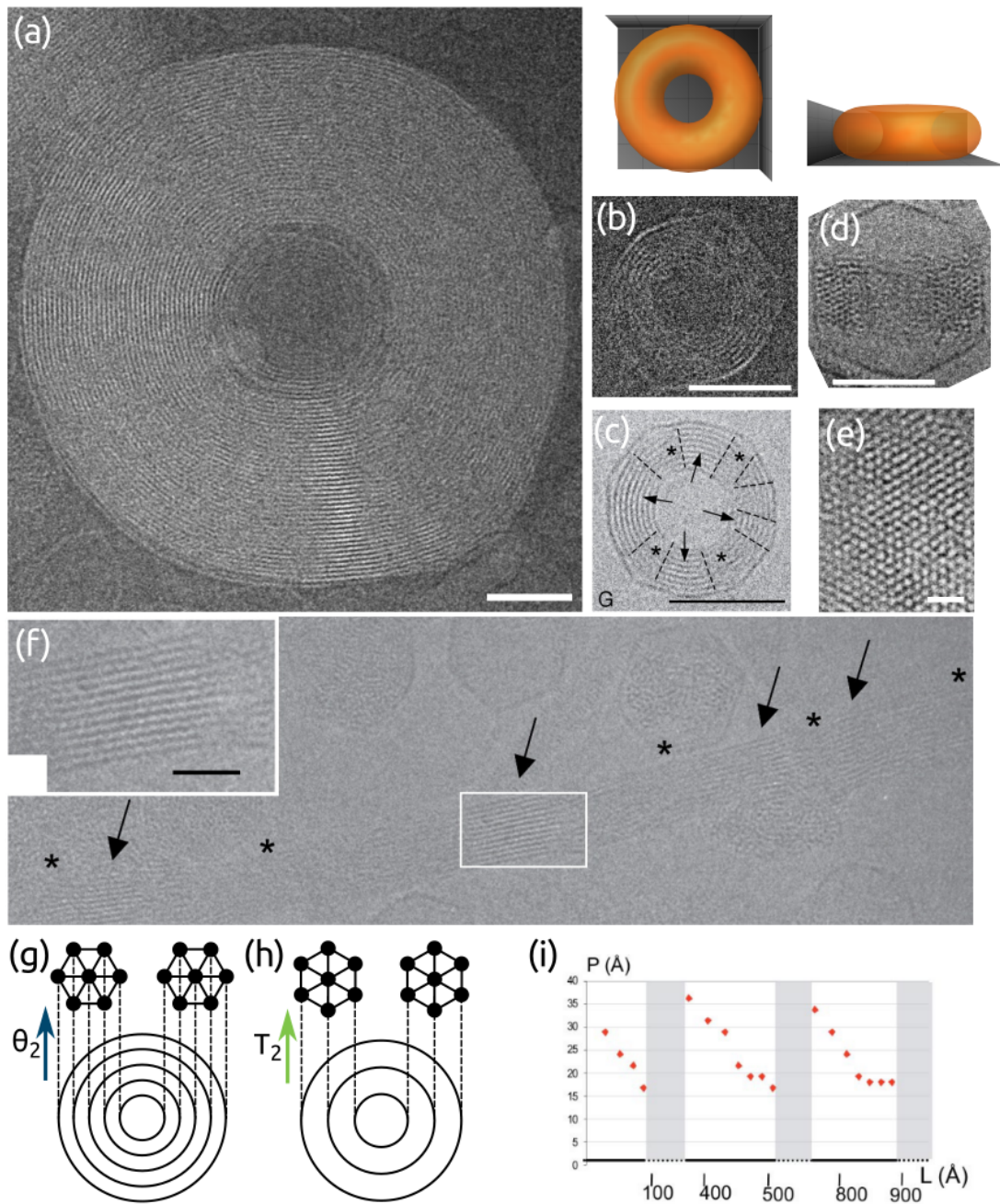


Figure 4.1: **General features of DNA toroids from cryoelectron microscopy.** (a) Top view of a giant toroid, with a viral capsid at its center. Scale bar, 50 nm. (b, c) Top views of small toroids. Scale bars, 50 nm. (c) Striated domains are indicated by arrows, blurred domains by asterisks and twist walls by dashed segments. (d) Side view of a small toroid. The two cross-sections are visible. Scale bar, 50 nm. (e) Zoom on a toroid cross-section. Each dot is a DNA helix pointing out of the page. Helices are hexagonally packed. Scale bar, 10 nm. (f) Straight toroidal bundle, made of the DNA ejected by several viral capsids, which are visible in the background. Striated domains are indicated by arrows, blurred domains by asterisks. Scale bar, 20 nm. (g) Expected striated domains when the direction of observation is  $\theta_2$ . (h) Expected striated domains when the direction of observation is  $T_2$ . (i) Helical pitch ( $P$ ) periodic variation along the length ( $L$ ) of a curved DNA helix, in a toroidal bundle. Figs. (c,f,i) adapted from *Leforestier and Livolant [2009]*, with permission from the authors.

$d \pm d_{\text{SEM}}$ (nm)		
	4 mM spermine	40 mM spermine
Small toroids	$2.61 \pm 0.01$	$2.62 \pm 0.01$
Giant toroids	$2.502 \pm 0.003$	$2.51 \pm 0.01$

Table 4.1: **Average striation spacing from FFTs.** Expected values are averages of averages from various datasets. Uncertainties are standard errors of means (SEMs).

observation, generating a blurry image. Therefore, most of the rotation was suggested to be concentrated at the interfaces between striated and blurry domains, at so-called *twist walls* [Fig. 4.1c, Leforestier and Livolant 2009]. Notice that striated and blurred domains are found also in straight DNA bundles, meaning that they twist in the same fashion [Fig. 4.1f].

In straight bundles, helices are aligned in such a way that major (minor) grooves on one helix face minor (major) grooves on the neighboring helix. In toroids, the preferred groove correlation depends on the toroid size, thus on curvature. In giant toroids, helices seem to be aligned as in straight bundles <sup>1</sup>. In small toroids, major (minor) grooves on one helix face major (minor) grooves on the neighboring helix. This kind of correlation is never observed in straight bundles, but it may be observed in the innermost regions of giant toroids. If the pitch were constant, it would be impossible to preserve groove correlations between helices belonging to neighboring striations, due to their different curvature. In toroidal bundles, groove correlations are possible because the helical pitch is not constant along the length of individual helices, where under-twisted regions alternate with over-twisted regions in a periodic fashion [Fig. 4.1i].

### 4.3 Curvature correlates with inter-helical spacing

The average inter-helical distance  $a_H$  is measured from FFTs of side views showing hexagonal order [Figs. 4.2b, 4.2c] as well as from top views showing striated patterns [Figs. 4.2d, 4.2e]. Notice that the striation spacing is  $d = \sqrt{3}/2 \times a_H$  [Fig. 4.2f]. The resulting average spacing is  $d_{\text{small}} \simeq 2.6$  nm in small toroids and  $d_{\text{giant}} \simeq 2.5$  nm in giant toroids, yielding  $a_H^{\text{small}} \simeq 3.0$  nm and  $a_H^{\text{giant}} \simeq 2.9$  nm, consistent with previous experiments [Raspud et al., 2005]. This behavior suggests a dependence of spacing on local curvature. Notice that spacing is hardly affected by spermine concentration. This is expected in the presence of relatively high amounts of monovalent cations (100 mM NaCl plus 10 mM Tris, notwithstanding 2 mM of divalent cations here) [Raspud et al., 2005].

Local spacing variations at different curvatures can be measured from the periodic variation of contrast intensity along line profiles perpendicular to striated domains [Figs. 4.2a, 4.2g]. Local spacing is inferred from peak to peak distances in the contrast profile. To reduce noise, in giant toroids, local distance is measured by averaging over three consecutive peaks (*i.e.*,  $d_i = D_i/3$ ,  $i = 1, 2, 3 \dots$  in Fig. 4.2g). This is not possible in small toroids, where distances are measured individually. In giant toroids, no measure is recorded within regions that have no free outer boundaries, *i.e.* wherever there is a contact zone between aggregated neighbors (gray circular sector in Fig. 4.2a).

<sup>1</sup>A. Leforestier, private communication

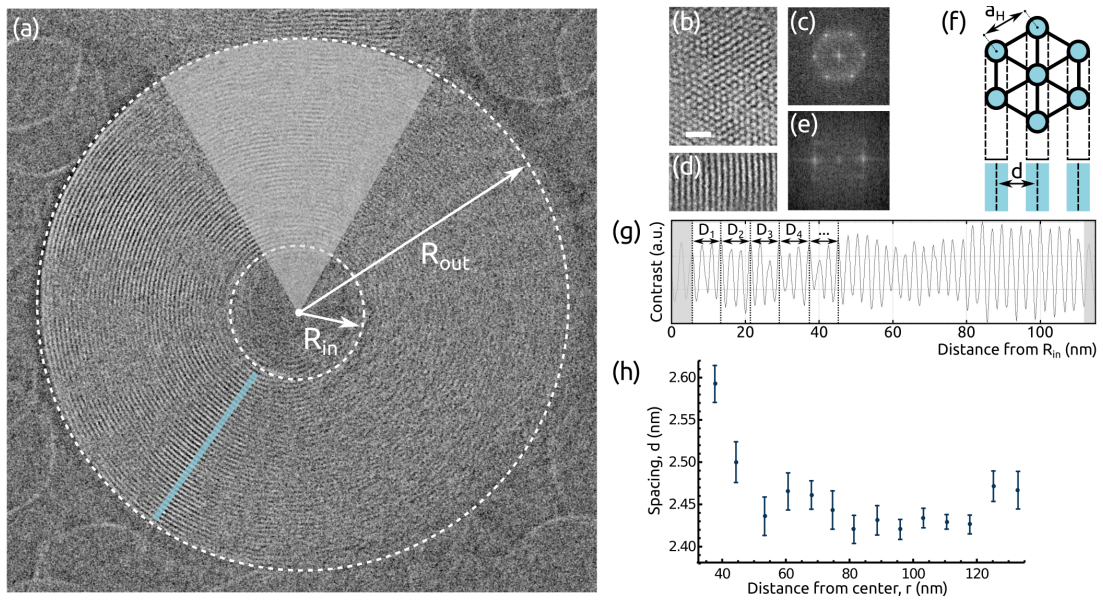


Figure 4.2: **Measurement of inter-helical spacing.** (a) Top view of a giant toroid. Inner and outer boundary evidenced by a white dashed line. Example of profile over which striation spacing is measured (cyan). No measurements taken in the direction of boundary regions where two toroids collide (gray circular sector). (b) Hexagonal packing from toroid side view. Scale bar 10 nm. (c) FFT of hexagonal packing from side view. (d) Striated pattern from toroid top view. (e) FFT of hexagonal packing from top view. (f) Projection of hexagonal lattice generating striations (cyan). (g) Contrast intensity over cyan profile in (a). Measurements not taken over first and last peak (green regions). Striated spacing averaged over three peaks ( $d_i = D_i/3$ ,  $i = 1, 2, 3 \dots$ ). (h) Striation spacing dependence on position resulting from (g).

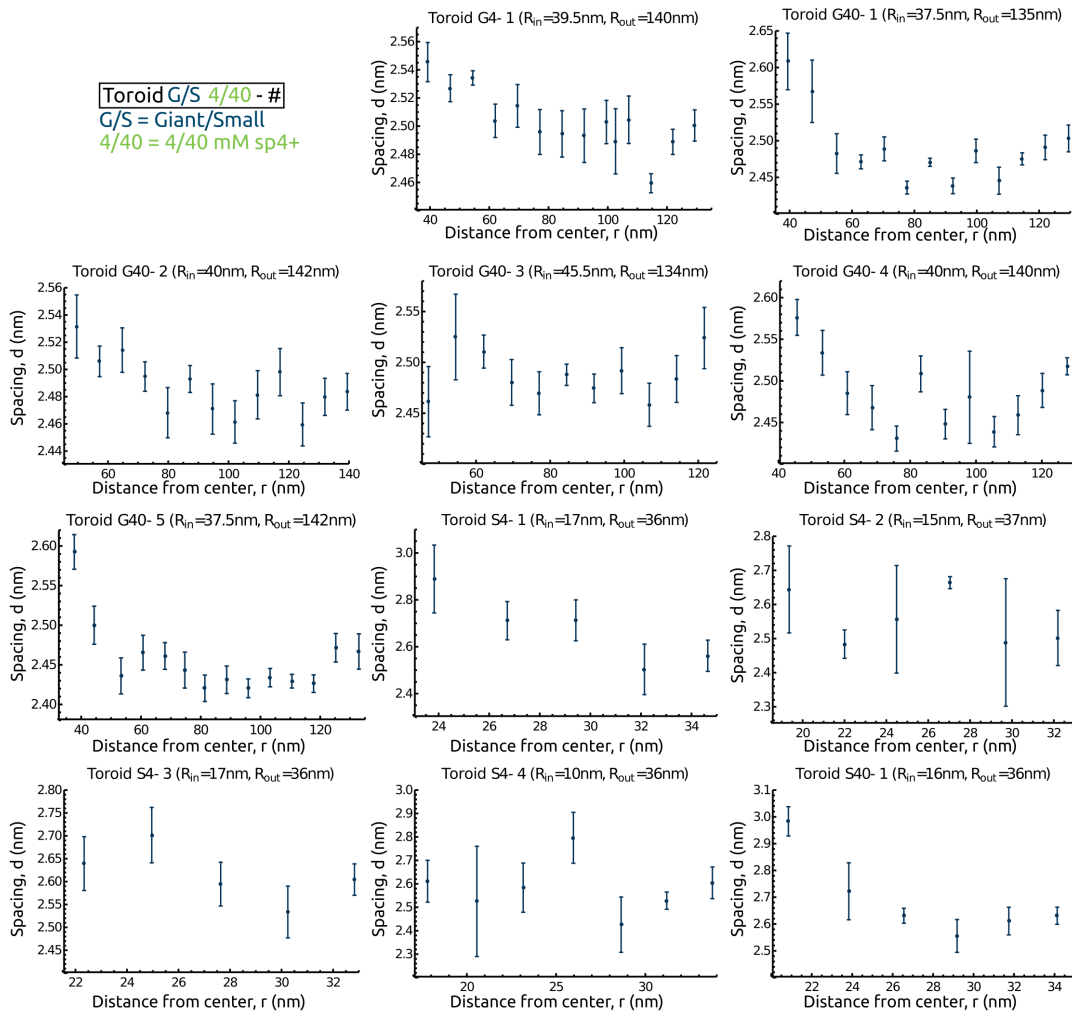


Figure 4.3: **Striation spacing datasets from various toroids.** Error bars are standard errors of means. Notice that the dataset corresponding to Toroid G40-5 is the one presented in Fig. 4.2.

Several line profiles are recorded for each toroid and averaged (from 8 to 13 in giant toroids, 3 to 6 in confined ones). The averaged  $d$  values are plotted as a function of the radius  $r$ , with  $r_i = r_{i-1} + d_{i-1}$  [Fig. 4.2h]. Series of measurements are obtained on six different giant toroids (six at 40 mM spermine, one at 4 mM) and five confined ones (four at 4 mM spermine, one at 40 mM) [Fig. 4.3]. Data from small toroids are far more noisy than from giant ones, on account of the impossibility of averaging measurements over three peak-to-peak distances and of the smaller number of line profiles per toroid there. These local measurements confirm and precise global ones obtained on FFTs. In each toroid, spacing decreases with the distance from the center of the assembly. Notice that this is a weak effect, relative spacing variations being limited to less than 10% going from the inner to the outer radius.

## 4.4 Summary

This chapter presents how DNA toroids of variable sizes can be generated *in vitro* and their main geometrical features. Small toroids can be generated by making single DNA molecules condense inside bacteriophage capsids. Giant toroids can be generated by making multiple DNA molecules, ejected from multiple bacteriophages, condense outside the capsids. The resulting giant toroids generally exhibit a capsid in their middle, which fixes their inner radius. From toroids side views, the hexagonal packing of DNA helices emerges.

From toroids top views, different patterns emerge depending on the hexagonal lattice orientation relative to the direction of observation. When the lattice is favorably oriented, striated patterns reflecting its periodicity are observed. Striated patterns persist as long as the lattice orientation deviates less than few degrees from the direction of observation. When the deviation is too strong, periodicity is lost and blurry patterns emerge. From striated patterns, it is possible to see how neighboring helices' grooves laterally correlate. In small toroids, the major grooves of each helix face the major grooves of its neighbors. In large toroids, the minor grooves of each helix face the major grooves of its neighbors.

The average inter-helical spacing in toroids can be accessed from FFTs of side views, which show that small toroids are, on average, less tightly packed than giant ones. Local variations in inter-helical spacing can be accessed from striated patterns. In every toroid, inter-helical spacing undergoes a  $\leq 10\%$  decrease going from the inner to the outer radius.

# Chapter 5

## Theoretical modeling

### Contents

---

5.1 Preliminary: how twist redistributes filaments' curvature in DNA toroids . . . . .	35
5.2 A minimal model of DNA toroid: bending stiffness vs. interactions	39
5.3 Perturbative solution of force-balance equations . . . . .	41
5.4 Fitting the experimental data . . . . .	45

---

The goal of this chapter is to understand why inter-helical spacing decreases with the distance from the inner radius of DNA toroids. We propose some simple theoretical arguments based on DNA elasticity and effective cation-mediated inter-helical forces. By pursuing this goal, we also infer some information on the effective inter-helical interaction potential.

Our intuition is that local spacing variations are related to DNA local elastic response. Specifically, DNA bending rigidity penalizes every region of the toroid proportionally to the DNA curvature it requires to be populated. Within striated regions, DNA helices appear to be locally arranged as if they were arcs of concentric circles, like a woolen thread in a spool. If this were true, then the curvature of DNA helices would decrease going from the inner radius  $R_{\text{in}}$  to the outer radius  $R_{\text{out}}$ . This geometry would support our intuition: DNA helices populate the inner regions the least because their curvature is the highest there. But does DNA curvature actually decrease going from  $R_{\text{in}}$  to  $R_{\text{out}}$ , as striated regions suggest? Since DNA toroids are twisted, it is possible that curvature is not that easily distributed throughout the assembly. If twist is strong enough, it may even be that DNA is less curved close to  $R_{\text{in}}$  than to  $R_{\text{out}}$ .

In Sec. 5.1, we quantify how filaments' curvature is distributed within a DNA toroid, depending on the DNA rate of twist around the toroid center line. We show that the experimental rate of twist is low enough that we can assume DNA helices behave as concentric circles around the toroid center, *i.e.* that DNA curvature increases with the distance from the inner radius. In Sec. 5.2, we leverage this result to develop a minimal two-dimensional model of DNA toroid, from which we investigate the mechanical equilibrium between DNA elasticity and effective inter-helical interactions. In Sec. 5.3, we solve our model and predict that inter-helical spacing decreases with the distance from the inner radius, in qualitative agreement with the experiments. In Sec. 5.4, we fit our model to the data and infer the local interaction potential between DNA helices.

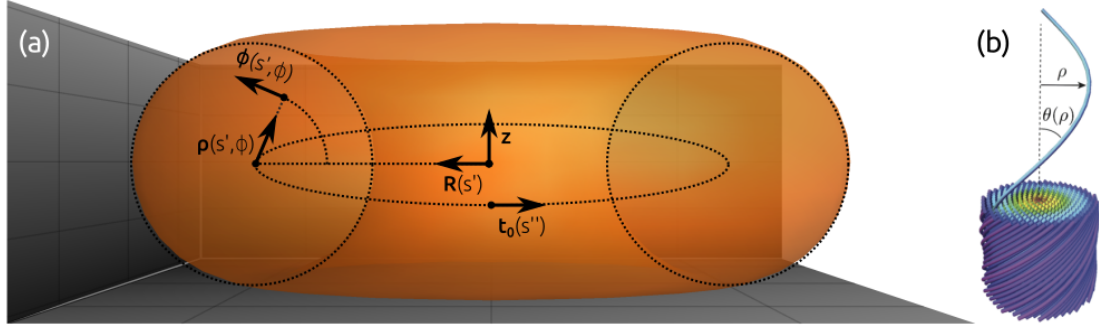


Figure 5.1: **Modeling a twisted DNA toroid.** (a) Covariant frame around the circular center line of radius  $R$ . (b) Double-twist geometry around a straight center line (vertical axis). Every filament is a helix with pitch  $2\pi/\Omega$ . Filaments are colored depending on their distance from the vertical axis. *Reproduced from Grason [2015], with permission from APS and the author.*

## 5.1 Preliminary: how twist redistributes filaments' curvature in DNA toroids

In this section, we address the following question: how is filaments' curvature distributed within a twisted DNA toroid? To answer, we parametrize the family of curves describing the DNA helical backbones in a toroidal bundle and use this parametrization to calculate the local filaments' curvature.

In Sec. 4.2, we have shown that the rate of twist in DNA toroids is not constant. Most of the twist is concentrated at the boundaries between striated and blurry domains [Fig. 4.1c]. Accounting for such a non-constant rate of twist goes beyond the purpose of this section. Our current interest is limited to the effects of twist in striated domains, where spacing measurements are taken, and where we assume the rate of twist to be small and constant. Therefore, we parametrize a twisted toroidal bundle with constant rate of twist around its center line.

We construct our twisted bundle as a continuous family of curves around a circular center line of radius  $R$ . We parametrize the center line by its arc length  $s \in [0, 2\pi R]$ , such that its position vector and unit tangent are  $\mathbf{R}(s) = R\hat{\mathbf{R}}$  and  $\hat{\mathbf{t}}_0 = \partial_s \mathbf{R}$ , respectively [Fig. 5.1a]. Notice that  $\partial_s \hat{\mathbf{t}}_0 = -\hat{\mathbf{R}}/R$ .

We introduce a system of orthogonal coordinates  $\{\hat{\mathbf{t}}_0, \hat{\boldsymbol{\rho}}, \hat{\boldsymbol{\phi}}\}$  that co-moves with the center line [Fig. 5.1a], in which:

$$\hat{\boldsymbol{\rho}}(s, \phi) = -\cos \phi \hat{\mathbf{R}}(s) + \sin \phi \hat{\mathbf{z}}, \quad (5.1a)$$

$$\hat{\boldsymbol{\phi}}(s, \phi) = \partial_\phi \hat{\boldsymbol{\rho}}(s, \phi). \quad (5.1b)$$

In these coordinates, the position vector of any point in space can be expressed in terms of its distance  $\rho$  from the center line as  $\mathbf{x}(s, \rho, \phi) = \mathbf{R}(s) + \rho \hat{\boldsymbol{\rho}}(s, \phi)$ .

Since we are constructing a continuous family of curves, a filament passes through any point  $(s, \rho, \phi)$  in the toroid. Ultimately, we want to know what the local filaments' curvature  $c(\rho, \phi)$  is, depending on the bundle's rate of twist. To calculate the curvature of a filament, we need to know how its unit tangent vector varies along its own direction. Therefore, we introduce the field of local unit tangents  $\hat{\mathbf{t}}(s, \rho, \phi)$ , and relate it to the local filaments' curvature as:

$$c\hat{\mathbf{n}} = (\hat{\mathbf{t}} \cdot \nabla) \hat{\mathbf{t}}, \quad (5.2)$$

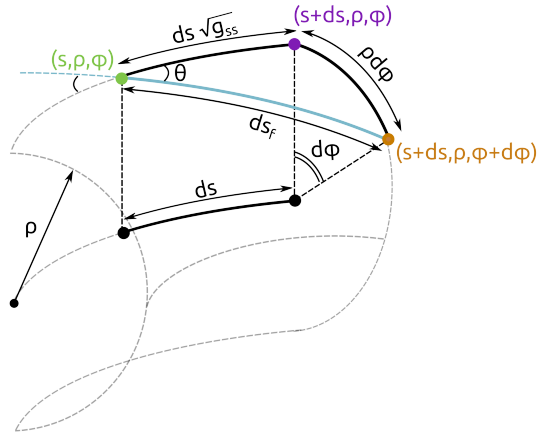


Figure 5.2: **Circulation of a filament around the toroid center line.** A portion of toroidal surface, with circular section of radius  $\rho$ , on which a quasi-helical filament (cyan) lies. The filament makes a tilt angle  $\theta(\rho, \phi)$  with the tangent of the toroid center line. The toroidal coordinates of three different points are denoted by three different colors (green, purple and brown). Notice that  $g_{ss} = \partial_s \mathbf{x} \cdot \partial_s \mathbf{x} = 1 - \rho \cos \phi / R$  is equal to 1 only at  $\phi = \pm\pi/2$ .

where  $\hat{\mathbf{n}}$  is the filaments' local unit normal and  $\hat{\mathbf{t}} \cdot \nabla$  is a derivative along the filaments' direction.

At this point, we need to specify what  $\hat{\mathbf{t}}(s, \rho, \phi)$  is. In a real DNA bundle, the relative orientation of neighboring DNA molecules emerges from mechanical equilibrium. Because of their chiral architecture, two neighboring helices exert torques on each other [Cherstvy, 2008]. Deriving a field of tangents  $\hat{\mathbf{t}}(s, \rho, \phi)$  from the optimization of a realistic torque field goes beyond our current purposes. Rather, we propose an educated *ansatz* from empirical considerations.

To start, we prescribe a form of  $\hat{\mathbf{t}}(s, \rho, \phi)$  that reproduces the macromolecular twist observed in the experiments. If we think of a DNA bundle as a set of screw-like objects packed around a central one, a classical result of the theory of cholesteric liquid crystals is that chiral interactions promote a so-called *double-twist* geometry [Wright and Mermin, 1989; Grason, 2015]. We show an example of double-twist arrangement around a straight central filament in Fig. 5.1b. There, every filament is a helix with pitch  $2\pi/\Omega$  and tilt angle  $\theta = \arctan(\Omega\rho)$  relative to the vertical axis. We introduce double-twist in our toroidal bundle by writing

$$\mathbf{t}(s, \rho, \phi) = \cos[\theta(\rho, \phi)] \hat{\mathbf{t}}_0(s) + \sin[\theta(\rho, \phi)] \hat{\boldsymbol{\phi}}(s, \phi). \quad (5.3)$$

Notice that, here, contrary to the straight double-twist, the tilt angle  $\theta(\rho, \phi)$  relative to the center line also depends on the angular coordinate  $\phi$ . In fact, a filament describing a helical path on a toroidal surface around the centerline cannot twist at the same rate throughout its length. For this reason, we refer to the filament geometry in this case as *quasi-helical*. We define the local circulation rate  $\omega(\rho, \phi)$  around the toroid center line of a quasi-helix with radius  $\rho$  as the variation of its angular coordinate  $\phi$  relative to the arc length  $s$  of the center line, *i.e.*  $\omega = \partial\phi/\partial s$  [Atkinson et al., 2019]. We can relate  $\omega = \partial\phi/\partial s$  to the tilt angle  $\theta(\rho, \phi)$  with simple geometrical considerations and with the aid of a schematic [Fig. 5.2]. In the figure, we have reproduced a portion of toroidal surface with radius  $\rho$ , on which a quasi-helical filament (cyan) lies. We call  $ds_f$  the length of the filament arc connecting the points with coordinates  $(s, \rho, \phi)$

and  $(s + ds, \rho, \phi + d\phi)$ . Notice that the distance between the points with coordinates  $(s, \rho, \phi)$  and  $(s + ds, \rho, \phi)$  is  $\sqrt{g_{ss}} ds$ , with  $g_{ss} = \partial_s \mathbf{x} \cdot \partial_s \mathbf{x} = 1 - \rho \cos \phi / R$ . Then, the two relations

$$ds_f \sin \theta = \rho d\phi, \quad (5.4a)$$

$$ds_f \cos \theta = \sqrt{g_{ss}} ds, \quad (5.4b)$$

imply

$$\omega(\rho, \phi) = \frac{\partial \phi}{\partial s} = \frac{\sqrt{g_{ss}}}{\rho} \tan \theta. \quad (5.5)$$

Later in this section, we use Eq. (5.5) to set experimental bounds on  $\theta(\rho, \phi)$ .

So far, we have built up a toroidal bundle that twists [Eq. (5.3)], effectively accounting for the chiral interactions between DNA helices by resorting to the double-twist geometry. We now adapt  $\theta(\rho, \phi)$  so as to account for the tendency of neighboring helices to stay at a fixed distance from each other, which is set by inter-helical forces. We know from the experiments that inter-helical spacing varies very little throughout a toroid, less than 10% [Sec. 4.2]. This suggests that a DNA bundle is an incompressible material, a condition that we enforce by ruling out splay deformations in the tangent field, which is the same as saying

$$\nabla \cdot \hat{\mathbf{t}} = 0. \quad (5.6)$$

To calculate the divergence above, we have to express the gradient  $\nabla$  and the tangent  $\hat{\mathbf{t}}$  in a common vector basis. From differential geometry [Kreyszig, 1991], we know that the usual partial derivatives are the so-called *covariant components* of the gradient, implying

$$\nabla = \mathbf{g}^s \partial_s + \mathbf{g}^\rho \partial_\rho + \mathbf{g}^\phi \partial_\phi. \quad (5.7)$$

Here,  $\{\mathbf{g}^s, \mathbf{g}^\rho, \mathbf{g}^\phi\}$  is the so-called *contravariant basis*, which is the dual of the *covariant basis*  $\{\mathbf{g}_s, \mathbf{g}_\rho, \mathbf{g}_\phi\}$ , defined as:

$$\mathbf{g}_s = \partial_s \mathbf{x} = \left(1 - \frac{\rho}{R} \cos \phi\right) \hat{\mathbf{t}}_0; \quad (5.8a)$$

$$\mathbf{g}_\rho = \partial_\rho \mathbf{x} = \hat{\boldsymbol{\rho}}; \quad (5.8b)$$

$$\mathbf{g}_\phi = \partial_\phi \mathbf{x} = \rho \hat{\boldsymbol{\phi}}. \quad (5.8c)$$

The duality condition  $\mathbf{g}_i \cdot \mathbf{g}^j = \delta_i^j$ , where  $\delta_i^j$  is the Kronecker delta and  $i, j = s, \rho, \phi$ , implies:

$$\mathbf{g}^s = \left(1 - \frac{\rho}{R} \cos \phi\right)^{-1} \hat{\mathbf{t}}_0; \quad (5.9a)$$

$$\mathbf{g}^\rho = \hat{\boldsymbol{\rho}}; \quad (5.9b)$$

$$\mathbf{g}^\phi = \frac{1}{\rho} \hat{\boldsymbol{\phi}}. \quad (5.9c)$$

We can use the contravariant basis to find the covariant components of the tangent field [Eq. (5.3)], giving:

$$t^s = \hat{\mathbf{t}} \cdot \mathbf{g}^s = \left(1 - \frac{\rho}{R} \cos \phi\right)^{-1} \cos \theta; \quad (5.10a)$$

$$t^\rho = \hat{\mathbf{t}} \cdot \mathbf{g}^\rho = 0; \quad (5.10b)$$

$$t^\phi = \hat{\mathbf{t}} \cdot \mathbf{g}^\phi = \frac{\sin \theta}{\rho}. \quad (5.10c)$$

We can now explicit the splay-free (or vanishing divergence) condition Eq. (5.6) by putting together Eqs. (5.10) and (5.7), such that

$$\nabla \cdot \hat{t} = (\mathbf{g}^s \partial_s + \mathbf{g}^\rho \partial_\rho + \mathbf{g}^\phi \partial_\phi) \cdot (t^s \mathbf{g}_s + t^\rho \mathbf{g}_\rho + t^\phi \mathbf{g}_\phi) \quad (5.11a)$$

$$= \mathbf{g}^s \cdot t^\phi \partial_s \mathbf{g}_\phi + \partial_\phi t^\phi \quad (5.11b)$$

$$= \frac{\sin \theta \sin \phi}{1 - \rho \cos \phi / R} + \frac{\cos \theta}{\rho} \partial_\phi \theta. \quad (5.11c)$$

Notice that all the terms in Eq. (5.11a) that do not appear in Eq. (5.11b) are equal to zero. One can verify that the right hand side of Eq. (5.11c) is zero for any  $\theta(\rho, \phi)$  of the form [Kulić et al., 2004; Koning et al., 2014; Atkinson et al., 2019]

$$\theta(\rho, \phi) = \arcsin \left( \frac{f(\rho)}{1 - \rho \cos \phi / R} \right), \quad (5.12)$$

in which  $f(\rho)$  is an arbitrary function of  $\rho$ . Henceforth, we make the simplest linear choice  $f(\rho) = \Omega \rho$ , coherent with previous studies on liquid crystalline toroidal packings [Kulić et al., 2004; Koning et al., 2014]. The coefficient  $\Omega$  can be interpreted as the bundle twist strength. It is related to the filaments' circulation rate around the toroid center line  $\omega(\rho, \phi)$  [Eq. (5.5)],

$$\omega(\rho, \phi) = \frac{\sqrt{\mathbf{g}^s \cdot \mathbf{g}^s}}{\rho} \tan \theta = \Omega \left[ 1 + \left( \frac{\Omega \rho}{1 - \rho \cos \phi / R} \right)^2 \right]^{-1/2}. \quad (5.13)$$

Notice that, when  $\Omega = 0$ , we have a bundle of circular filaments that do not twist.

We now estimate  $\Omega$  thanks to the data collected in striated domains [Sec. 4.2]. We consider here only small toroids confined in viral capsids, essentially because their cross-sections are far more circular than those of giant toroids, allowing a clearer definition of the tubular radius  $\rho$ . First, we estimate the experimental circulation  $\omega_{\text{exp}}$  in a striated domain. The typical arc length of a striated domain is  $\Delta s_{\text{exp}} \simeq 10$  nm. Over a striated domain, the typical rotation of the DNA hexagonal lattice around the toroid center line is limited to few degrees, certainly much less than the  $\pi/6$  rotation associated with twist walls [Sec. 4.2]. We thus assume an average rotation of  $\Delta \phi_{\text{exp}} = \pi/60$ , yielding  $\omega_{\text{exp}} = \Delta \phi_{\text{exp}} / \Delta s_{\text{exp}}$ . Now, since our data are taken from DNA toroid top views, our observations are made at  $\phi_{\text{exp}} \simeq \pi/2$  and on the outer layer of DNA helices, *i.e.* at  $\rho_{\text{exp}}^{\text{out}} = R_{\text{exp}}/3$  [Leforestier and Livolant, 2009], with  $R_{\text{exp}} \simeq 25$  nm. From Eq. (5.13), we get

$$\omega(\rho_{\text{exp}}^{\text{out}}, \phi_{\text{exp}}) = \Omega_{\text{exp}} [1 + (\Omega_{\text{exp}} \rho_{\text{exp}}^{\text{out}})^2]^{-1/2} = \frac{\Delta \phi_{\text{exp}}}{\Delta s_{\text{exp}}}, \quad (5.14)$$

whose numerical solution yields  $\Omega_{\text{exp}} \simeq 0.13/R_{\text{exp}}$ .

We are all set to calculate the filaments' curvature field  $c(\rho, \phi)$  from Eq. (5.2). To express the directional derivative operator  $\hat{t} \cdot \nabla$ , we use the contravariant components of the tangent field [Eqs. (5.10)], such that

$$\mathbf{t} \cdot \nabla = t^i \mathbf{g}_i \cdot \mathbf{g}^j \partial_j = \cos \theta \left( 1 - \frac{\rho}{R} \cos \phi \right)^{-1} \partial_s + \frac{\sin \theta}{\rho} \partial_\phi, \quad (5.15)$$

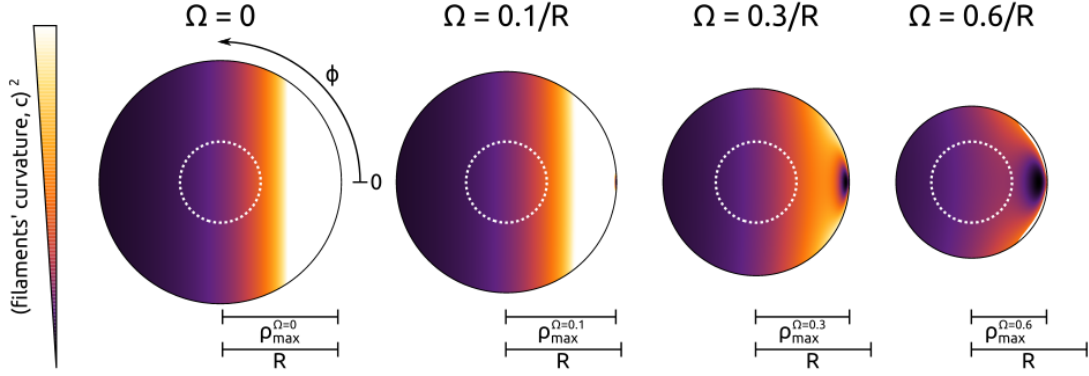


Figure 5.3: **Influence of twist on filaments' local curvature.** Heat maps of the squared local curvature ( $c^2$ ) of filaments over the cross section of a twisted toroidal bundle, at different values of the twist strength  $\Omega$ . The toroid has radius  $R = 1$  and tubular radius  $\rho_{\max} = 1/(1 + \Omega)$  (see text). The boundary of the cross-section corresponding to the typical confined DNA toroid is drawn as a white dashed circle. Notice that  $\phi = 0$  close to the center of the assembly [Fig. 5.1a].

where summation over repeated indices is implied. Applying the operator above to the unit tangent field [Eq. (5.3)], Eq. (5.2) gives  $[c(\rho, \phi)]^2 = C_1^2 + C_2^2 + C_3^2$ , in which:

$$C_1 = \frac{\cos^2 \theta \cos \phi}{R - \rho \cos \phi} - \frac{\sin^2 \theta}{\rho}; \quad (5.16a)$$

$$C_2 = \frac{\partial_\phi \theta \sin \theta \cos \theta}{\rho} - \frac{\cos^2 \theta \sin \phi}{R - \rho \cos \phi}; \quad (5.16b)$$

$$C_3 = \frac{\cos \theta \sin \theta \sin \phi}{R - \rho \cos \phi} - \frac{\partial_\phi \theta \sin^2 \phi}{\rho}. \quad (5.16c)$$

In Fig. 5.3, we plot  $[c(\rho, \phi)]^2$  over a toroidal cross-section for some values of  $\Omega$ . Notice that the section radius has an upper bound  $\rho_{\max} = 1/(\Omega + 1/R)$ , which comes from the domain of the arcsin in the definition of  $\theta(\rho, \phi)$  [Eq. (5.12)]. The typical section of confined DNA toroids is shown as a white dashed contour in Fig. 5.3. When  $\Omega = 0$ , filaments are circles and curvature is the highest where  $\phi = 0$ , at the boundary, *i.e.* close to the center of the toroid [Fig. 5.2]. As  $\Omega$  increases, a zero curvature region emerges from the center of the toroid. This curvature drop corresponds to a local change in curvature sign. In fact, filaments go from winding around the z-axis (positive curvature), when  $\Omega = 0$ , to winding around the toroid center line (negative curvature), when  $\Omega > 0$ . In other words, the filaments' local normal goes from pointing towards the center of the toroid to gradually pointing away from it.

We have quantified how twist redistributes curvature in a DNA toroid section. Given the aspect ratio of confined DNA toroids, we see from Fig. 5.2 that the filaments' curvature behaves qualitatively as in the  $\Omega = 0$  case even at  $\Omega \geq \Omega_{\text{exp}} \simeq 0.13$ .

## 5.2 A minimal model of DNA toroid: bending stiffness vs. interactions

In this section, we develop a minimal mechanical model of DNA toroid. This model qualitatively predicts the experimental dependence of inter-helical spacing on posi-

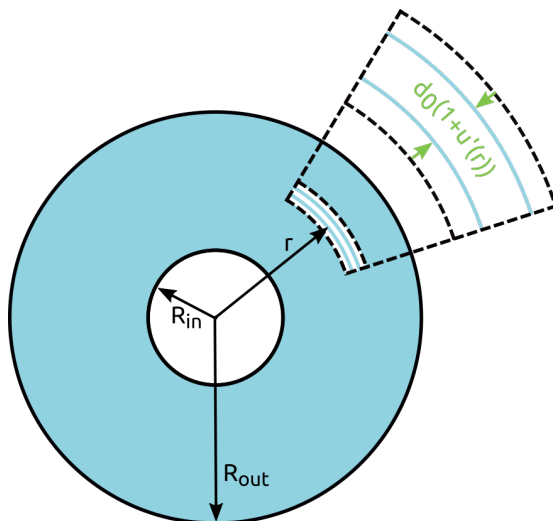


Figure 5.4: **Two-dimensional model of DNA toroid.** Continuum description for a dense set of concentric DNA circles (cyan). Two circles, that in the reference state are located at  $r$  and  $r + dr$ , are spaced  $d_0[1 + u'(r)]$  in the final state.

tion, relying on just two physical ingredients: effective interactions between neighboring helices and DNA bending rigidity.

Motivated by the result of Sec. 5.1, we neglect all strictly three dimensional features of DNA toroids. In particular, we neglect twist, which we have proven to be weak enough to allow the approximation of a toroidal DNA bundle with a set of concentric circular filaments [Sec. 5.1]. The smallest and biggest circles in the set have a radii  $R_{in}$  and  $R_{out}$ , respectively, and coincide with the inner and outer radius of a DNA toroid. Moreover, since the typical inter-helical spacing,  $\simeq 3$  nm, is much smaller than the extension  $R_{out} - R_{in}$  of the assembly ( $\simeq 20$  nm in small and  $\simeq 100$  nm in giant toroids), we take the continuum limit and model the set of circles as a CD-ROM [Fig. 5.4], parametrized by the radial coordinate  $r \in [R_{in}; R_{out}]$ .

We model DNA as a semi-flexible polymer with bending rigidity  $k_b = \ell_p k_B T$ , where  $\ell_p$  is DNA persistence length,  $k_B$  is Boltzmann's constant and  $T$  is temperature. If DNA were a flexible polymer (*i.e.*,  $k_b = 0$ ), inter-helical spacing would be the same throughout the assembly, its value being fixed to some constant,  $d_0$ , corresponding to a minimum of the interaction potential between neighboring helices. Our CD-ROM would be the continuum limit of a dense set of equally spaced circles, such that the number of circles between  $r$  and  $r + dr$  would be  $dr/d_0$ . Henceforth, we refer to  $k_b = 0$  as the *reference state*. When  $k_b > 0$ , DNA filaments resist bending by relaxing local curvature, such that the local radius of curvature goes from  $r$  to  $r + u(r)$ . The radial displacement field,  $u(r)$ , defines what we call the *final state*. In the final state, inter-helical spacing can be written as  $d(r) = d_0[1 + u'(r)]$ , where the prime denotes differentiation with respect to  $r$  [Fig. 5.4].

According to the data, spacing never decreases more than 10% going from  $R_{in}$  to  $R_{out}$  [Sec. 4.3], meaning that  $u'(r) \ll 1$ , or, equivalently, that bending effects are “weak” compared to interactions. We formalize this observation by introducing a dimensionless small parameter,  $\epsilon$ , defined as the ratio between the typical energy scales associated to bending and interactions, and such that  $u(r) \propto \epsilon$ . A convenient estimate of the bending energy scale is  $k_b R_c$ , where we have used the “radius” of a viral capsid  $R_c \simeq 40$  nm as a proxy to the typical radius of curvature of DNA he-

lices. We estimate the typical interaction energy scale by observing that, since spacing is close to  $d_0$  throughout the assembly, we can approximate the interaction potential by Taylor expanding it around  $d_0$ . To second order, this yields  $\gamma/2 \times [d(r) - d_0]^2 = \gamma/2 \times d_0^2 [u'(r)]^2$ , where we denoted by  $\gamma$  the stiffness of the parabolic potential. Then, interactions have a typical energy scale  $\gamma d_0^2 R_c$ , where we used  $R_c$  as a proxy to the typical length of our system. Finally, we define the small parameter as  $\epsilon = k_b / \gamma d_0^2 R_c^2 \ll 1$ .

We are all set to determine what displacement field  $u(r)$  enforces mechanical equilibrium in the final state. Since toroids are fairly monodispersed in the experiments, we work in the ensemble of fixed DNA length  $\mathcal{L}$ , implying the conservation law

$$\mathcal{L} = \int_{R_{\text{in}}}^{R_{\text{out}}} \frac{dr}{d_0} 2\pi [r + u(r)]. \quad (5.17)$$

Notice that the integral is performed in the reference state. Finally, we postulate the free energy of deformation

$$\mathcal{F} [u(r), R_{\text{in}}, R_{\text{out}}] = \int_{R_{\text{in}}}^{R_{\text{out}}} \frac{dr}{d_0} 2\pi [r + u(r)] \left\{ \frac{k_b}{2} \frac{1}{[r + u(r)]^2} + \frac{\gamma d_0^2}{2} [u'(r)]^2 - \mu \right\}, \quad (5.18)$$

where the the first term is bending energy, the second is the interaction energy and the third,  $\mu$ , is a Lagrange multiplier that enforces Eq. (5.17). Dimensionally,  $\mu$  is a force and acts as a chemical potential difference between our toroid and a virtual DNA reservoir. Notice that also the latter integral is performed in the reference state.

### 5.3 Perturbative solution of force-balance equations

In this section, we minimize the free energy functional Eq. (5.18) in the specific case of giant toroids, whose internal radius is fixed by the radius of a viral capsid,  $R_{\text{in}} = R_c \simeq 40$  nm. Because the minimization procedure is almost identical for small toroids, with the only difference that the fixed boundary would be the outer radius in that case, we give the results for small toroids at the end of this section without going through the derivation a second time.

Our plan is to solve force balance equations

$$\left. \frac{\delta \mathcal{F} [u(r), R_{\text{out}}]}{\delta u(r)} \right|_{R_{\text{out}}, \mu} = 0, \quad (5.19a)$$

$$\left. \frac{\partial \mathcal{F} [u(r), R_{\text{out}}]}{\partial R_{\text{out}}} \right|_{u(r), \mu} = 0, \quad (5.19b)$$

to leading order in the small parameter  $\epsilon$ , obtaining expressions of  $u(r)$  and  $R_{\text{out}}$  in terms of the Lagrange multiplier  $\mu$ . Then, we plug these expressions into Eq. (5.17) so as to find the dependency of  $\mu$  on the input parameters  $R_c$  and  $\mathcal{L}$ .

To set up the perturbative expansion in powers of  $\epsilon$ , we first need to make all of our quantities adimensional. We make the choice of units  $R_c = \gamma d_0^2 = 1$ , and define the rescaled quantities

$$\tilde{\mathcal{F}} = \frac{\mathcal{F}}{\gamma d_0^2 R_c}, \quad \tilde{R}_{\text{out}} = \frac{R_{\text{out}}}{R_c}, \quad \tilde{r} = \frac{r}{R_c}, \quad \tilde{d}_0 = \frac{d_0}{R_c}, \quad \tilde{u} = \frac{u}{R_c} \quad \text{and} \quad \tilde{\mu} = \frac{\mu}{\gamma d_0^2}. \quad (5.20)$$

Notice that, in these units, the bending stiffness  $k_b$  is the small parameter  $\epsilon$ . For completeness, we give the expression of the non-dimensional free energy functional [Eq. (5.18)]:

$$\tilde{\mathcal{F}}[\tilde{u}(\tilde{r}), \tilde{R}_{\text{out}}] = \int_1^{\tilde{R}_{\text{out}}} \frac{d\tilde{r}}{\tilde{d}_0} 2\pi [\tilde{r} + \tilde{u}(\tilde{r})] \left\{ \frac{\epsilon}{2} \frac{1}{[\tilde{r} + \tilde{u}(\tilde{r})]^2} + \frac{1}{2} [\tilde{u}'(\tilde{r})]^2 - \tilde{\mu} \right\}. \quad (5.21)$$

We now turn to the solution of Eq. (5.19a). We say that  $\mathcal{O}(\tilde{\mu}) = \mathcal{O}(\epsilon)$ , since in the absence of deformation (*i.e.*,  $\epsilon = 0$ ) the total DNA length is automatically conserved. We expand the free energy [Eq. (5.21)] in powers of  $\epsilon$ , such that  $\tilde{\mathcal{F}} = \tilde{\mathcal{F}}_1\epsilon + \tilde{\mathcal{F}}_2\epsilon^2 + \mathcal{O}(\epsilon^3)$ , with:

$$\tilde{\mathcal{F}}_1(\tilde{R}_{\text{out}}) = \int_1^{\tilde{R}_{\text{out}}} d\tilde{r} 2\pi \left( \frac{1}{2\tilde{r}} - \tilde{\mu}\tilde{r} \right); \quad (5.22a)$$

$$\tilde{\mathcal{F}}_2[\tilde{u}(\tilde{r}), \tilde{R}_{\text{out}}] = \int_1^{\tilde{R}_{\text{out}}} d\tilde{r} 2\pi \left\{ -\frac{\tilde{u}(\tilde{r})}{2\tilde{r}^2} + \frac{\tilde{r}}{2} [\tilde{u}'(\tilde{r})]^2 - \tilde{\mu}\tilde{u}(\tilde{r}) \right\}. \quad (5.22b)$$

Since  $\tilde{\mathcal{F}}_1$  does not depend on  $\tilde{u}(\tilde{r})$ , the leading order to take into account in Eq. (5.19a) is  $\tilde{\mathcal{F}}_2$ . To calculate the variational derivative  $\delta\tilde{\mathcal{F}}_2/\delta\tilde{u}(\tilde{r})$ , we introduce a small perturbation  $\delta\tilde{u}(\tilde{r})$  in the functional  $\tilde{\mathcal{F}}_2$ , getting

$$\tilde{\mathcal{F}}_2[\tilde{u}(\tilde{r}) + \delta\tilde{u}(\tilde{r}), \tilde{R}_{\text{out}}] = \tilde{\mathcal{F}}_2[\tilde{u}(\tilde{r}), \tilde{R}_{\text{out}}] + \delta\tilde{\mathcal{F}}_2[\tilde{u}(\tilde{r}), \delta\tilde{u}(\tilde{r}), \tilde{R}_{\text{out}}] + \mathcal{O}[\delta\tilde{u}(\tilde{r})^2], \quad (5.23)$$

where  $\delta\tilde{\mathcal{F}}_2$ , also known as the *first variation*, reads

$$\delta\tilde{\mathcal{F}}_2[\tilde{u}(\tilde{r}), \delta\tilde{u}(\tilde{r}), \tilde{R}_{\text{out}}] = \int_1^{\tilde{R}_{\text{out}}} d\tilde{r}' 2\pi \left[ -\frac{\delta\tilde{u}(\tilde{r}')}{2\tilde{r}'^2} + \tilde{r}'\tilde{u}'(\tilde{r}')\delta\tilde{u}'(\tilde{r}') - \tilde{\mu}\delta\tilde{u}(\tilde{r}') \right]. \quad (5.24)$$

Integrating by parts the second term in Eq. (5.24), the first variation becomes

$$\delta\tilde{\mathcal{F}}_2[\tilde{u}(\tilde{r}), \delta\tilde{u}(\tilde{r}), \tilde{R}_{\text{out}}] = [\tilde{r}'\tilde{u}'(\tilde{r}')\delta\tilde{u}(\tilde{r}')]_1^{\tilde{R}_{\text{out}}} + \int_1^{\tilde{R}_{\text{out}}} d\tilde{r}' 2\pi \left\{ -\frac{1}{2\tilde{r}'^2} - [\tilde{r}'\tilde{u}'(\tilde{r}')] - \tilde{\mu} \right\} \delta\tilde{u}(\tilde{r}'), \quad (5.25)$$

meaning that the stationarity condition is a differential equation,

$$-\frac{1}{2\tilde{r}^2} - \tilde{\mu} - \tilde{u}'(\tilde{r}) - \tilde{r}\tilde{u}''(\tilde{r}) = 0, \quad (5.26)$$

to be solved under two boundary conditions:

$$\tilde{u}(1) = 0, \quad (5.27a)$$

$$\tilde{u}'(\tilde{R}_{\text{out}}) = 0. \quad (5.27b)$$

The fixed boundary condition [Eq. (5.27a)] indicates that the innermost DNA filament sticks to the viral capsid. Notice that Eq. (5.27a) is equivalent to  $\delta\tilde{u}(1) = 0$ , in the sense that the choice of the perturbation  $\delta\tilde{u}(\tilde{r})$  is restricted to those functions that satisfy Eq. (5.27a). The free boundary condition [Eq. (5.27b)] indicates that the toroid is unconfined, implying zero stress (thus, strain) at the boundary. Finally, the solution of Eq. (5.26) is

$$\tilde{u}(\tilde{r}) = \frac{(\tilde{r}-1)(1-2\tilde{r}\tilde{\mu})}{2\tilde{r}} - \left( \frac{1}{2\tilde{R}_{\text{out}}} - \tilde{\mu}\tilde{R}_{\text{out}} \right) \log(\tilde{r}). \quad (5.28)$$

Turning to Eq. (5.19b), we call  $f(r, u(r), u'(r))$  the integrand of the free energy functional [Eq.(5.21)] and rewrite the left hand side of Eq. (5.19b) as

$$\frac{\partial}{\partial \tilde{R}_{\text{out}}} \int_1^{\tilde{R}_{\text{out}}} d\tilde{r} \tilde{f}(\tilde{r}, \tilde{u}(\tilde{r}), \tilde{u}'(\tilde{r})) = \tilde{f}(\tilde{R}_{\text{out}}, \tilde{u}(\tilde{R}_{\text{out}}), \tilde{u}'(\tilde{R}_{\text{out}})) \quad (5.29)$$

Combining the equation above with Eq. (5.19b), and observing that  $\tilde{u}'(\tilde{R}_{\text{out}}) = 0$  [Eq. (5.27b)], this second force balance equation is

$$\tilde{f}(\tilde{R}_{\text{out}}, \tilde{u}(\tilde{R}_{\text{out}})) = 0. \quad (5.30)$$

Once again, we solve this equation perturbatively, this time expanding the outer radius in powers of  $\epsilon$ :  $\tilde{R}_{\text{out}} = \tilde{R}_{\text{out}}^0 + \mathcal{O}(\epsilon)$ . To leading (*i.e.*, first) order in  $\epsilon$ , Eq. (5.30) reads  $1/(2\tilde{R}_{\text{out}}^0) - \tilde{\mu}\tilde{R}_{\text{out}}^0 = 0$ , which is readily solved for

$$\tilde{R}_{\text{out}}^0 = \frac{1}{\sqrt{2\tilde{\mu}}}. \quad (5.31)$$

We now turn to the constraint equation [Eq. (5.17)], which we solve for  $\mu$ . The zeroth order in  $\epsilon$  of the constraint equation is

$$\tilde{\mathcal{L}} = \int_1^{\tilde{R}_{\text{out}}^0} \frac{d\tilde{r}}{\tilde{d}_0} \tilde{r}, \quad (5.32)$$

yielding  $\tilde{\mu} = [2(\tilde{d}_0\tilde{\mathcal{L}}/\pi + 1)]^{-1}$ . Plugging this solution into Eqs. (5.28) and (5.31), we get the expressions of the displacement field and the outer radius at mechanical equilibrium:

$$\tilde{u}(\tilde{r}) = \frac{1}{2\tilde{r}} (\tilde{r} - 1) \left[ 1 - \frac{\tilde{r}}{(\tilde{R}_{\text{out}}^0)^2} \right]; \quad (5.33a)$$

$$\tilde{R}_{\text{out}}^0 = \sqrt{\tilde{d}_0\tilde{\mathcal{L}}/\pi + 1}. \quad (5.33b)$$

We conclude this section by providing the expression of the strain field  $u'(r)$  in the case of both giant and small toroids. The strain field of giant toroids is obtained from Eq. (5.33a), and reads

$$u'_{\text{giant}}(r) = \frac{\epsilon}{2} \left( \frac{R_c^2}{r^2} - \frac{R_c^2}{(R_{\text{out}}^0)^2} \right). \quad (5.34)$$

The strain field of small toroids can be obtained reproducing the minimization procedure described in this section, with the only difference that, in small toroids,  $R_{\text{out}} = R_c$  and  $R_{\text{in}}$  is free. This symmetry shows up in the final result, which is

$$u'_{\text{small}}(r) = \frac{\epsilon}{2} \left( \frac{R_c^2}{r^2} - \frac{R_c^2}{(R_{\text{in}}^0)^2} \right). \quad (5.35)$$

In both cases, we predict that inter-helical spacing  $d(r) = d_0 [1 + u'(r)]$  decreases with  $r$ , in qualitative agreement with the experiments.

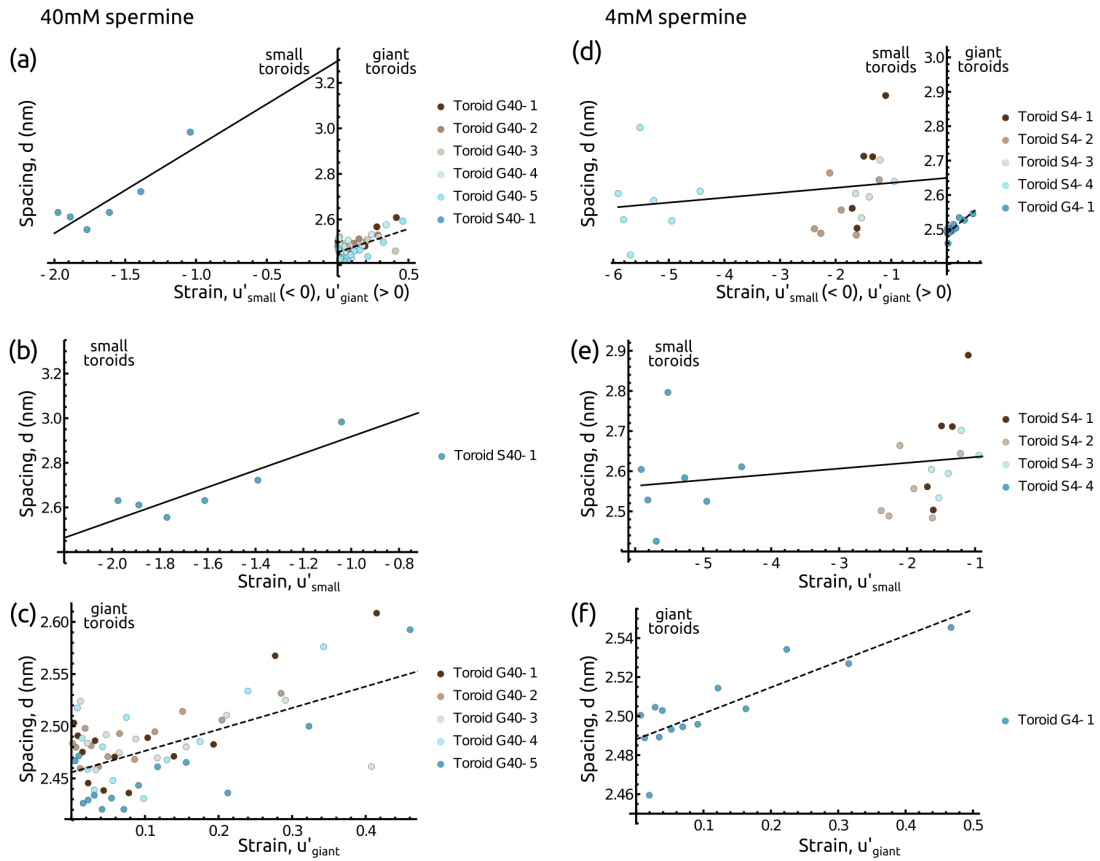


Figure 5.5: **Linear fit of collapsed datasets from small and giant toroids.** Toroids at (a-c) 40 mM and (d-f) 4 mM spermine. (a, d) Small and giant toroids in the same plot. (b, e) Small toroids only. (c, f) Giant toroids only. The linear relation used in the fits is  $d = d_0(1 + \epsilon u')$ , with  $d_0$  and  $\epsilon$  free parameters. Inferred parameters are provided in Tab. 5.1. Notice that the the strain  $u'$  is zero at  $R = R_c$  both in small toroids, where  $R_{\text{out}} = R_c$ , and in giant ones, where  $R_{\text{in}} = R_c$ . Toroid labels from Fig. 4.3.

4mM sp4+			
	$d_0$ (nm)	$\epsilon$	$\gamma$ (pN nm <sup>-2</sup> )
Small toroids	$2.65 \pm 0.03$	$0.005 \pm 0.004$	0.81
Big toroids	$2.49 \pm 0.01$	$0.050 \pm 0.010$	0.09
40mM sp4+			
	$d_0$ (nm)	$\epsilon$	$\gamma$ (pN nm <sup>-2</sup> )
Small toroids	$3.30 \pm 0.17$	$0.110 \pm 0.030$	0.02
Big toroids	$2.46 \pm 0.01$	$0.080 \pm 0.020$	0.06

Table 5.1: **Inferred parameters.** Four values of  $d_0$  and  $\epsilon$  inferred from four linear fits in Fig. 5.5. Corresponding values of  $\gamma$  from  $\gamma = k_b/\epsilon d_0^2 R_c^2$ , with  $R_c = 40$  nm and  $k_b = 40$  nm  $\times$   $k_B T$ .

## 5.4 Fitting the experimental data

In this section, we fit our model to the experimental data and infer the parameters of the inter-helical interaction potential: the stiffness  $\gamma$  and the optimal spacing  $d_0$ .

Notice that spacing  $d(r)$  depends linearly on  $u'_{\text{giant}}(r)$  and  $u'_{\text{small}}(r)$ , defined in Eqs. (5.34) and (5.35), respectively. This means that, in principle, the data points from small and big toroids can be collapsed on the same straight line. This can be done at fixed ionic conditions, because we know that cation-mediated interactions are sensitive to cation concentration [Sec. 3.1]. In Figs. 5.5a and 5.5d, we group the data in spacing vs.  $u'_{\text{giant}}(r)$  ( $u'_{\text{small}}(r)$ ) plots, using the values of inner ( $R_{\text{in}}^0$ ) and outer ( $R_{\text{out}}^0$ ) radius for each toroid from Fig. 4.3. We see that the points from small and big toroids are not aligned, the first being systematically shifted upwards. This is a consequence of small toroids being systematically less densely packed than big toroids, something we already knew from the experiments [Sec. 4.3].

As the data from small and big toroids are not aligned, we fit them independently. Our fitting parameters are  $d_0$  and  $\epsilon = k_b/\gamma d_0^2 R_c^2$ . We perform weighted least-square fits, by associating with each point a weight equal to the inverse of its variance. In this way, more precise points contribute more to the fit. We plot the best fit lines in Figs. 5.5a–5.5f and present the numerical values of the fitted parameters in Tab. 5.1. In calculating  $\gamma$  from  $\epsilon$ , we take  $R_c = 40$  nm and  $k_b = 40$  nm  $\times$   $k_B T$ . On a cautionary note, we stress that DNA persistence length may change by a factor of two because of the ionic environment [Guilbaud et al., 2019]. Since we are pursuing an order-of-magnitude estimate of  $\gamma$  here, we neglect this effect.

## Chapter 6

# Discussion

We conclude this part of the thesis dedicated to DNA toroids by discussing our results and proposing future perspectives.

In DNA toroids, inter-helical spacing correlates with curvature. In particular, helices that are close to the center of the assembly are more spaced than those that are far from it. We predict this behavior on the basis of a mechanical model, where DNA bending stiffness competes with inter-helical adhesive interactions. While interactions promote uniform spacing throughout the assembly, high curvature regions are energetically penalized by DNA rigidity. As a consequence, high curvature regions are less populated than low curvature ones, yielding higher local spacing in the former with respect to the latter.

A similar behavior was predicted by [Odijk and Slok \[2003\]](#) for DNA toroids confined in viral capsids in the absence of condensing cations, in which inter-helical forces are purely repulsive. Like us, they studied the mechanical equilibrium configuration resulting from the competition of elasticity and interactions. However, they used a specific form of inter-helical interaction potential, derived from Debye-Hückel theory, to predict the equilibrium inter-helical spacing dependence on position. Debye-Hückel cannot account for the attractive forces stabilizing our DNA condensates and we have no prior knowledge on the form of the attractive interaction potential in our case. Our agnostic approach, based on the generic Taylor expansion around the minimum of the effective potential, allows us to do the opposite: to deduce interactions from the knowledge on spacing spatial variations.

In some toroids, spacing decreases with the distance from the center up to a point where it reaches a minimum, followed by a weak increase [Fig. 4.3]. One possible explanation is that some of the data were taken in regions where the twist of DNA is not negligible. In Sec. 5.1, we have shown that twist can redistribute local curvature, making it vary non monotonically going from the inner to the outer radius of the assembly and generating an analogous non monotonic spacing dependence on position. The twisted toroid model developed in Sec. 5.1 can be used to extrapolate different curvature distributions and enrich our model. Because this effect is weak and not systematically detectable from the datasets, we do not think it affects the rest of our conclusions.

We infer values of the inter-helical interaction potential stiffness  $\gamma$  between  $10^{-2}$  and  $1 \text{ pNnm}^{-2}$ , which do not show any apparent dependence on either curvature or spermine concentration. These numbers can be compared with estimates obtained from two previous experimental and numerical works [[Todd et al., 2008](#); [Yoo and Aksimentiev, 2016](#)]. These two works infer inter-helical forces in agreement with each

other, studying spermine-condensed DNA in the presence of  $\text{Na}^+$  concentrations similar to ours, but in the absence of the divalent ions  $\text{Mg}^{2+}$  and  $\text{Ca}^{2+}$ , which are present in our experiments. These divalent ions are known to oppose DNA condensation [Tongu et al., 2016], so we expect helices to adhere less strongly in our case. Yoo and Aksimentiev [2016] estimate that the pair potential between two parallel DNA helices has a stiffness of  $\approx 10 \text{ pN nm}^{-1}$  per helical turn, close to the equilibrium point (see Fig. 4D in that article). If we approximate a DNA molecule as a chain of independent rigid sticks, with length  $\ell_p = 40 \text{ nm}$ , we can say that two such sticks belonging to parallel DNA molecules are connected by a spring with stiffness  $\gamma \times \ell_p \simeq 4 \text{ pN nm}^{-1}$ , where we used  $\gamma \simeq 0.1 \text{ pN nm}^{-2}$  from big toroids [Tab. 5.1]. Since a helical turn is about 3 nm long, each rigid stick contains  $40/3 \simeq 13$  helical turns, yielding a stiffness per turn  $\gamma \ell_p / 13 \simeq 0.3 \text{ pN nm}^{-1}$ . We infer a much softer stiffness than Yoo and Aksimentiev [2016], as expected on account of the presence of  $\text{Mg}^{2+}$  and  $\text{Ca}^{2+}$  in our experiments.

Although the presence of  $\text{Mg}^{2+}$  and  $\text{Ca}^{2+}$  can partially justify the soft adhesion between our helices, our current estimate of  $\gamma$  proves quite small even for our experiments. We can see this by asking whether the typical standard deviation of spacing data,  $\simeq 0.04 \text{ nm}$  in big toroids<sup>1</sup>, is consistent with thermal fluctuations in a parabolic trap with stiffness  $\gamma \ell_p$ . To address this question, we first check whether room temperature thermal fluctuations have the time to relax during the cooling process, required to vitrify water and have the sample ready for the electron microscope. Samples are cooled down from 300 K to 91 K with a speed of  $10^5 \text{ K sec}^{-1}$ , yielding a cooling time  $\tau_{\text{cooling}} \simeq 10^{-3} \text{ sec}$ . We now estimate the relaxation time of room temperature fluctuations in the harmonic trap of stiffness  $\gamma \ell_p$ . The spacing between two sticks is  $d_0(1 + \varepsilon)$ , where  $\varepsilon \simeq 0.1$  is the typical strain. Then, the typical force experienced by two interacting sticks in a toroid is  $\gamma \ell_p d_0 \varepsilon \simeq 1 \text{ pN}$ . Combining this value with water viscosity  $\eta = 10^{-3} \text{ Pa sec}$  and a typical length of  $\ell_p = 40 \text{ nm}$ , we get a fluctuation relaxation time  $\tau_{\text{relaxation}} = \eta \times \ell_p / \gamma \ell_p \simeq 10^{-8} \text{ sec} \ll \tau_{\text{cooling}}$ , implying that room temperature fluctuations do have the time to relax during the cooling process. We now estimate what the typical length scale of inter-helical spacing thermal fluctuations is at 91 K. This length scale is related to the ratio between thermal energy and the typical force between two interacting DNA sticks through  $k_B T / \gamma \ell_p d_0 \varepsilon \simeq 1 \text{ nm}$ . This value is much higher than the typical standard deviation of our spacing data. One source of error may be that the pressure felt by one helix is due to six neighbors rather than a single one, given the hexagonal packing. This consideration reduces the previous estimate to  $\simeq 0.2 \text{ nm}$ , still quite high, suggesting that we may have slightly underestimated  $\gamma$ .

As we illustrated in Sec. 4.3, DNA helices are more spaced in small than in big DNA toroids. This is the opposite of what we would expect on the basis of elasticity only, because helices are more curved in small than in big toroids, and should therefore push against each other more strongly in the former than in the latter case. Let us step back from the working hypothesis that the interaction potential is the same everywhere, independently of local curvature. In Sec. 4.2, we illustrated that the grooves of neighboring DNA helices correlate in a very specific way in DNA bundles. This behavior can be interpreted on the basis of the microscopic theories of inter-helical adhesive interactions [Ch. 3], that support the idea that helices need to be properly aligned for their adhesion to be optimal. Correlations are so important for inter-helical adhesion that, in toroidal bundles, helices exhibit a periodic over- and under-twist that makes groove correlation possible in the curved geometry of the assembly [Leforestier

<sup>1</sup>This number comes from non raw datasets that are not included in the manuscript.

and Livolant, 2009]. However, in Sec. 4.2 we have also shown that grooves correlate differently in straight and toroidal bundles, as if inter-helical forces could re-adapt depending on local curvature. In conclusion, given that groove correlation depends on curvature, inter-helical forces should depend on curvature as well. It is possible that the repulsive component of the interaction potential is more pronounced at high curvature, making the equilibrium spacing  $d_0$  increase.

Our study paves the way for several possible future directions. A systematic study of how the interaction between two helices depends on their curvature should be possible by using molecular dynamics simulations. These simulations could also reveal how groove correlations adapt to curvature. Concerning groove correlations, progress could be made by analyzing the existing datasets of toroid top views. In the past, Leforestier and Livolant [2009] measured the variation of the helical pitch along the length of one helix in a toroid. The pitch appeared to undergo periodic variations, showing alternating under- and over-twisted helical segments [Fig. 4.1i]. This measure could be repeated for many helices at different positions in a toroid, so as to measure how such periodic pitch modulation depends on local curvature. We expect the modulation amplitude to decrease as curvature decreases. It should also be possible to rationalize curvature-induced pitch modulations by means of a minimal analytical model. Our idea is to model a DNA helix as a chain of beads and springs, in which beads model DNA minor and major grooves (whose size difference we neglect). Two parallel DNA helices want to keep their grooves as in register as possible. If the chains are curved, like those in a toroid, beads cannot be in register without locally deforming the springs [Fig. 6.1]. Can the competition between the tendency of beads to align and spring rigidity generate periodically compressed and stretched regions along each chain, corresponding to the under- and over-twisted regions observed in DNA? How does the stability of the system change with curvature? This simple model, which is reminiscent of the Frenkel-Kontorova model of nonlinear physics [Chaikin and Lubensky, 1995], could predict quite a reach phenomenology.

In conclusion, we inferred cation-mediated forces between DNA helices from geometrical data on DNA toroidal bundles. We predict that curvature weakens inter-helical adhesion, which may apply to physiological DNA condensates. We hope the influence of curvature on inter-helical forces will be addressed in future studies, and that experimental progress will allow to clarify the influence of curvature on groove correlations.

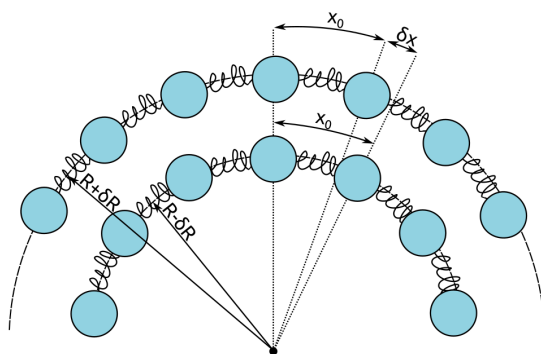


Figure 6.1: **Curvature hinders beads' alignment.** The two chains are composed of springs with the same resting length,  $x_0$ . Curvature generates a mismatch  $\delta x/x_0 = (R + \delta R)/(R - \delta R) - 1$  between the two helices, making it impossible to simultaneously align all the beads without deforming the springs.

**Part II**  
**ESCRT-III**

## Chapter 7

# Membrane budding away from the cytoplasm

The Endosomal Sorting Complexes Required for Transport (ESCRT) constitute an evolutionary conserved protein machinery that catalyzes membrane fission from within membrane necks in all known cellular processes requiring such kind of fission event, in eukaryotes and archaea. For instance, ESCRT is involved in HIV release from the plasma membrane [Cashikar et al., 2014], in the cytokinetic bridge constriction during cell division [Guizetti et al., 2011] and in the formation of multivesicular bodies (MVBs) [Babst et al., 2002] [Fig. 7.1a]. Excellent reviews on the ESCRT role and functioning are Schöneberg et al. [2016]; Chiaruttini and Roux [2017]; Christ et al. [2017]. The ESCRT machinery is composed of cytosolic protein complexes, labelled as ESCRT-0, -I, -II and -III, which cooperate with accessory proteins to perform membrane remodeling and severing. Notably, they cooperate with the ATPase Vps4, which is involved in the disassembly of ESCRT-III [Mierzwa et al., 2017; Pfitzner et al., 2019]. ESCRT-III participates in all ESCRT-mediated processes and is arguably the most important complex for the membrane remodeling part of ESCRT action. The architecture of ESCRT-III does not intuitively suggest how this complex catalyzes membrane remodeling and fission, which is currently under debate.

ESCRT-III is composed of four core subunits, which co-assemble into higher order structures. The subunit names depend on the cell they live in. In yeast, these are called Vps20, Snf7, Vps24 and Vps2. In mammals, their respective names are CHMP6, CHMP4, CHMP3 and CHMP2. ESCRT-III assembly can be nucleated by several proteins, among which ESCRT-II, which recruits Vps20 (CHMP6). After Vps20 (CHMP6) the other subunits are recruited in the order: Snf7 (CHMP4), Vps24 (CHMP3) and Vps2 (CHMP2) [Saksena et al., 2009].

ESCRT-III subunits form polymers of various shapes, like flat spirals [Figs. 7.2a, 7.2d], helices or conical helices [Figs. 7.2e]. Polymerization takes place both in solution [Lata et al., 2008; Henne et al., 2012; Shen et al., 2014] and on membrane substrates [Chiaruttini et al., 2015; McCullough et al., 2015]. ESCRT-III polymers are often double-stranded: Snf7 spirals [Fig. 7.2d], CHMP1B/IST1 helices [Fig. 7.2e] and Snf7/Vps24 heteropolymers [Banjade et al., 2019] are well characterized examples.

Can ESCRT-III polymers leverage their curvature to reshape membranes? Ten years ago, Lenz et al. [2009] have proposed an elastic model to explain how Snf7 spirals can tubulate flat lipid bilayers [Fig. 7.3]. This flat-to-tubular transition has been

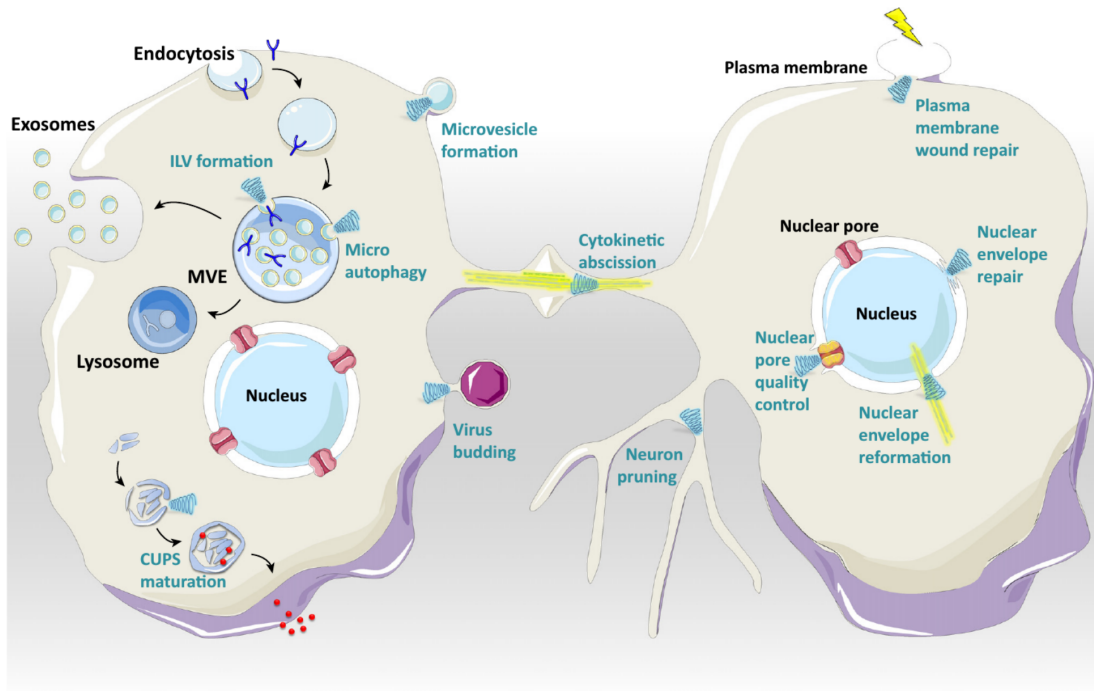
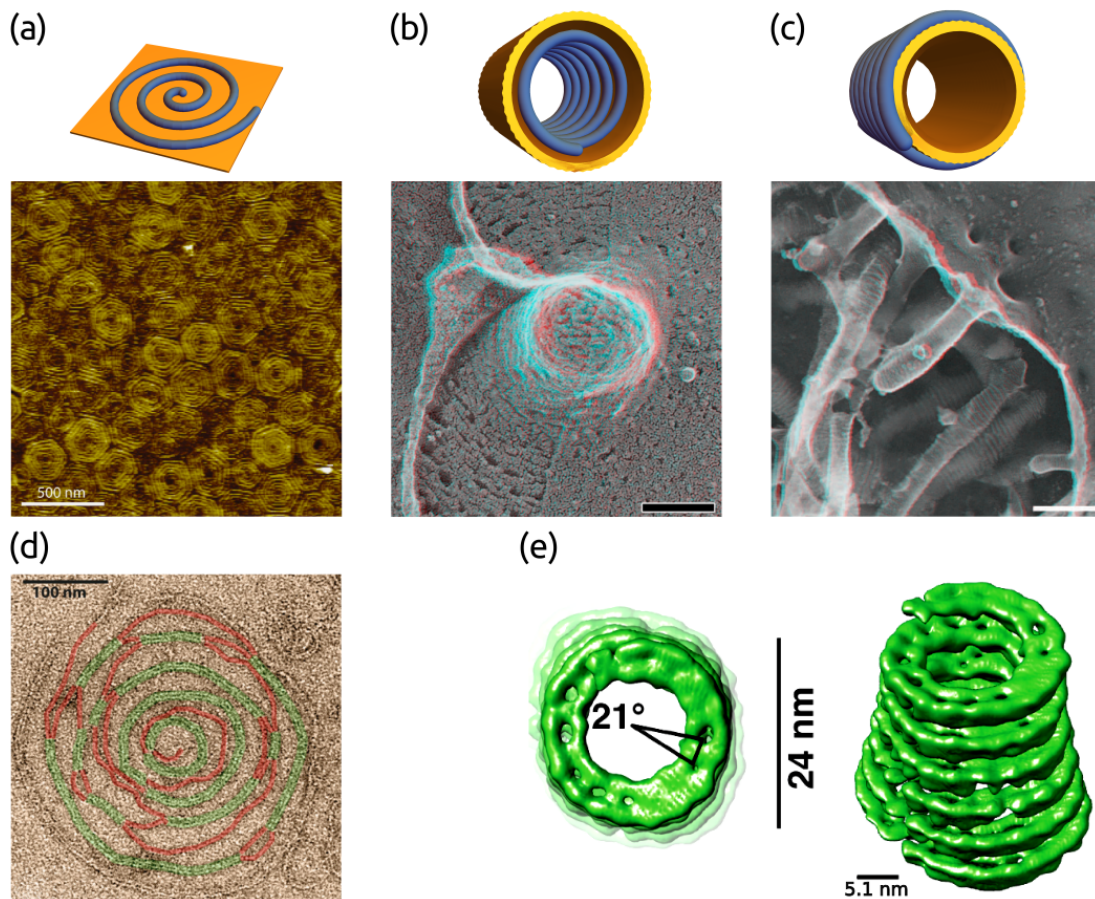


Figure 7.1: **The ESCRT-III protein complex.** Pictorial representation of some cellular phenomena where ESCRT-III (depicted as a blue helix) is known to be involved. Reprinted from Christ et al. [2017], with permission from Elsevier.

observed in COS-7 cells<sup>1</sup> overexpressing Snf7 in the presence of an ATP-hydrolysis deficient mutant of Vps4 [Fig. 7.2b, Hanson et al. 2008]. The essential physical ingredient here is that flat spirals are elastically unstable, and can relax by growing out of plane, thus driving membrane tubulation. What makes spirals unstable? Experiments suggest that Snf7 homopolymers have a preferred radius of curvature of 25 nm [Chiaruttini et al., 2015]. In a spiral, the polymer segment close to the inner radius  $r_i$  is over-bent, while the segment close to the outer radius  $r_e$  is under-bent, leaving the polymer optimal curvature only accessible halfway between  $r_i$  and  $r_e$  [Fig. 7.3a]. As a consequence, a flat spiral stores elastic energy that can be released by growing out of plane, shaping a membrane tube adapted to the preferred curvature of Snf7 [Figs. 7.3b, 7.3c].

The minimal model described above assumes no change in Snf7-membrane interaction during the buckling transition. We now discuss why this may be an oversimplifying assumption, that misses a crucial aspect of the ESCRT-III membrane remodeling ability. ESCRT-III polymers are usually equipped with a continuous membrane-binding interface running along their length, consisting of exposed, positively charged protein residues that attract negatively charged phospholipids [Tang et al., 2015]. Depending on the preferred direction of curvature relative to the positioning of the membrane-binding interface along the surface of ESCRT-III polymers, various membrane shapes can be induced. For example, Vps24 and Vps2 form helices that expose their membrane-binding interface on their exterior, and are thus able to stabilize membrane bilayer tubes by binding to their inner leaflet [Lata et al., 2008]. Similarly, Snf7/Vps4 or CHMP4A helices stabilize membrane tubes from the *lumen* (*i.e.*, from the tubes' in-

<sup>1</sup>A cell derived from monkey kidney tissue.



**Figure 7.2: ESCRT-III shapes and shaped tubes.** (a) Snf7 spirals on a flat membrane substrate. *Reproduced from Chiaruttini et al. [2015]. Figure licensed under CC BY-NC-ND 4.0.* (b) Membrane tube protruding away from the cytoplasm in cells coexpressing hSnf7-1 and an ATP-deficient mutant of VPS4B [VPS4B(E235Q)-GFP]. A spontaneous tear along the membrane surface reveals the underlying polymer scaffold. Scale bar, 100 nm. *Republished with permission of Rockefeller University Press, from Hanson et al. [2008]; permission conveyed through Copyright Clearance Center, Inc.* (c) Membrane tubes protruding towards the cytoplasm in a cell expressing CHMP1B. Scale bar, 100 nm. *From McCullough et al. [2015]. Reprinted with permission from AAAS.* (d) Snf7 spiral on membrane substrate. Single-stranded and double-stranded domains are colored in red and green, respectively. *Reproduced from Chiaruttini et al. [2015]. Figure licensed under CC BY-NC-ND 4.0.* (e) Top and side view of a CHMP1B/IST1 conical helix. The helix is double-stranded and there is a  $21^\circ$  rotation between individual subunits. *From McCullough et al. [2015]. Reprinted with permission from AAAS.*

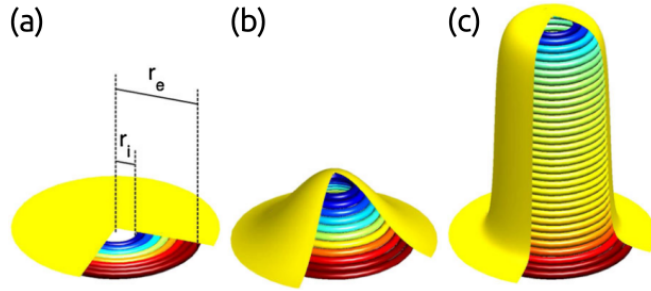


Figure 7.3: **Lenz model of ESCRT-mediated membrane buckling.** (a) A polymer spiral is over-bent (blue) close to its inner radius  $r_i$  and under-bent (red) close to its external radius  $r_e$ . (b, c) The spiral releases its bending energy by growing out of plane, shaping a tube with radius compatible with the optimal curvature of the polymer (yellow). Figures reproduced from Lenz et al. [2009], with permission from APS and the authors.

ner volume) as well [Fig. 7.2b, Hanson et al. 2008]. This is thought to be the physiological configuration of ESCRT-III polymers, which are only known to work from the lumen of membrane necks. Strikingly, CHMP1B and IST1 assemble into helices that expose their membrane-binding interface on their interior, and are thus able to stabilize bilayer tubes by binding to their outer leaflet [Fig. 7.2c, McCullough et al. 2015]. Although this is a physiologically unexpected behavior, it proves a certain richness of ESCRT-III membrane-deforming abilities.

What are the implications of the preferred membrane-binding direction of ESCRT-III in the spiral-to-tubular transition described earlier? Šarić and coworkers have recently addressed this question, by using molecular dynamics simulations [Harker-Kirschneck et al., 2019]. In their simulations, ESCRT-III polymerizes with a preferred radius of curvature  $R$  and tilt angle  $\alpha$  between its membrane-binding interface (colored in blue) and its direction of curvature [Fig. 7.4a]. In Fig. 7.4b, we show the outcome of a simulation that starts with an ESCRT-III flat spiral grown on a membrane bilayer. Before describing the evolution of the simulation, we mention the two sources of frustration that a flat spiral has in this model. One is the driver of tubulation in the aforementioned model by Lenz et al. [2009], *i.e.* the locally under- and over-bent regions along the spiral length. The other, unique to this model, is that a flat spiral can only be realized at  $\alpha = 0^\circ$ . At time zero in the simulation, this latter source of frustration is turned off by setting the spontaneous  $\alpha = 0$ . Interestingly, spirals grown on flat bilayers with  $\alpha = 0$  do not lead to tubulation in these simulations. As soon as the frustration is turned on, by setting the spontaneous  $\alpha \neq 0$ , the spiral can drive tubulation. The sign of  $\alpha$  determines whether the polymer stabilizes membrane necks from their inner or outer leaflet [Fig. 7.4b].

Harker-Kirschneck et al. [2019] have also explored how dynamic structural transitions between non-tilted and tilted resting states can lead to membrane fission, a process that has not been clarified by Lenz et al. [2009]. To do so, they have simulated how ESCRT-III could drive the budding of a cargo from a membrane bilayer, which is one of the services delivered by ESCRT in cells [Teis et al., 2010]. In their model system, the cargo is a sphere whose surface adheres to the membrane, but not enough to drive spontaneous budding. They grow an ESCRT-III spiral around the cargo, which should mimic the physiological recruiting of ESCRT-III [Teis et al., 2010]. During the recruiting process, the spiral has a  $\alpha = 0$  resting state. By transitioning to a  $\alpha > 0$  rest-

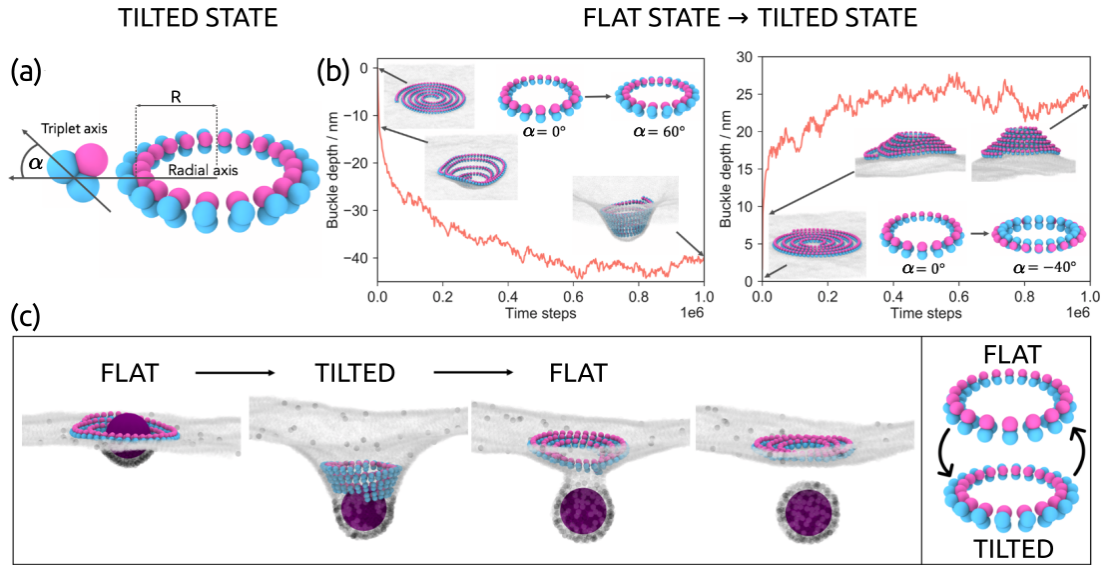


Figure 7.4: **Šarić model of ESCRT-mediated membrane buckling.** (a) ESCRT-III monomers are modeled as triplets, with two membrane binding units (blue), that copolymerize with a spontaneous radius of curvature  $R$  and tilt angle  $\alpha$ . (b) Molecular dynamics simulation in which a flat spiral with  $\alpha = 0^\circ$  at time zero switches to  $\alpha = 60^\circ$  (left) or  $\alpha = -40^\circ$  (right), driving membrane tubulation in two different directions. (c) Molecular dynamics simulation in which two consecutive shape transitions, flat  $\rightarrow$  tilted  $\rightarrow$  flat, drive cargo budding. *Figures reproduced from Harker-Kirschneck et al. [2019], with minor modifications to the labels. Figures licensed under CC BY-NC-ND 4.0.*

ing state, the spiral stabilizes the neck of a membrane protrusion in which the cargo is sequestered [Fig. 7.4c]. Strikingly, a further transition to the  $\alpha = 0$  resting state constricts the neck enough for thermal fluctuations to drive its closure and complete the cargo release.

In the field, there is more than one subscriber to the idea that dynamic shape transitions are the secret behind ESCRT-mediated membrane scission. Chiaruttini and Roux [2017] have suggested that an ESCRT-III polymer may undergo a dynamic shape transition if its subunits are dynamically exchanged, a job that the ATP-ase Vps4 seems to be able to do [Mierzwa et al., 2017; Pfitzner et al., 2019]. In fact, earlier in this section we have illustrated how different ESCRT-III subunits assemble into polymers with different shapes and membrane-binding preferences.

In this part of the thesis, we present experiments that prove previously unexpected membrane-binding capabilities of ESCRT-III. In Ch. 8, we show that three ESCRT-III units: Snf7, Vps24 and Vps2 copolymerize into helices that stabilize helical membrane tubes by binding to their outer lipid layer [Fig. 8.1g, 8.1i]. Helical tubes constitute an unusual shape for membranes, because they cost more bending energy than the fairly straight tubular protrusions discussed so far. However, differently than the ESCRT-III helical polymers mentioned above, Snf7/Vps24/Vps2 helices never shape straight membrane tubes. Why? We address this question in Ch. 9, where we show that the mechanical stability of helical tubes can be explained by the existence of two separate membrane-binding interfaces along Snf7/Vps24/Vps2 polymers (like in a more sophisticated version of Harker-Kirschneck et al. 2019). Specifically, we show that the stability of helical tubes relies on the asymmetric membrane-binding energy between

these two interfaces. Furthermore, we infer bounds on the bending and torsional rigidities of Snf7/Vps24/Vps2 helices. Finally, in Ch. 10, we discuss some biological implications of our findings, also in the context of the theoretical models proposed above.

# Chapter 8

## Experiments

### Contents

---

8.1	ESCRT-III filaments stabilize helical membrane tubes . . . . .	57
8.2	Polar and equatorial filaments . . . . .	59
8.3	Tube-less helices . . . . .	59
8.4	Summary and relevant data . . . . .	62

---

In this chapter, we present experimental results obtained by Joachim Moser Von Filseck and Aurélien Roux at the University of Geneva, in collaboration with Nathaniel Talledge, Isabel Johnson and Adam Frost from the University of California San Francisco. All figures are reproduced from our joint manuscript, [Moser Von Filseck et al. \[2019\]](#). We deliberately omit many details about the experiments in the following, since these are not key to our analysis.

The ESCRT-III subunits available in the samples are Snf7, Vps24, Vps2. As we illustrate, these three subunits co-assemble into helical polymers that are able to reshape membrane vesicles into helical tubes. For simplicity, we generically refer to these polymers as Snf7/Vps24/Vps2. However, we cannot exclude that the different polymers in the sample have different stoichiometry. Unfortunately, such information is not accessible from the experiments presented here.

In Sec. 8.1, we show the helical tubes into which membrane vesicles are deformed by the action of Snf7/Vps24/Vps2 helices. Two dimensional images of the samples are obtained by either transmission electron microscopy (TEM), upon negative staining, or Cryo-EM. Three-dimensional reconstructions of some helical tubes are obtained by cryo-electron tomography (Cryo-ET). In Sec. 8.2, we show that Snf7/Vps24/Vps2 filaments are double-stranded and spatially segregated on the outer surface of helical tubes. Moreover, we illustrate that these filaments cluster into three groups, suggesting that they are equipped with two different membrane-binding interfaces and can be divided into two groups, that we call *polar* and *equatorial*. Finally, in Sec. 8.3 we show the resting configuration of Snf7/Vps24/Vps2 helices when these are grown in the absence of membrane tubes, which can be solubilized by a detergent.

### 8.1 ESCRT-III filaments stabilize helical membrane tubes

Vps24 and Vps2 are added to spherical bilayer vesicles incubated with Snf7 and decorated by flat Snf7 spirals [[Chiaruttini et al., 2015](#); [Mierzwa et al., 2017](#)]. Upon several hours of incubation, a mixture of vesicles coated by flat spirals [Fig. 8.1a, 8.1d] and

## Membrane + Snf7 + Vps2 + Vps24

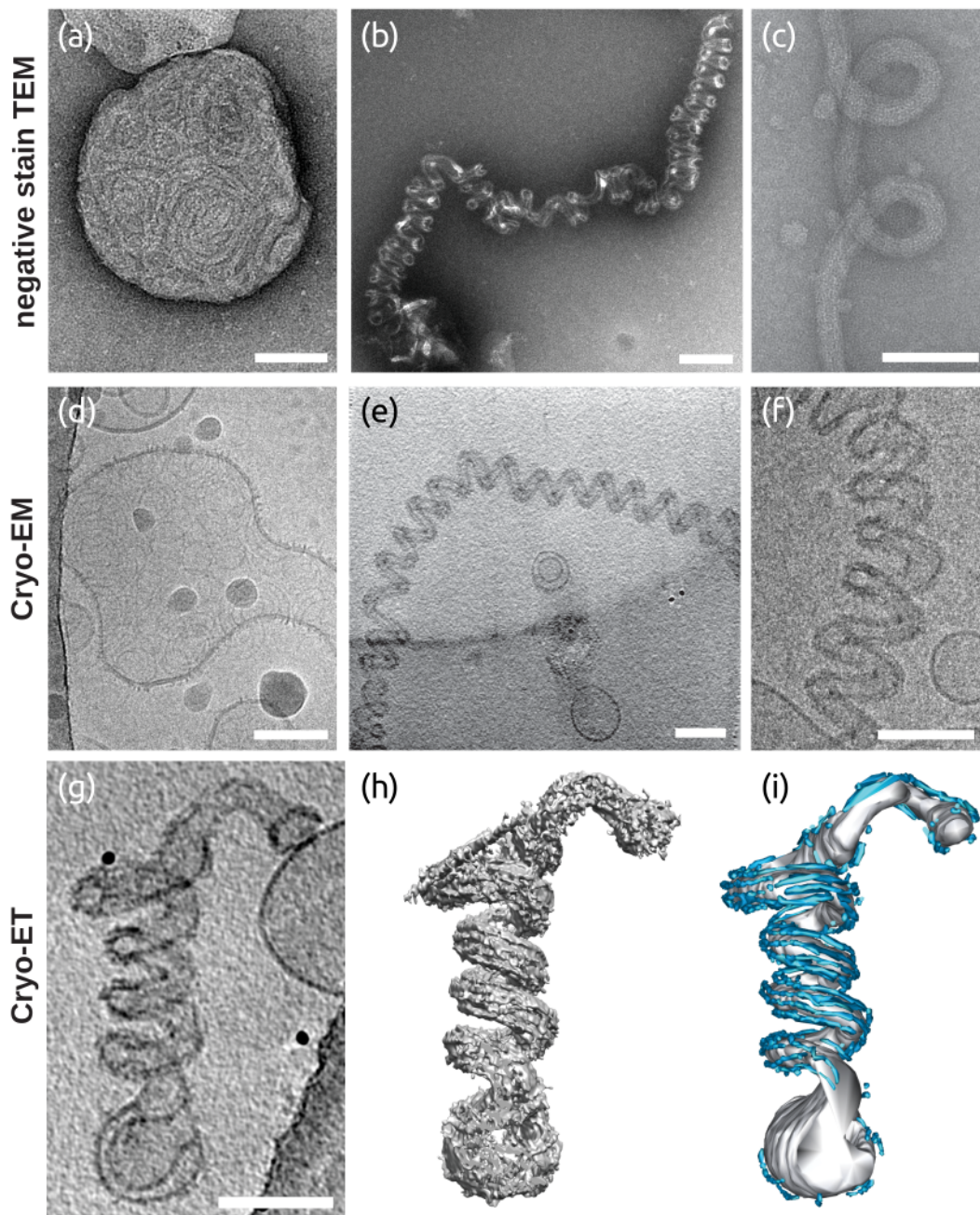


Figure 8.1: **Helical tubulation of spherical membrane vesicles by ESCRT-III heteropolymers.** (a, d) Electron micrographs showing undeformed large unilamellar vesicles (LUVs), coated by flat Snf7 spirals. (b, c, e, f) Electron micrographs showing helical membrane tubes coated by Snf7/Vps24/Vps2 on negatively stained (b, c) and vitrified (e, f) samples. (g,h,i) Reconstructed cryo-ET volume of a helical membrane tube, projected (g) and volume view (h-i), showing the organization of protein filaments (cyan) along the helical membrane tube (gray). Scale bars, 100 nm.

helical membrane tubes coated by helical filaments [Figs. 8.1b, 8.1c, 8.1e, 8.1f] is observed. Helical membrane tubes only form in the presence of all three proteins, and their number increases with incubation time. They exhibit a regular shape, with an average tubular diameter of  $23.9 \pm 3.7$  nm, outer diameter of  $82.3 \pm 6.1$  nm and pitch of  $53.1 \pm 7.6$  nm, where uncertainties are standard deviations.

To visualize the ESCRT-III filament organization on the surface of the helical tubes, cryogenic electron tomography (cryo-ET) on vitrified helical membrane tubes is performed. Six to eight filaments running parallel to the tube axis and almost always segregated on the outer region of the tube, far from the helical axis, are observed [Figs. 8.1g, 8.1h, 8.1i]. The filaments' thickness is compatible with that of negatively stained, double-stranded Snf7/Vps24/Vps2 heteropolymers,  $4.9 \pm 0.5$  nm [Mierzwa et al., 2017].

## 8.2 Polar and equatorial filaments

The local structure of these filaments is reconstructed at 3.2 nm resolution by subtomogram averaging (STA), revealing three well separated filament clusters [Fig. 8.2a]. The central cluster, containing two filaments, covers a 13 nm wide region around the equator of the tube (*equatorial filaments*, blue). Two additional filament clusters, each containing 2 to 3 filaments, are shifted up and down from the equator, respectively, (*polar filaments*, red) and appear wider (16 to 20 nm) [Figs. 8.2b – 8.2d]. The resolution of the polar filaments is limited, as their positions vary more with tube diameter compared to the equatorial region. With further STA focused on the equatorial cluster, each of the two equatorial filaments is shown to be made of two strands [Figs. 8.2e, 8.2g]. The filaments in the polar clusters, based on their thickness, could be double-stranded as well, although it is not possible to resolve their substructure.

Overall, the architectures of equatorial and polar filaments appear to be similar: both are composed of at least two double-stranded filaments, possibly bundled together as a helical ribbon along the surface of the tube. However, while polar filaments curve perpendicular to their membrane-binding direction, equatorial filaments curve towards their membrane-binding direction. In this respect, polar filaments are reminiscent of the double-stranded spirals formed by Snf7 on flat membranes [Fig. 7.2d, Chiaruttini et al. 2015] ( $\alpha = 0^\circ$  case in Figs. 7.4a, 7.4b), while equatorial filaments are reminiscent of the double-stranded helices formed by IST1 and CHMP1B around straight membrane tubes [Fig. 7.2e, McCullough et al. 2015] ( $\alpha = -90^\circ$  case in Figs. 7.4a, 7.4b). This suggests that polar and equatorial filaments engage membrane with a different interface and, as a consequence, bundle along a different direction [Fig. 8.2h].

## 8.3 Tube-less helices

The mechanical equilibrium between membrane helical tubes and ESCRT-III filaments relies on the balance between the tube's tendency to straighten and the filaments' ability to keep it helical. To analyze the preferred geometry of the helical filaments in the absence of a membrane tube, Snf7/Vps24/Vps2 filaments are grown in the presence of detergent, which removes membrane. Helical ribbons form without membrane tubes during detergent removal. Most of these tube-less helical ribbons assemble into sharp zigzag shapes [Fig. 8.3a], a smaller population appears sinusoidal [Fig. 8.3b], and

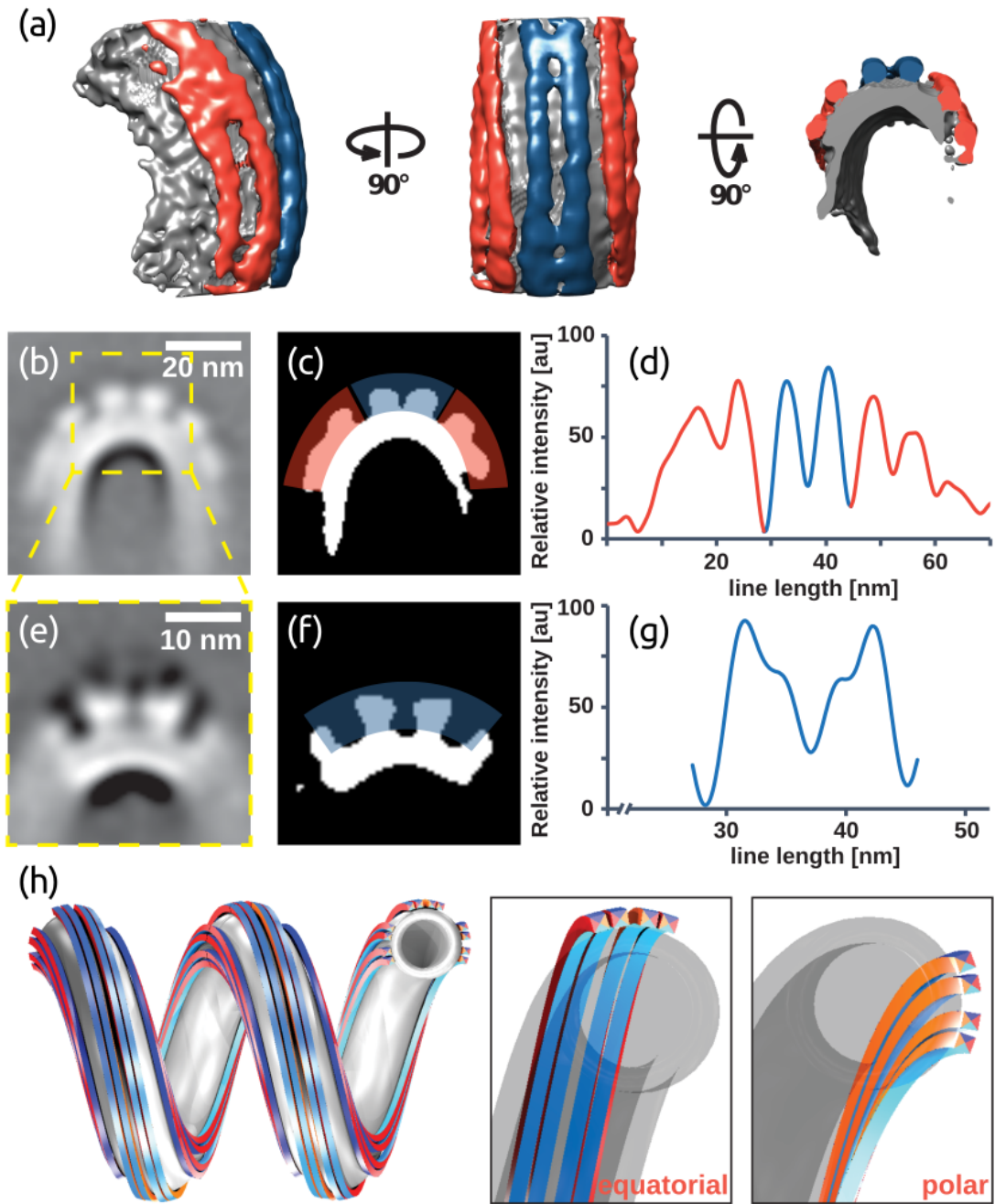


Figure 8.2: **ESCRT-III filament bundles form distinct clusters on the surface of helical tubes.** (a) Side view (left), top view (center) and cross-section (right) of a global subtomogram average showing filaments following the tube axis, in the equatorial (blue) and polar (red) binding mode, respectively. (b) Sum projection of a central segment of the tube in (a) showing filaments on the outer surface of the helical tube, organized as one equatorial and two polar clusters. Scale bar, 20 nm. (c) Equatorial (blue) and polar (red) filament cluster highlighted on the thresholded image (b). (d) Intensity profile of protein density in (c). (e) Projection of a refined map of the equatorial cluster showing that both filaments of the cluster are made of two strands each. Scale bar, 10 nm. (f) Thresholded image of (e). (g) Intensity profile of protein density in (e). (h) 3D model of two equatorial and four polar filaments, each double-stranded, on a helical membrane tube (grey). All filaments are identical, except that equatorial and polar filaments bind the membrane through the cyan and orange interfaces, respectively (insets). Filaments in the two hemispheres are shown as antiparallel.

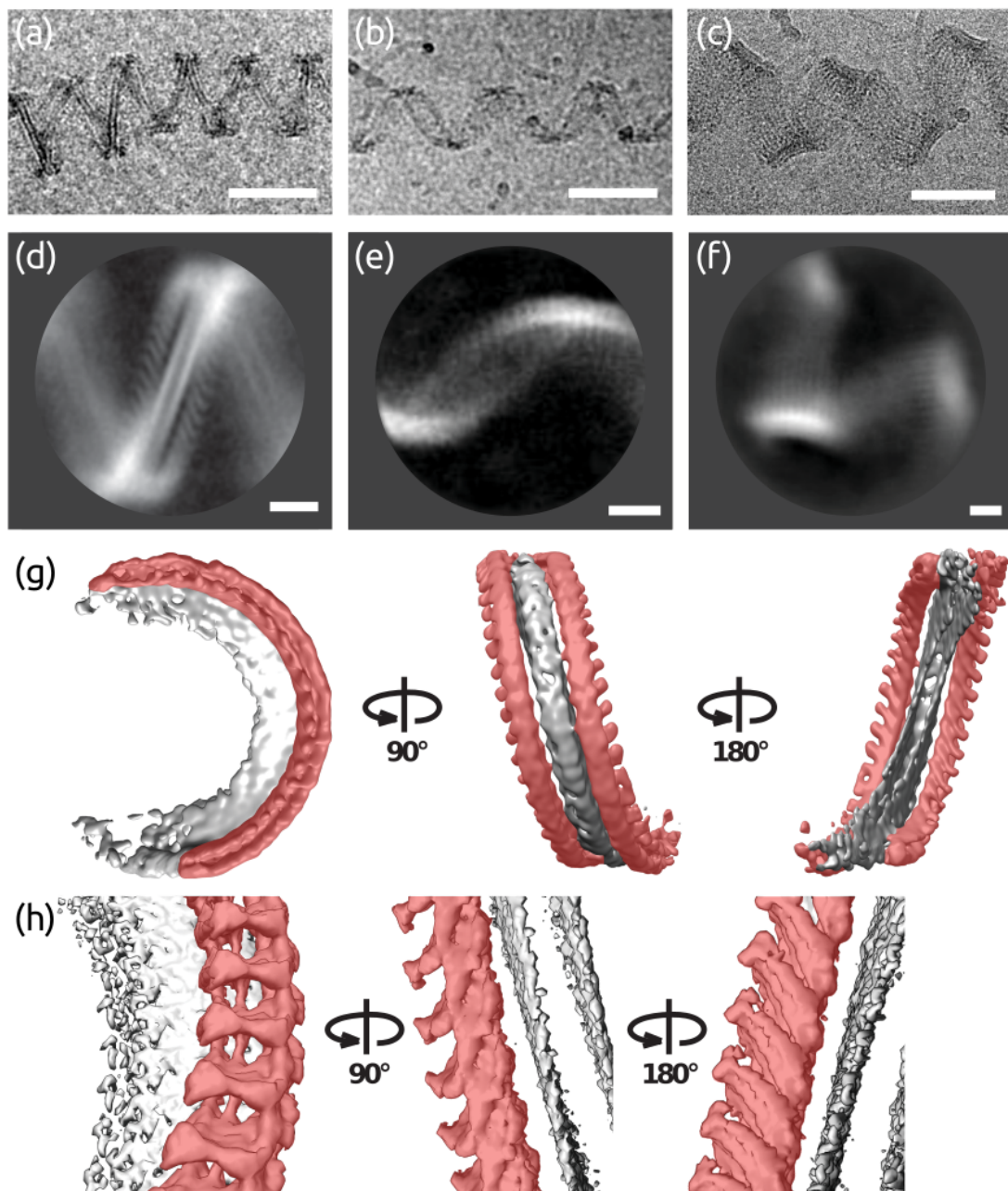


Figure 8.3: **Organization of tube-less ESCRT-III filaments.** (a, b, c) Electron micrographs (scale bars, 100 nm) and (d, e, f) 2D class averages (scale bars, 10 nm) showing different tube-less, helical ESCRT-III filament bundles formed upon detergent removal. The majority of ribbons adopts a zigzag shape (a, d), others appear sinusoidal (b, e) and a third set consists of helical ribbons with higher strand numbers (c, f). (g) 3D average of (a, d) shows that the center of the ribbon is a helical bicelle with its plane perpendicular to the tube axis (gray). There are two anti-parallel double-stranded filaments on both sides of the bicelle (red). (h) 3D average as in (a, c) that includes only one double-stranded filament (red).

Helical membrane tubes		
$r$ (nm)	$R$ (nm)	$P$ (nm)
$12.1 \pm 0.6$	$41.9 \pm 1.6$	$8.5 \pm 0.4$

Table 8.1: **Experimental parameters of membrane helical tubes.** Tubular radius  $r$ , radius  $R$  and pitch  $2\pi P$  defined in Fig. 9.1. Uncertainties are standard deviations.

a third ribbon population displays significantly larger ribbons with varying strand numbers and diameters [Fig. 8.3c]. 2D class averages of these tube-less helical protein filament ribbons are determined [Figs. 8.3d – 8.3f].

Analysis of the more ordered “zigzag” filaments leads to a 3D reconstruction at 1.5 nm resolution. This structure reveals a helical ramp formed around a membrane *bicelle*, *i.e.* a flat lipid bilayer whose perimeter is stabilized by detergents, with the bicelle plane oriented perpendicular to the helix axis. On both sides of the bicelle, filamentous polymers with dimensions consistent with other double-stranded ESCRT-III structures [McCullough et al., 2015; Mierzwa et al., 2017; Banjade et al., 2019] are observed. Considering the apparently anti-symmetric orientation of subunits lying on opposite sides of the bicelle, the resulting filaments on the two sides of the bicelle seem to have opposite polarity [Fig. 8.3g]. This is confirmed by a 3D reconstruction at a higher resolution (1.1 nm) that was computed by focusing on one side of the bicelle only [Fig. 8.3h]. The subunits appear to assemble into a double-stranded helical polymer reminiscent of previously described ESCRT-III architectures. Both strands seem to bind to the membrane and they curve perpendicular to their membrane-binding direction. The zigzag tube-less ribbon’s architecture is compatible with the polar filaments on helical tubes, and confirms that polar filaments are also double-stranded.

The overall appearance of sinusoidal ribbons [Figs. 8.3b, 8.3e] suggests that they comprise multi-stranded filaments that could orient along a helical path similar to that of the equatorial filaments bound to the helical membrane tubes.

## 8.4 Summary and relevant data

To conclude this chapter, we summarize the fundamental experimental findings that are used in the course of the theoretical modeling, in the next chapter.

Snf7/Vps2/Vps24 polymers reshape initially spherical bilayer vesicles into helical tubes. The average tubular radius, radius and pitch of helical tubes is provided in Tab. 8.1. Helical tubes are stabilized by a scaffold comprising, on average, six double-stranded helical filaments. The filamentous scaffold is subdivided into two clusters: the equatorial one, comprising two filaments, and two polar ones, comprising four filaments and located at symmetric sites above and below the equatorial cluster.

The resting configuration of Snf7/Vps2/Vps24 helices is revealed by growing them in the absence of membrane tubes. Among the tube-less helices, those reproducing the polar membrane-binding configuration are fairly distinguishable, revealing a 3 nm inter-monomer spacing. Helices possibly reproducing the equatorial membrane-binding configuration are also recognized, although with much less resolution. The average radius and pitch of polar and (putative) equatorial helices is provided in Tab. 8.2.

Tube-less helices			
Polar filaments		Equatorial filaments	
$R_0^R$ (nm)	$P_0^R$ (nm)	$R_0^B$ (nm)	$P_0^B$ (nm)
$23.4 \pm 0.6$	$6.6 \pm 0.2$	$17.1 \pm 2.5$	$8.9 \pm 1.4$

Table 8.2: **Experimental parameters of tube-less helices.** Preferred helical radius and pitch are denoted by  $R_0$  and  $2\pi P_0$ , respectively. Superscripts  $R$  (red) and  $B$  (blue) denote polar and equatorial filaments, respectively (color code from Fig. 8.2h). Uncertainties are standard deviations.

## Chapter 9

# Theoretical modeling

In this chapter, we study the mechanical stability of helical membrane tubes scaffolded by polymer helices, with the aim of addressing two questions emerging from the experiments described in the previous chapter.

In Sec. 9.1, we derive some results on the differential geometry of helical tubes that are used in the rest of the chapter.

Why do Snf7/Vps24/Vps2 helices systematically shape helical rather than straight membrane tubes? In Sec. 9.2, we propose that the experimental realization of exclusively helical tubes can be explained on the basis of an asymmetric membrane-binding energy of polar and equatorial filaments [Sec. 8.2]. We derive a phase diagram, in which the relative stability of straight and helical tubes scaffolded by Snf7/Vps24/Vps2 rigid helices are compared. From the phase diagram, we infer a lower bound on the difference in membrane-binding energy per monomer between polar and equatorial filaments.

How stiff are Snf7/Vps2/Vps24 helices? In Sec. 9.3, we answer this question by developing an elastic model in which a helical tube is stabilized by a semi-flexible scaffold of polar and equatorial Snf7/Vps24/Vps2 helices. By knowing from the experiments how much Snf7/Vps24/Vps2 helices deviate from their resting configuration when they stabilize helical tubes, we estimate a lower bound on the helices' bending rigidity from force balance equations. Furthermore, using a previous estimate of the bending rigidity, we estimate the actual torsional stiffness of Snf7/Vps24/Vps2 helices, as well as the actual membrane-binding energy difference between polar and equatorial monomers.

### 9.1 Preliminary: differential geometry of helical tubes

We model membrane tubes by means of the Helfrich free energy [Eq. (1.3)],

$$\mathcal{F}_{\text{Helfrich}} = \frac{\kappa}{2} \int_{\mathcal{A}} d\mathcal{A} (2H)^2 + \sigma \mathcal{A}. \quad (9.1)$$

Here, we parametrize a helical tube and obtain closed expressions for its differential area  $d\mathcal{A}$  and mean curvature  $H$ . At the end of this section, we compute the integral appearing in Eq. (9.1).

We first parametrize the center line of the helical tube. This center line is a regular helix with radius  $R - r$  and pitch  $2\pi P$  [Fig. 9.1]. Denoting by  $s \in [0, \mathcal{S} = 2\pi n \sqrt{(R - r)^2 + P^2}]$  its arc length, where  $n$  is the number of turns around the  $z$ -axis,

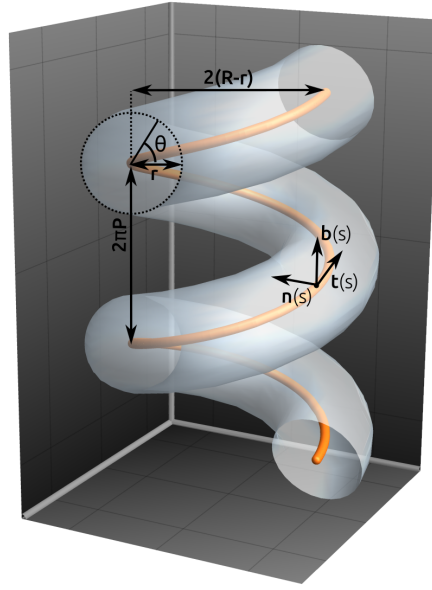


Figure 9.1: **Schematic of a helical tubular surface.** Center line is colored in orange.

its position vector is

$$\mathbf{h}(s) = R \left[ \cos \left( \frac{s}{\sqrt{(R-r)^2 + P^2}} \right) \hat{\mathbf{x}} + \sin \left( \frac{s}{\sqrt{(R-r)^2 + P^2}} \right) \hat{\mathbf{y}} \right] + \frac{sP}{\sqrt{(R-r)^2 + P^2}} \hat{\mathbf{z}}. \quad (9.2)$$

To parametrize the tubular surface, we take advantage of the co-moving frame of the curve  $\mathbf{h}$ , generated by its unit tangent  $\hat{\mathbf{t}}$ , normal  $\hat{\mathbf{n}}$  and binormal  $\hat{\mathbf{b}}$  [Fig. 9.1]:

$$\hat{\mathbf{t}}(s) = \partial_s \mathbf{h}; \quad \hat{\mathbf{n}}(s) = \frac{1}{c} \partial_s \partial_s \mathbf{h}; \quad \hat{\mathbf{b}}(s) = \hat{\mathbf{t}} \times \hat{\mathbf{n}}. \quad (9.3)$$

where  $c = (R-r)/[(R-r)^2 + P^2]$  is the curvature of  $\mathbf{h}(s)$ . The vectors in the co-moving frame are related through the Frenet – Serret formulas,

$$\begin{pmatrix} \partial_s \hat{\mathbf{t}} \\ \partial_s \hat{\mathbf{n}} \\ \partial_s \hat{\mathbf{b}} \end{pmatrix} = \begin{pmatrix} 0 & c & 0 \\ -c & 0 & \tau \\ 0 & -\tau & 0 \end{pmatrix} \begin{pmatrix} \hat{\mathbf{t}} \\ \hat{\mathbf{n}} \\ \hat{\mathbf{b}} \end{pmatrix}, \quad (9.4)$$

where  $\tau = P/[(R-r)^2 + P^2]$  is the torsion of  $\mathbf{h}(s)$ .

We define the position vector of the surface as

$$\boldsymbol{\Sigma}(s, \theta) = \mathbf{h}(s) + r \left[ \cos \theta \hat{\mathbf{n}}(s) + \sin \theta \hat{\mathbf{b}}(s) \right], \quad (9.5)$$

where  $r$  is the tubular radius and  $\theta \in [0, 2\pi]$  [Fig. 9.1]. Notice that the term in the square brackets is also the local unit normal  $\hat{\mathbf{N}}$  to the tubular surface,

$$\hat{\mathbf{N}}(\theta, s) = \frac{\partial_\theta \boldsymbol{\Sigma} \times \partial_s \boldsymbol{\Sigma}}{\|\partial_\theta \boldsymbol{\Sigma} \times \partial_s \boldsymbol{\Sigma}\|} = \cos \theta \hat{\mathbf{n}} + \sin \theta \hat{\mathbf{b}}. \quad (9.6)$$

We now proceed with the evaluation of the differential area  $d\mathcal{A}$  of the membrane surface. To do so, we introduce the covariant components of the *metric tensor* (also

called the *first fundamental form*) associated with the helical tube  $\Sigma(s, \theta)$ . These components are defined as  $g_{\alpha\beta} = \partial_\alpha \Sigma \cdot \partial_\beta \Sigma$ , where the indices can be either  $s$  or  $\theta$ , and result in:

$$g_{ss} = (1 - cr \cos \theta)^2 + (\tau r)^2; \quad (9.7a)$$

$$g_{s\theta} = g_{\theta s} = \tau r^2; \quad (9.7b)$$

$$g_{\theta\theta} = r^2. \quad (9.7c)$$

Denoting by  $g$  the determinant of the metric tensor, the differential area of the tubular surface reads

$$d\mathcal{A} = \sqrt{g} d\theta ds = r [1 - cr \cos \theta] d\theta ds, \quad (9.8)$$

yielding the total area

$$\mathcal{A} = \int_0^{\mathcal{S}} ds \int_0^{2\pi} d\theta \sqrt{g} = 2\pi r \mathcal{S}. \quad (9.9)$$

We now turn to the evaluation of the mean curvature  $H$  of the membrane surface. To do so, we introduce the covariant components of the *second fundamental form* associated with the membrane. These are defined as  $b_{\alpha\beta} = \partial_\alpha \partial_\beta \Sigma \cdot \hat{N}$ , and read:

$$b_{ss} = (1 - cr \cos \theta) c \cos \theta - r\tau^2 \quad (9.10a)$$

$$b_{s\theta} = b_{\theta s} = -r\tau \quad (9.10b)$$

$$b_{\theta\theta} = -r \quad (9.10c)$$

The mean curvature is obtained by tracing the second fundamental form

$$H(\theta) = \frac{1}{2} g^{\alpha\beta} b_{\alpha\beta} = \frac{1}{2} \left( -\frac{1}{r} + \frac{c \cos \theta}{1 - cr \cos \theta} \right), \quad (9.11)$$

where summation over repeated indices is implied and the  $g^{\alpha\beta}$  are the contravariant components of the metric tensor, which are defined such that  $g^{\alpha\gamma} g_{\gamma\beta} = \delta_\beta^\alpha$ , where  $\delta_\beta^\alpha$  is the Kronecker delta. The expression of the mean curvature in Eq. (9.11) is identical to that of a torus with tubular radius  $r$  and center line radius  $1/c$ . Notice that  $H(\theta = 0)$  diverges when  $r = 1/c$ , at which point the helical tube is too “fat” and self-intersects at  $\theta = 0$ . To avoid self-intersection, we restrict the tubular radius to  $0 < r < 1/c$  in the following.

Finally, we combine Eq. (9.8) and Eq. (9.11) to compute the bending energy integral appearing in Eq. (9.1):

$$\int_{\Sigma} d\mathcal{A} (2H)^2 = \int_0^{\mathcal{S}} ds \int_0^{2\pi} d\theta \sqrt{g} (2H)^2 = \frac{2\pi \mathcal{S}}{r \sqrt{1 - (cr)^2}}. \quad (9.12)$$

Notice that the bending energy explodes at  $r = 0$  and  $r = 1/c$ , and is thus bounded from below.

## 9.2 Straight or helical? A phase diagram for membrane tubes

In this section, we develop a minimal mechanical model with the aim of explaining why Snf7/Vps2/Vps24 helices systematically shape helical rather than straight membrane tubes.

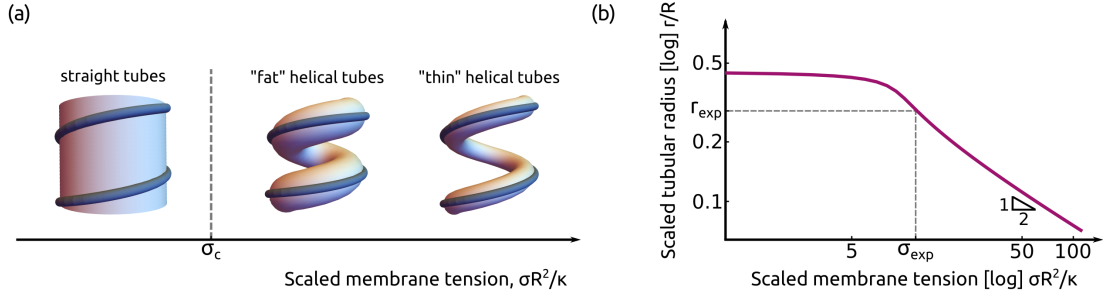


Figure 9.2: **Straight-to-helical tube transition via membrane tension.** (a) Phase diagram showing the energetically more favored shape between straight and helical tubes, as a function of the surface tension  $\sigma$ . The dashed gray line is the phase boundary. (b) The equilibrium tubular radius of a helical tube decreases with increasing surface tension.

We approximate the membrane scaffolding function of the filaments by a single, effective outer helix that fixes the outer membrane radius [Fig. 9.2a]. Notice that this effective helix includes all six double-stranded Snf7/Vps24/Vps2 filaments stabilizing helical tubes in the experiments [Fig. 8.2h]. We moreover assume that this scaffold is undeformable, consistent with the observation that Snf7/Vps24/Vps2 radius and pitch [Tab. 8.2] change only by a modest amount when membrane is added to them [Tab. 8.1]. The change is less than 30%, except for the radius of equatorial filaments, which, however, constitute only one third of the scaffolding filaments [Fig. 8.2h].

In Sec. 9.2.1, we only include in this model the energetic contribution coming from membrane elasticity. We show that the stability of helical over straight tubes can be caused by a high enough membrane tension  $\sigma$ . We calculate the critical tension  $\sigma_c$  and argue that the experimental tension  $\sigma_{\text{exp}}$  is below this critical value. Thus, we rule out that helical tubes in the experiments are stabilized by membrane tension only.

In Sec. 9.2.2, we enrich the model by introducing an energy term due to polymer membrane-binding. Specifically, we hypothesize an energy gain associated with Snf7/Vps24/Vps2 filaments binding the membrane through their polar rather than their equatorial interface. We show that such membrane-binding asymmetry between polar and equatorial filaments can explain the systematic selection of helical over straight tubes in the experiments. By using our estimate of experimental membrane tension  $\sigma_{\text{exp}}$  from Sec. 9.2.1, we infer a lower bound for the binding energy difference per monomer.

### 9.2.1 An instructive failure: helical tubes from high surface tension

In this section, we explain why helical tubes can be more stable than straight ones relying on membrane elasticity only. We model membrane elasticity with the Helfrich free energy [Eq. (9.1)], with  $\kappa \simeq 20 k_B T$  and no prior knowledge of  $\sigma$ .

Before going through the calculation, we anticipate why the competition between  $\kappa$  and  $\sigma$  can explain a straight-to-helical tube transition, in words. We can visualize the transition by looking at Fig. 9.2a. A helical tube is always more curved than a straight one. However, a thin enough helical tube may require less membrane area than a straight one. Surface tension  $\sigma$  penalizes membrane area, and can therefore compensate for the bending cost associated with a helical tube when the latter is thin enough. At mechanical equilibrium, we expect that the tubular radius  $r$  of a heli-

cal tube decreases with increasing membrane tension  $\sigma$  (proof below). Summing up, there should be a critical tension  $\sigma_c$  above which a helical tube is energetically more convenient than a straight one.

What is the critical surface tension  $\sigma_c$ ? We compare the free energy of straight and helical tubes for a fixed total length  $\mathcal{L}$  of helical filament scaffold of radius  $R$  and pitch  $2\pi P$ , such that  $\mathcal{L} = 2\pi n\sqrt{R^2 + P^2}$ , where  $n$  is the number of helical turns around the vertical axis. Approximating the straight tube to a cylinder, the membrane surface area is  $\mathcal{A}_{\text{cylinder}} = 2\pi R \times 2\pi P \times n$ , its mean curvature is  $H_{\text{cylinder}} = -1/2R$ , and Eq. (9.1) reduces to

$$\frac{\mathcal{F}_{\text{cylinder}}}{\mathcal{L}} = \frac{2\pi RP}{\sqrt{R^2 + P^2}} \left( \frac{\kappa}{2R^2} + \sigma \right). \quad (9.13)$$

Now considering the helical tube, we model the membrane as a tube of constant radius  $r$  with a helical center line. Using the result Eq. (9.12), this geometry yields the free energy

$$\frac{\mathcal{F}_{\text{helical}}(r)}{\mathcal{L}} = 2\pi \left[ \frac{P^2 + (R-r)^2}{P^2 + R^2} \right]^{1/2} \left\{ \frac{\kappa}{2r} \left[ 1 - \left( \frac{r(R-r)}{P^2 + (R-r)^2} \right)^2 \right]^{-1/2} + r\sigma \right\}. \quad (9.14)$$

Using  $R = 41.9$  nm and  $P = 8.5$  nm [Tab. 8.1], we numerically minimize  $\mathcal{F}_{\text{helical}}$  over  $r$  to compare it to  $\mathcal{F}_{\text{cylinder}}$ .

The minimization results in a relation between  $r$  and  $\sigma$  at mechanical equilibrium, which we plot in Fig. 9.2b. Since surface tension penalizes the membrane area,  $r$  decreases with increasing  $\sigma$ . As  $\sigma \rightarrow \infty$ , the scales of  $r$  and  $R$  separate ( $r \ll R$ ) and we recover the straight cylinder limit  $r = \sqrt{\kappa/2\sigma}$  [Lenz, 2010]. As  $\sigma \rightarrow 0$ ,  $r$  increases and saturates before the tube self-intersects, thanks to the corresponding divergence of the membrane bending energy [Eq. 9.12]. We can estimate the tension of helical tubes in the experiments  $\sigma_{\text{exp}}$  by pinpointing the experimental tubular radius  $r_{\text{exp}} = 12.1$  nm on the curve in Fig. 9.2b. We get  $\sigma_{\text{exp}} \simeq 6 \times 10^{-4}$  N/m (a fairly high tension for a membrane).

What is the critical tension  $\sigma_c$ ? To answer, we solve  $\mathcal{F}_{\text{helical}} = \mathcal{F}_{\text{cylinder}}$  numerically, at mechanical equilibrium. We get  $\sigma_c \simeq 2 \times 10^{-3}$  N/m. Since  $\sigma_{\text{exp}} < \sigma_c$ , the experimental tension is not high enough to justify the observation of helical tubes in the experiments.

## 9.2.2 Asymmetric membrane binding of polar and equatorial monomers

In the previous section, we implicitly assumed that the Snf7/Vps2/Vps24 helical scaffold binds equally well to straight and helical membrane tubes. Below, we argue that this may be an oversimplifying assumption, given the peculiar architecture of these polymers.

Why should the polymer-membrane interaction change going from straight to helical tubes? Snf7/Vps2/Vps24 helices are equipped with two membrane-binding interfaces [Sec. 8.2]. Depending on which of the two interfaces they use to bind helical tubes, we label them as either polar or equatorial. To clarify this aspect, in Fig. 8.2h we color in orange the polar interface and in light blue the equatorial one. Notice that engaging the membrane with the equatorial interface requires that the filament local normal  $\hat{n}$  and the surface local normal  $\hat{N}$  are parallel. Conversely, engaging the

membrane with the polar interface requires that  $\hat{n}$  and  $\hat{N}$  are perpendicular. The polar binding mode is thus exclusively accessible to Snf7/Vps2/Vps24 helices on helical tubes, while the equatorial mode can be used to bind both straight cylinders or helical tubes.

To account for the energy difference between binding modes, we introduce an energy gain  $-\mu$  per unit length of polar filament (*i.e.*,  $\mu > 0$  favors helical over straight tubes) to the free energy of helical tubes  $\mathcal{F}_{\text{helical}}$  used in Sec. 9.2.1. What is total length of polar filaments in our model? Since we have condensed 4 polar and 2 equatorial (double-stranded) filaments [Fig. 8.2h] onto a single helix of fixed length  $\mathcal{L}$ , the total length of polar filaments is  $4/(4+2) \times \mathcal{L} = 2/3 \times \mathcal{L}$ . We call  $\mathcal{F}_{\text{helical}}^{\mu}$  the upgraded free energy of helical tubes, that we write as

$$\frac{\mathcal{F}_{\text{helical}}^{\mu}}{\mathcal{L}} = \frac{\mathcal{F}_{\text{helical}}}{\mathcal{L}} - \frac{2}{3}\mu. \quad (9.15)$$

Before discussing the straight-to-helical tube transition, we illustrate how  $\mu$  is related to a binding energy difference per monomer.  $\mu$  is defined as an energy gain per unit length of model polar filament. How many real monomers are included in such a unit length? Our model helix accounts for four Snf7/Vps24/Vps2 polar filaments, each of which is double-stranded (*i.e.*, made of two sub-filaments) [Fig. 8.2h]. Therefore, each unit length of model helix accounts for  $4 \times 2 = 8$  real sub-filaments. From the experiments, we know that the typical monomer-monomer spacing within sub-filaments is 3 nm [Sec. 8.4], yielding a membrane-binding energy difference per monomer equal to  $\mu \times 1/8 \times 3$  nm.

The parameter regions where either straight or helical tubes are more stable are illustrated in Fig. 9.3. Differently than in the previous section, we find that helical tubes can be more favorable than straight ones at  $\sigma < \sigma_c$ , provided  $\mu$  is large enough. The thickness of helical tubes at the transition depends on  $\sigma$ , following the  $r = r(\sigma)$  relation derived in the previous section [Fig. 9.2b].

We can estimate the minimal  $\mu$  required for the stability of helical tubes with radius  $r_{\text{exp}} = 12.1$  nm [Tab. 8.1] by pinpointing the  $\mu_s^{\text{min}}$  value corresponding to  $\sigma_{\text{exp}}$  on the phase boundary [Fig. 9.3]. We get  $\mu \geq \mu_s^{\text{min}} = 26$  pN, which corresponds to a binding energy difference of  $2k_B T$  per monomer. This value is compatible with the previously estimated membrane-binding energy of Snf7 polymers alone, about  $4k_B T$  per monomer [Chiaruttini et al., 2015].

Interestingly the phase boundary curve has a maximum in proximity of  $\sigma = \sigma_{\text{exp}}$ . We readily make sense of this coincidence by giving a further look at the relation between the helical tube radius  $r$  and tension  $\sigma$  plotted in Fig. 9.2b. When  $\sigma \lesssim \sigma_{\text{exp}}$ ,  $r$  decreases slowly with increasing  $\sigma$ . The corresponding decrease in surface area cannot compensate for the increase of  $\sigma$ , making the surface energy of helical tubes increase with  $\sigma$  in that region. As a consequence, an increasingly higher  $\mu$  is required to transition, and the phase boundary curve increases with  $\sigma$ . When  $\sigma \gtrsim \sigma_{\text{exp}}$ ,  $r$  decreases more rapidly with increasing  $\sigma$ , shrinking the surface area enough to compensate for the increase of  $\sigma$  and making the surface energy of helical tubes decrease with  $\sigma$  in that region. Then, a decreasingly lower  $\mu$  is required to promote the transition, and the phase boundary curve decreases.

To conclude, a difference in membrane-binding energy between polar and equatorial filaments is required to justify the systematic observation of helical tubes in the experiments.

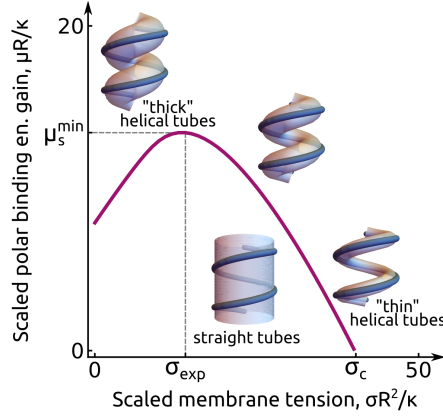


Figure 9.3: **Phase diagram of the straight-to-helical transition.** The solid purple line is the phase boundary.

### 9.3 Bending and torsional rigidities of ESCRT-III filaments

Compared to an isolated Snf7/Vps24/Vps2 helix, adding a membrane of known rigidity deforms the polymer into a larger helix [Tabs. 8.1, 8.2]. In this section, we use the magnitude of such deformation to infer the bending and torsional rigidities of the helix, as well as the difference in membrane binding energy between the polar and equatorial filaments.

The model used here is more detailed than the one of Sec. 9.2, and takes into account the flexibility of the filaments. In the model, a helical membrane tube is bound to two polar (red) and one equatorial (blue) model filaments [Fig. 9.4], such that every model filament accounts for two double-stranded Snf7/Vps24/Vps2 filaments [Fig. 8.2h]. The binding energy difference per unit length between the two types of filaments is denoted by  $\mu$ , as in Sec. 9.2.

Denoting the radius of the blue polymer by  $R$  and its pitch by  $2\pi P$ , the total length of red filaments is  $\mathcal{L}^R = 2 \times 2\pi n \sqrt{(R-r)^2 + P^2}$  and the length of the blue filaments is  $\mathcal{L}^B = 2\pi n \sqrt{R^2 + P^2}$ , where  $n$  denotes the number of turns around the vertical axis. We consider the most energetically favorable configuration of the system at fixed total polymer length  $\mathcal{L} = \mathcal{L}^R + \mathcal{L}^B$  and membrane area  $\mathcal{A}$ . Denoting by  $a = \mathcal{A}/\mathcal{L}$  the membrane surface area per unit polymer length, we use the expression of  $\mathcal{A}$  given in Eq. (9.9) to write

$$a = \frac{2\pi r \times 2\pi n \sqrt{(R-r)^2 + P^2}}{4\pi n \sqrt{(R-r)^2 + P^2} + 2\pi n \sqrt{R^2 + P^2}}, \quad (9.16)$$

which we invert to express the pitch  $2\pi P$  as

$$P = \left[ \frac{(2 - 2\pi r/a)^2 (R-r)^2 - R^2}{1 - (2 - 2\pi r/a)^2} \right]^{1/2}, \quad (9.17)$$

where  $r$  is the radius of the membrane tube.

The free energy of the system is the sum of a membrane and a polymer contribution:  $\mathcal{F} = \mathcal{F}_{\text{membrane}} + \mathcal{F}_{\text{polymer}}$ . The membrane free energy is given by Eq. (9.1), noting that the surface tension term only contributes a (physically irrelevant) constant to the free energy due to the constraint of fixed  $\mathcal{A}$ . We now write the polymer free

energy and then comment on its parameters and their numerical prefactors below,

$$\frac{\mathcal{F}_{\text{polymer}}}{\mathcal{L}} = \ell^R \left[ \frac{k_b}{2} (c^R - c_0^R)^2 + \frac{k_t}{2} (\tau^R - \tau_0^R)^2 - \frac{\mu}{2} \right] + \ell^B \left[ \frac{k_b/4}{2} (c^B - c_0^B)^2 + \frac{k_t}{2} (\tau^B - \tau_0^B)^2 \right]. \quad (9.18)$$

The superscripts  $R$  and  $B$  denote quantities related to red (polar) and blue (equatorial) filaments, respectively [Fig. 9.4]. Here  $\ell^R = \mathcal{L}^R/\mathcal{L}$ ,  $\ell^B = \mathcal{L}^B/\mathcal{L}$  and  $c_0 = R_0/(R_0^2 + P_0^2)$  and  $\tau_0 = P_0/(R_0^2 + P_0^2)$  denote the spontaneous curvature and torsion of the filaments, and are given by the radius  $R_0$  and pitch  $2\pi P_0$  of the tube-less helices [Tab. 8.2]. The values of curvature and torsion of the deformed filaments are given as

$$c^R = \frac{R - r}{(R - r)^2 + P^2}, \quad c^B = \frac{R}{R^2 + P^2}, \quad \tau^R = \frac{P}{(R - r)^2 + P^2} \quad \text{and} \quad \tau^B = \frac{P}{R^2 + P^2}. \quad (9.19)$$

The differential binding energy per unit length  $\mu$  is multiplied by  $1/2$ , so that its definition is the same as in Sec. 9.2, where one model filament accounted for four polar Snf7/Vps24/Vps2 double-stranded filaments, whereas here one model filament accounts for two double-stranded filaments. While both types of filaments have the same torsional stiffness  $k_t$ , in Eq. (9.18) the bending stiffness  $k_b$  of the red filaments is four times larger than that of the blue. Indeed, as we show in Fig. 8.2h, both red and blue filaments consist of two parallel sub-filaments of comparable thickness, but while red filaments bend along the sub-filaments' binding direction, blue filaments bend along the orthogonal direction. Just like it is much easier to bend a piece of cooked tagliatelle pasta in its thin than its thick direction, bending the red filaments is thus more costly than bending the blue ones. To express this notion quantitatively, we approximate each double-stranded filament as an elastic rod with a rectangular cross-section of aspect ratio equal to 2. Applying the classical result of Landau et al. [1986] this implies a ratio of bending stiffnesses of  $2^2 = 4$ .

We next express the conditions of mechanical equilibrium, which relate the helix' mechanical parameters with its observed dimensions. We thus insert Eqs. (9.17) and (9.19) into Eq. (9.18) to express the total free energy as a function of  $R$  and  $r$  only. The two force balance equations are

$$\frac{\partial \mathcal{F}}{\partial R} = 0, \quad (9.20a)$$

$$\frac{\partial \mathcal{F}}{\partial r} = 0. \quad (9.20b)$$

Finally, we insert the numerical values of  $R = 41.9$  nm,  $r = 12.1$  nm,  $R_0^B = 17.1$  nm,  $P_0^B = 8.9$  nm,  $R_0^R = 23.4$  nm and  $P_0^R = 6.6$  nm [Tab. 8.2], as well as  $a = 22.7$  nm obtained from Eq. (9.16) using  $P = 8.5$  nm [Tab. 8.1]. This results in a set of two equations relating the unknown parameters  $k_b$ ,  $k_t$  and  $\mu$ , which can be recast as:

$$\frac{k_b}{\kappa/c_0^R} = -1.14 + 0.30 \times \frac{\mu}{\kappa c_0^R} \quad (9.21a)$$

$$\frac{k_t}{\kappa/c_0^R} = -0.32 + 0.02 \times \frac{\mu}{\kappa c_0^R}. \quad (9.21b)$$

In Sec. 9.3.1, we infer lower bounds for the persistence length of Snf7/Vps2/Vps24 sub-filaments, as well as for the membrane-binding energy difference between polar and equatorial monomers, by enforcing the the positivity of the torsional stiffness  $k_t \geq 0$  in Eq. (9.21). In Sec. 9.3.2, we estimate the actual torsional stiffness of

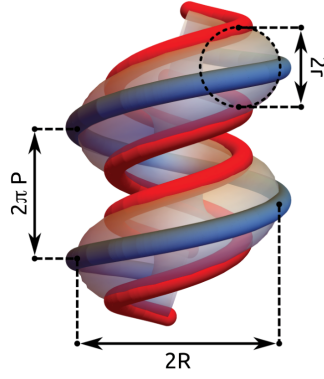


Figure 9.4: **Scheme of model used to estimate ESCRT-III bending and torsional rigidities.** A helical tube is stabilized by two polar (red) and one equatorial (blue) model filament. Polar helices have radius  $R - r$ . Both polar and equatorial helices have pitch  $2\pi P$ .

Snf7/Vps2/Vps24 sub-filaments, as well as the membrane-binding energy difference between polar and equatorial monomers, by assuming that the persistence length of Snf7/Vps2/Vps24 sub-filaments is that of Snf7 filaments, measured in previous experiments [Chiaruttini et al., 2015].

### 9.3.1 A lower bound for bending rigidity and membrane-binding asymmetry

Since mechanical stability of polymer helices requires  $k_t \geq 0$ , Eq. (9.21b) further implies that  $\mu > \mu_k^{\min} \simeq 52$  pN, corresponding to a differential binding energy per monomer bigger than  $\mu_k^{\min} \times 1/8 \times 3$  nm  $\simeq 5 k_B T$ . Since  $\mu_k^{\min} > \mu_s^{\min}$  [Sec. 9.2.2], helical tubes are more favorable than straight ones in the whole range of predicted rigidities.

Together with Eq. (9.21a), the condition  $\mu > \mu_k^{\min}$  also implies  $k_b > k_b^{\min} \simeq 8 \times 10^{-27}$  J · m. What bound does  $k_b^{\min}$  impose on the persistence length  $\ell_p$  for the of individual Snf7/Vps24/Vps2 sub-filaments? To answer this question, we note that  $k_b$  is the bending rigidity of a model equatorial filament, which accounts for two double-stranded Snf7/Vps24/Vps2 filaments [Figs. 9.4, 8.2h]. Hence, the bending stiffness of one double-stranded Snf7/Vps24/Vps2 filament is  $1/2 \times k_b$ . Notice that this is the bending stiffness of the filament along the binding direction of its two sub-filaments [Fig. 8.2h]. How is this bending stiffness related to that of one sub-filament? We assume that a double-stranded filament responds to bending like an elastic rod of rectangular section, with short side  $d$  and long side  $2d$ , such that its bending stiffness along its short side (*i.e.*, along the binding direction of its sub-filaments) is  $\propto (2d)^3 d / 12$  [Landau et al., 1986]. We further assume that sub-filaments respond to bending like isotropic rods of square section with side  $d$ , such that their bending stiffness is  $\propto d^4 / 12$  [Landau et al., 1986]. We get  $\ell_p \geq \ell_p^{\min}$ , with

$$\frac{\ell_p^{\min} \times k_B T}{k_b^{\min}} = \frac{d^4 / 12}{2 \times (2d)^3 d / 12} \quad (9.22)$$

from which  $\ell_p^{\min} \simeq 114$  nm. This value is compatible with a previous experimental estimate of the persistence length of Snf7 homopolymers,  $\ell_p^{\text{Snf7}} = 250$  nm [Chiaruttini

et al., 2015].

### 9.3.2 Realistic estimate of torsional rigidity and membrane-binding asymmetry

We now estimate the torsional stiffness of Snf7/Vps24/Vps2 sub-filaments, as well as the differential binding energy per monomer, by assuming that the persistence length of Snf7/Vps24/Vps2 sub-filaments is that of Snf7,  $\ell_p^{\text{Snf7}} = 250 \text{ nm}$  [Chiaruttini et al., 2015].

If sub-filaments have persistence length  $\ell_p^{\text{Snf7}}$ , Eq. (9.22) implies  $k_b = k_b^* = 16 \ell_p^{\text{Snf7}} k_B T$ . We call  $\mu^*$  the solution of Eq. (9.21a) for  $k_b = k_b^*$ , which yields a differential binding energy per monomer of  $\mu^* \times 1/8 \times 3 \text{ nm} \simeq 15 k_B T$ . This value is much larger than the membrane-binding energy of Snf7 alone, about  $4 k_B T$  per monomer [Chiaruttini et al., 2015], suggesting that Vps24 and Vps2 may be significant contributors of the binding of ESCRT-III filaments to lipid membranes.

We denote by  $k_t^*$  the solution of Eq. (9.21b) for  $\mu = \mu^*$ . How is  $k_t^*$  related to the torsional persistence length  $\ell_t$  of Snf7/Vps2/Vps24 sub-filaments? To answer this question, we note that  $k_t^*$  is the torsional rigidity of a model filament, which accounts for two double-stranded Snf7/Vps24/Vps2 real filaments [Figs. 9.4, 8.2h]. Hence, the torsional stiffness of one double-stranded real filament is  $1/2 \times k_t^*$ . How is this torsional stiffness related to that of one sub-filament? We assume that a double-stranded filament responds to torsion around its long axis like an elastic rod of rectangular section, with short side  $d$  and long side  $2d$ , such that its torsional stiffness is  $\propto \beta_2 (2d) d^3$  [Landau et al., 1986], with  $\beta_2 = 0.229$  [Ugural and Fenster, 2012]. We further assume that sub-filaments respond to torsion around their long axis like isotropic rods of square section with side  $d$ , such that their torsional stiffness is  $\propto \beta_1 d^4$  [Landau et al., 1986], with  $\beta_1 = 0.141$  [Ugural and Fenster, 2012]. We get

$$\frac{\ell_t \times k_B T}{k_b^*} = \frac{\beta_1 d^4}{2 \times \beta_2 (2d) d^3}, \quad (9.23)$$

yielding  $\ell_t \simeq 45 \text{ nm}$ . This value of torsional stiffness is comparable to that of DNA at low tension [Kriegel et al., 2017].

# Chapter 10

## Discussion

The key experimental finding presented here is that Vps24 and Vps2 endow initially flat Snf7 spirals with spontaneous torsion and two membrane binding interfaces [Secs. 8.2, 8.3]. The appearance of spontaneous torsion supports the Lenz et al. [2009] hypothesis that ESCRT-III tubulates membranes by growing out of plane [Fig. 7.3]. Moreover, Snf7/Vps2/Vps24 are systematically double-stranded in the experiments [Secs. 8.2, 8.3], making them possibly stiffer than Snf7 homopolymers and promoting membrane buckling via the curvature relaxation mechanism proposed by Lenz and coworkers.

The appearance of two membrane-binding interfaces upon Vps24 and Vps2 binding substantiates the membrane scission mechanism proposed by Šarić and coworkers [Harker-Kirschneck et al., 2019], in which the molecular origin of the hypothesized ESCRT-III transitions between different membrane-binding states was not clarified. Specifically, the assembly of Vps24 and Vps2 to Snf7 can be related to the flat  $\rightarrow$  out-of-plane transition, while their disassembly from Snf7, possibly mediated by Vps4, can be related to the out-of-plane  $\rightarrow$  flat transition.

The key theoretical finding is that there is a significant membrane binding energy difference between the two Snf7/Vps24/Vps2 interfaces, on which the stability of helical tubes relies [Sec. 9.2]. This energy difference (5 to  $15 k_B T$ ) is predicted to be larger than the membrane binding energy of Snf7 monomers alone ( $4 k_B T$ ), suggesting that Vps24 and Vps2 contribute significantly to ESCRT-III membrane adhesion [Sec. 9.3]. In the language of Harker-Kirschneck et al. [2019], the membrane-binding interface reminiscent of flat spirals, *i.e.*  $\alpha = 0^\circ$  in Fig. 7.4a, adheres to the membrane much better than the interface reminiscent of the  $\alpha = -90^\circ$  case. A similar energy difference between one interface at  $\alpha = 0^\circ$  and another at  $\alpha \geq 0^\circ$  may help severing membrane necks in the model of Šarić and coworkers, by favoring the out-of-plane  $\rightarrow$  flat transition and discouraging its reverse.

We derived the straight-to-helical tube phase diagram in Fig. 9.3 assuming that the membrane tube radius is constant along the membrane surface. For this reason, the radius of our straight cylinders is fixed to that of the undeformable scaffold and they have no way of reducing their surface. We thus neglected that the tube can modulate its radius along the vertical axis, as in Fig. 10.1a, in a way that keeps the membrane anchored to the helical scaffold. Such radial modulation can imply a reduction of the tube surface area, making it more stable at high membrane tension with respect to our estimate. Hence, we think that including this correction would increase  $\sigma_c$  and, consequently, stretch rightwards the phase boundary in the phase diagram [Fig. 9.3]. However, we do not think this would affect our conclusions, since the straight-to-tubular transition in the experiments happens at  $\sigma < \sigma_c$ , in a region of the phase

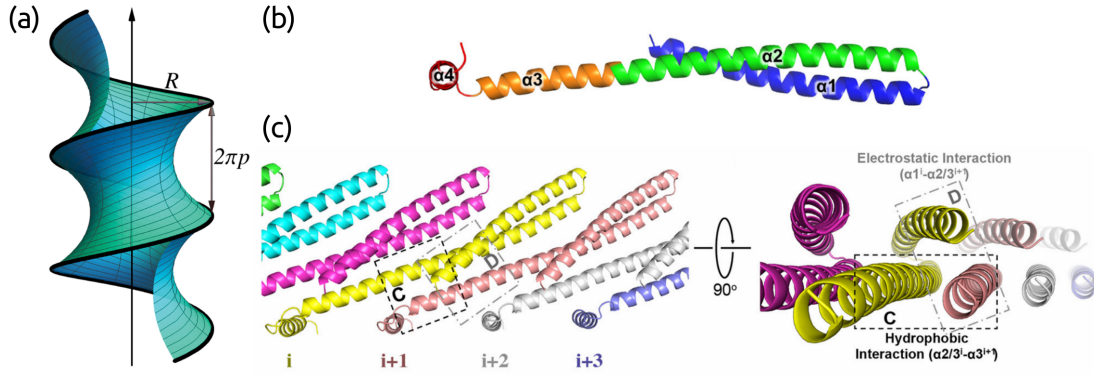


Figure 10.1: **Ribbon model of Snf7 homopolymers.** (a) Tube radius variations with helical symmetry in a straight membrane tube. *Reproduced from McDargh and Deserno [2018], with permission. © 2018 John Wiley & Sons A/S. Published by John Wiley & Sons Ltd* (b) Individual Snf7 protein. (c) Snf7 homopolymer architecture. Individual proteins drawn with different colors and labeled by the indices  $i, i + 1, \dots$ . One  $\alpha$ -helix from the protein  $i + 1$  (pink) interacts with two  $\alpha$ -helices from the protein  $i$  (yellow). *Figs. (b,c) reproduced from Tang et al. [2015], and licensed under CC BY 4.0.*

diagram that should be less sensitive to this correction.

We derived the bending and torsional stiffnesses of Snf7/Vps24/Vps2 sub-filaments by assuming they behave as elastic rods made of isotropic material. The isotropic material hypothesis implies that bending and torsional stiffnesses are related through the Poisson's ratio  $\sigma$ . In fact, given a rod with square section of side  $d$  made of isotropic material of Young's modulus  $E$  and shear modulus  $\mu$ , its bending and torsional stiffnesses are  $Ed^4/12$  and  $\mu\beta_1d^4$ , respectively [Landau et al., 1986; Ugural and Fenster, 2012]. Writing the bending and torsional stiffnesses in terms of the bending and torsional persistence lengths, *i.e.*  $\ell_p \times k_B T$  and  $\ell_t \times k_B T$ , we get  $E = 12/d^4 \times \ell_p \times k_B T$  and  $\mu = 1/(\beta_1 d^4) \times \ell_t \times k_B T$ . Furthermore, in isotropic materials,  $E$  and  $\mu$  satisfy [Landau et al., 1986]

$$E = 2\mu(1 + \sigma). \quad (10.1)$$

Plugging the relations obtained above for  $E$  and  $\mu$  in Eq. (10.1), using  $\ell_p = \ell_p^{\text{Snf7}}$  and  $\ell_t = 45 \text{ nm}$  [Sec. 9.3], we get that Snf7/Vps24/Vps2 heteropolymers have a Poisson's ratio  $\sigma \simeq 3.5$ , which is impossible since  $\sigma \in [-1; 1/2]$  due to mechanical stability conditions (namely, positivity of bulk and shear moduli) [Landau et al., 1986]. This is a clear sign that the internal structure of Snf7/Vps24/Vps2 heteropolymers is far from isotropic. Specifically, our estimate of their torsional stiffness is too small compared to the bending stiffness.

What could be the origin of the weak torsional rigidity of these polymers? It may be instructive to look at how monomers are interlocked in an ESCRT-III chain. Our most detailed knowledge on inter-monomer interactions comes from crystallographic studies on Snf7 [Tang et al., 2015]. The experiments suggest that the adhesion between two adjacent protein units relies on two pair-interactions between the  $\alpha$ -helix (pink) of one protein and two  $\alpha$ -helices (yellow) of the next one [Fig. 10.1c, right]. The two  $\alpha$ -helices belonging to the same protein do not have adhesive interactions along their length, but are hinged at one of their ends [Fig. 10.1b]. One could argue that only this intra-protein hinge responds to weak torsional deformations along the polymer

axis, the two inter-protein adhesive interactions being free to rotate around the polymer axis. Conversely, a weak bending deformation would tilt the interacting  $\alpha$ -helices relative to their preferred configuration, generating a possibly stronger response. In a future study, it would be interesting to put numbers into this argument and check whether this would actually lead to a difference between bending and torsional stiffness similar to what we find.

In postulating the free energy of membrane tubes, we neglected osmotic and hydrostatic pressure gradients through membrane bilayers. This choice is motivated by two experimental observations<sup>1</sup>. First, no significant difference in chemical composition is expected inside and outside membrane tubes. Even assuming there were such a difference at the early stages of helical tubes formation, measurements were taken after several hours of incubation, which should be enough for chemical potential equilibration inside and outside tubes. Second, a significant decrease in surface-to-volume ratio is observed during the formation of helical tubes, suggesting that water permeates the bilayers enough to rule out hydrostatic pressure gradients.

We modeled the straight-to-helical tube transition in the simplified case where the scaffolding function of multiple helical polymers is condensed into a single model filament. How does the transition picture change if the helical scaffold comprises multiple filaments? The ability of a multifilament scaffold to stabilize straight and helical tubes critically involves its filaments' spatial arrangement. A scaffold of helices that are homogeneously spaced along the vertical axis is suited for straight membrane tubes. Conversely, a scaffold of helices that are condensed into a helical ribbon is suited for both straight and helical membrane tubes [Fig. 10.2], and the relative stability of either shape depends on other factors, like membrane tension. We can thus predict a straight-to-helical tube transition driven by the spatial condensation of multiple scaffolding helical filaments, possibly due to thermal fluctuations. Notice that condensation requires that filaments' surface density be not too high, *i.e.* that filaments be few and their pitch-to-radius ratio be large enough. We are currently working on this theory, to extend our understanding of membrane tubes stabilized by helical filaments beyond the specific case of ESCRT-III. In fact, membrane helical tubes are observed also in ciliate mitochondria [Allen, 1995; Mühleip et al., 2016]. These helical tubes (*cristae*) are stabilized by a stiff helical scaffold of  $F_0F_1$  ATP-ase dimers, which are segregated on the outer surface of the tube (as in the bottom right panel of Fig. 10.2). In the same organism, straight membrane tubes are found in the contractile vacuole complex (CVC), this time stabilized by a stiff helical scaffold of  $V_0V_1$  ATP-ase dimers [Allen, 1995]. Differently than  $F_0F_1$  helices, which segregate on the membrane surface,  $V_0V_1$  helices homogeneously cover the membrane surface (as in the left panel of Fig. 10.2).

In conclusion, we inferred the membrane binding force of ESCRT-III from geometrical data on the shape of ESCRT-stabilized helical tubes. We contribute to the current debate on ESCRT-mediated membrane remodeling by proposing that Snf7/Vps24/Vps2 helices have two membrane-binding interfaces available to them, whose positioning on the polymers' surface allows them to engage membranes with previously unexpected curvatures. Furthermore, we make predictions on the asymmetric binding force of these two interfaces, as well as on the rigidities of Snf7/Vps24/Vps2 helices. We hope that the theoretical framework proposed here can help clarifying the mechanical stability of other helical and straight membrane tubes found in cells, like in ciliate mitochondria and in the contractile vacuole complex.

---

<sup>1</sup>Moser Von Filseck, private communication.

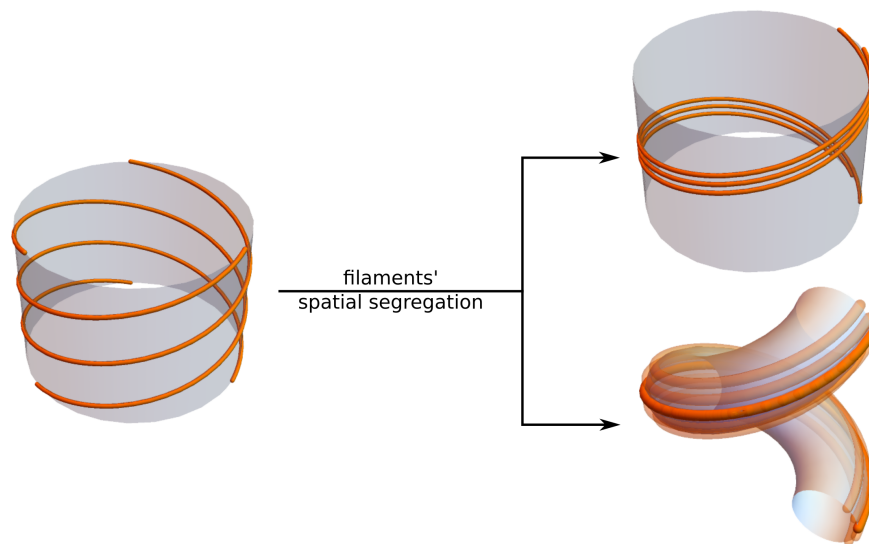


Figure 10.2: **Straight-to-helical transition from filaments' segregation.** Helical filaments can diffuse on the surface of a membrane tube. The more filaments' density is homogeneous, the more a straight tube is stable. If filaments spatially segregate, the straight tube can transition to a helical one depending on various factors. For instance, membrane tension would favor helical tubes, similarly to what we found in Sec. 9.2.

# Chapter 11

## Conclusion

In this thesis, we deduce inter-molecular forces from the elastic deformations they impose on biological matter. This method of investigation is well suited in those cases where forces can hardly be predicted from microscopic principles, due to their sensitivity to complicated chemical or physical factors. We focus on two such forces.

We start from the attractive force exerted by DNA helices onto each other in the presence of multivalent cations. Cation-mediated inter-helical attraction is key to compensate DNA bending stiffness when packing large amounts of DNA in comparatively small environments, such as the nuclei of sperm cells. The physical origin of inter-helical attractive forces is still under debate. Several theories were proposed to predict them, all of which suggest that helices need to properly align in order to optimize attraction. We infer inter-helical attractive forces from geometrical data on the distribution of DNA helices in dense toroidal bundles, which DNA spontaneously forms in the presence of multivalent cations, *in vitro*. The experiments show that the helical packing density decreases with increasing curvature.

We propose that toroidal curvature weakens inter-helical adhesion by making it harder for helices to optimize their lateral alignment. This idea is supported by further experimental evidence, showing that the average spatial correlation between neighboring DNA helices' grooves is different in small and giant toroids: in the first, the major grooves of each helix face the major grooves of its neighbors, whereas in the latter the major grooves of each helix face the minor grooves of its neighbors. Groove correlation between curved helices in DNA toroids is possible thanks to periodic variations in helical pitch along the backbone of each DNA helix, in which locally over- and under-twisted segments alternate each other.

To the best of our knowledge, the dependence of inter-helical adhesion on curvature was overlooked in previous studies, which mainly focused on the interaction between straight DNA helices. Since physiological DNA is often strongly curved, we think this aspect may be worth further investigation. To systematically investigate the interaction between DNA helices at varying curvature, a molecular dynamics simulation approach may prove the best tool. The emergence of pitch periodic modulation and its dependence on curvature may also be observed in such simulations. Progress in the understanding of periodic pitch modulation may also be done via a joint experimental and analytical approach. From the microscopy datasets used in this work, further image analysis should allow to extrapolate pitch modulation along DNA helices at varying local curvatures. We think the phenomenology of pitch modulation along DNA helices in toroidal bundles may be captured by a customized version of the Frenkel-Kontorova model of nonlinear physics.

We then turn to the binding force of a specific protein complex, ESCRT-III, to cellular membranes. ESCRT-III proteins polymerize into membrane-deforming polymers that are key to membrane neck severing from the lumen in all known biological processes requiring this kind of fission event, ranging from HIV budding to cytokinesis. Despite their ubiquity, it is still unclear how ESCRT-III polymers deform and sever membrane necks. *In vitro*, ESCRT-III helical polymers can reshape spherical vesicles into helical membrane tubes. We leverage geometrical data on helical tubes' shape to suggest that ESCRT-III polymers dispose of two separate membrane binding interfaces along their surface, whose positioning relative to the polymers' preferred direction of curvature allows to stabilize helical membrane tubes. We argue that the systematic shaping of helical tubular protrusions in the experiments is the result of a significant binding energy difference between the two interfaces, comparable to ESCRT-III polymers absolute membrane binding energy. Furthermore, we provide estimates for ESCRT-III polymers' bending and torsional stiffness.

Our findings support two previous models of ESCRT-mediated membrane remodeling. On the one hand, ESCRT-III polymers can form protrusions on the surface of lipid bilayers by growing out of plane, thanks to their spontaneously helical shape. On the other hand, ESCRT-III can engage membrane necks with different local curvatures thanks to their multiple membrane binding interfaces.

We think the theoretical framework developed to rationalize the stability of ESCRT-shaped helical tubes can be applied also to different cases in which membrane tubes are stabilized by helical filaments, such as the helical tubular cristae found in ciliate mitochondria or the straight tubules in the contractile vacuole complex.

In conclusion, throughout this thesis we tackle biological problems with a joint experimental and theoretical effort. We deduce forces and physical mechanisms that play important roles in cells by developing simple mechanical models. Our minimal theoretical approach allows us to keep track of causes and effects, as well as to untangle the intrinsic complexity of biological systems by focusing on just few physical ingredients at a time. Our models can easily be enriched and, in some cases, adapted to different biological systems. We hope our findings and suggestions will be helpful to other researchers in the field.

## Chapter 12

# Résumé de la thèse en français

Les assemblages biologiques doivent souvent leur stabilité et leur évolution à des forces intermoléculaires sur lesquelles nous avons peu de connaissances préalables. La principale difficulté dans la modélisation de ces forces est peut-être leur sensibilité à la composition chimique des molécules en interaction, ainsi qu'à celle de leur environnement. Cependant, le rôle biologique des forces intermoléculaires peut être dû à un petit nombre de leurs caractéristiques, qui émergent de la complexité chimique sous-jacente. Si ces forces sont impliquées de façon critique dans la déformation de la matière biologique, nous pouvons déduire ces caractéristiques en conciliant la géométrie de déformation avec des modèles mécaniques simples. Nous adoptons cette approche pour étudier deux de ces forces intermoléculaires.

Dans la première partie de la thèse, nous étudions les forces que les hélices d'ADN exercent les unes sur les autres (pour une introduction détaillée, voir le chapitre 2). L'ADN est un polymère chargé négativement [Fig. 1.1a], ce qui implique que ses unités ont tendance à se repousser mutuellement. Cependant, en présence de cations multivalents, des hélices d'ADN chargées négativement peuvent s'attirer mutuellement. L'attraction entre les hélices d'ADN est un phénomène fascinant, dont l'origine physique n'est pas encore complètement claire [voir le chapitre 3].

L'attraction entre les hélices est fondamentale pour compenser la résistance de l'ADN à la flexion lors du stockage de grandes quantités d'ADN dans des environnements relativement petits, tels que les noyaux des spermatozoïdes. En fait, le noyau d'un spermatozoïde humain peut être considéré comme une petite boîte, avec une taille linéaire de 5  $\mu\text{m}$  [Fig. 2.1a]. Cette boîte microscopique, qui pourrait tenir dix fois dans la largeur d'un cheveu humain, peut contenir une chaîne d'ADN longue de 1 m ! Chez les mammifères, les charges positives responsables de la condensation de l'ADN sont fournies par les *protamines*, protéines à haute contenu d'acides aminés chargés positivement. Chez l'homme, entre 85% et 95% de l'ADN est condensé par les *protamines*, et le reste du travail est laissé aux *histones* [Balhorn, 2007]. Il est intéressant de noter que la modification de la concentration de *protamines* est en corrélation avec l'infertilité chez la souris et l'homme, ce qui suggère que les *protamines* sont essentielles au bon fonctionnement des spermatozoïdes [Oliva, 2006].

Nous utilisons des données expérimentales sur la géométrie des condensats d'ADN pour déduire les propriétés des forces entre les hélices, médiées par les cations. Malheureusement, il est impossible d'obtenir des images à haute résolution des condensats d'ADN *in vivo*, car la densité physiologique de l'ADN dans les noyaux des cellules est trop élevée (voir, par exemple, Koehler 1966, 1970, 1972; Koehler et al. 1983) [Fig. 2.1b]. Par conséquent, nous utilisons les données de condensats d'ADN réalisés

*in vitro*. *In vitro*, on est libre de choisir parmi un ensemble d'agents condensateurs d'ADN, certains des plus couramment utilisés étant  $\text{Co}(\text{NH}_3)_6^{3+}$ , spermidine (3+), spermine (4+) et protamines [Laemmli, 1975; Chatteraj et al., 1978; Widom and Baldwin, 2004; Hud et al., 1993]. Il est intéressant de noter que, indépendamment de l'espèce de l'agent de condensation, l'ADN se condense généralement en faisceaux hexagonaux, qui peuvent être soit toroïdaux [Fig. 2.2] ou droits. Notre étude porte sur les faisceaux toroïdaux d'ADN condensés par la spermine (4+). Bien que nous ne sachions pas s'il existe des tores à ADN *in vivo* (par exemple, dans le noyau des spermatozoïdes) ils ont au moins deux caractéristiques en commun avec l'ADN physiologique : un emballage serré et une courbure. Par conséquent, nous pensons que nos résultats peuvent être transférés à des cas biologiquement pertinents.

Dans le chapitre 4, nous décrivons les expériences qui motivent notre étude théorique. Dans la section 4.1, nous présentons comment des toroïdes d'ADN de tailles variables peuvent être générés en utilisant des capsides de bactériophages. En particulier, de petits toroïdes peuvent être générés en laissant des molécules individuelles d'ADN se condenser à l'intérieur des capsides, tandis que des toroïdes géants peuvent être générés en laissant des nombreuses molécules d'ADN se condenser à l'extérieur des capsides. Dans la section 4.2, nous illustrons les caractéristiques géométriques connues des tores d'ADN qui ne dépendent pas de leur taille, notamment : l'emballage hexagonal des hélices d'ADN, leur rotation collective (torsion) autour de la ligne centrale du toroïde et la corrélation latérale entre les sillons des hélices voisines. Enfin, dans la section 4.3, nous présentons des mesures récentes concernant la dépendance de l'espacement entre hélices de la courbure des tores, réalisées par Amélie Leforestier et Françoise Livolant au LPS, à Orsay. Leur constatation principale est que, dans chaque tore, l'espacement entre les hélices subit une diminution d'environ 10% en allant du rayon intérieur vers le rayon extérieur du tore. De plus, elles observent que les petits tores sont, en moyenne, moins compactés que les tores géantes.

Nous étudions la corrélation entre la densité de compactage de l'ADN et la courbure des tores d'ADN. Notre intuition est que les variations d'espacement local sont liées à la réponse élastique locale de l'ADN. Plus précisément, la rigidité de l'ADN pénalise chaque région du tore proportionnellement à la courbure de l'ADN dont elle a besoin pour être peuplée. D'après des vues de dessus des tores, les hélices d'ADN semblent être disposées localement comme s'il s'agissait d'arcs de cercles concentriques, comme un fil de laine dans une pelote. Si cela était vrai, la courbure des hélices d'ADN diminuerait en allant de l'intérieur vers l'extérieur du tore. Cette géométrie supporterait notre intuition : les hélices d'ADN peuplent le moins les régions intérieures parce que leur courbure est plus élevée dans ces régions. Mais est-ce que la courbure de l'ADN diminue réellement en allant de l'intérieur vers l'extérieur du rayon, comme le suggèrent les vues de dessus ? Étant donné que les toroïdes d'ADN sont tordus, il est possible que la courbure ne soit pas aussi facilement répartie dans l'assemblage. Si la torsion est assez forte, il peut arriver même que l'ADN soit moins courbé près de l'intérieur que de l'extérieur du tore.

Dans le chapitre 5, nous développons notre modèle théorique. Dans la section 5.1, nous quantifions comment la courbure des filaments d'ADN est distribuée dans un tore, selon le taux de torsion de l'ADN autour de la ligne centrale du tore. Nous montrons que le taux de torsion expérimental est suffisamment faible pour supposer que les hélices d'ADN se comportent comme des cercles concentriques autour du centre du tore, *i.e.* que la courbure de l'ADN augmente avec la distance du rayon intérieur du tore. Dans la section 5.2, nous utilisons ce résultat pour développer un modèle

bidimensionnel minimal de tore d'ADN, à partir duquel nous étudions l'équilibre mécanique entre l'élasticité de l'ADN et les interactions entre les hélices. Dans la section 5.3, nous résolvons notre modèle et prédisons que l'espacement entre les hélices diminue avec la distance du rayon intérieur, en accord qualitatif avec les expériences. Dans la section 5.4, nous adaptons notre modèle aux données et déduisons le potentiel d'interaction locale entre les hélices d'ADN.

Dans le chapitre 6, nous discutons nos résultats et proposons des perspectives futures. Bien que notre modèle prévoie qualitativement la dépendance de l'espacement entre les hélices en fonction de la position dans chaque tore, il ne peut prévoir que les petits tores sont moins bien compactés que les grands tores. En fait, c'est le contraire de ce à quoi on pourrait s'attendre sur la seule base de l'élasticité, car les hélices sont plus courbées dans les petits tores que dans les tores géantes, et donc devraient se pousser l'un contre l'autre plus fort dans le premier que dans le dernier cas. Cela donne à penser que les interactions adhésives entre les hélices sont plus faibles chez les petits tores que chez les tores géants, *i.e.* que la courbure affaiblit l'adhésion entre les hélices.

Pourquoi la courbure devrait-elle affecter les forces entre les hélices ? Une molécule d'ADN a des charges négatives réparties le long de ses deux hélices de groupes phosphates. En raison de cette distribution de charge inhomogène, l'interaction entre deux molécules d'ADN parallèles dépend de la corrélation spatiale entre leurs sillons. Des images à haute résolution de faisceaux d'ADN condensés de spermine, obtenus par Leforestier and Livolant [2009], montrent que la courbure modifie la corrélation des sillons entre les hélices voisines [Fig. 2.3]. Dans les faisceaux droits, les sillons majeurs de chaque hélice sont orientés vers les sillons mineurs de ses voisines [Fig. 2.3b]. Par contre, dans les faisceaux toroïdaux, les sillons majeurs de chaque hélice sont orientés vers les sillons majeurs de ses voisines [Fig. 2.3a]. Nous pensons que cela certifie une influence non négligeable de la courbure sur les interactions entre hélices. Ensuite, puisque l'adhérence entre les hélices requiert des corrélations spécifiques entre les sillons, nous en déduisons que la courbure doit affecter leurs adhérence.

Notre étude ouvre la voie à plusieurs perspectives d'avenir. Par exemple, une étude systématique de la façon dont l'interaction entre deux hélices dépend de leur courbure devrait être possible en utilisant des simulations de dynamique moléculaire. Ces simulations pourraient également révéler comment les corrélations des sillons s'adaptent à la courbure. De plus, en ce qui concerne les corrélations entre les sillons, des progrès pourraient être réalisés en analysant les ensembles de données existants des vues de dessus des tores. Dans le passé, Leforestier and Livolant [2009] ont mesuré la variation du pas tout au long d'une hélice dans un tore. Le pas semblait subir des variations périodiques, montrant en alternance des segments hélicoïdaux sous-tordus et sur-tordus [Fig. 4.1i]. Cette mesure pourrait être répétée pour plusieurs hélices à différentes positions dans les tores, afin de mesurer comment une telle modulation périodique de pas dépend de la courbure locale. Nous nous attendons à ce que l'amplitude de la modulation diminue au fur et à mesure que la courbure diminue. Il devrait également être possible de rationaliser les modulations de pas induites par la courbure au moyen d'un modèle analytique minimal [voir le chapitre 6].

En conclusion, nous avons déduit des forces entre les hélices d'ADN, médiées par des cations multivalents, à partir de données géométriques sur des faisceaux toroïdaux d'ADN. Nous prédisons que la courbure affaiblit l'adhérence entre les hélices, ce qui peut se vérifier au niveau des condensats physiologiques d'ADN. Nous espérons que l'influence de la courbure sur les forces entre hélices sera abordée dans les études fu-

tures et que les progrès expérimentaux permettront de clarifier l'influence de la courbure sur les corrélations des sillons.

Dans la deuxième partie de la thèse, nous nous intéressons à la force de liaison d'un complexe protéique particulier, ESCRT-III, aux membranes cellulaires. Les protéines ESCRT-III s'assemblent en polymères qui rétrécissent le diamètre des cols de membrane, en agissant dans leur volume interne. A notre connaissance, ESCRT-III est impliqué dans tous les processus biologiques connus qui nécessitent un tel événement de fission membranaire, allant de la libération du VIH de la membrane plasmique à la constriction du pont cytokinétique pendant la division cellulaire (pour une introduction détaillée, voir le chapitre 7). Malgré leur omniprésence, on ne sait toujours pas comment les polymères ESCRT-III déforment et coupent le col des membranes.

Dans le chapitre 8, nous présentons des expériences qui prouvent des capacités inattendues de liaison entre l'ESCRT-III et les membranes. Ces résultats ont été obtenus par Joachim Moser Von Filseck et Aurélien Roux à l'Université de Genève, en collaboration avec Nathaniel Talledge, Isabel Johnson et Adam Frost de l'University of California San Francisco. Leur constatation principale est que trois unités ESCRT-III : Snf7, Vps24 et Vps2 se copolymérisent en hélices qui stabilisent des tubes de membrane hélicoïdaux en se liant à leur couche lipidique externe [Fig. 8.1g, 8.1i]. Par souci de simplicité, nous désignons ces polymères par le terme générique Snf7/Vps24/Vps2. Cependant, nous ne pouvons exclure que les différents polymères de l'échantillon aient une stoechiométrie différente. Malheureusement, ces informations ne sont pas accessibles à partir des expériences présentées ici.

Dans la section 8.1, nous montrons les tubes hélicoïdaux dans lesquels les vésicules membranaires sont déformées sous l'action des hélices Snf7/Vps24/Vps2. Dans la section 8.2, nous montrons que les filaments Snf7/Vps24/Vps2 sont à double brin et se trouvent à la surface externe des tubes hélicoïdaux. De plus, nous illustrons que ces filaments se regroupent en trois groupes, ce qui suggère qu'ils sont équipés de deux interfaces de liaison membranaire différentes et peuvent être divisés en deux ensembles, appelés *polaire* et *équatorial*. Enfin, dans la section 8.3, nous montrons la configuration de repos des hélices Snf7/Vps24/Vps2 lorsqu'elles sont produites en absence de tubes de membrane, qui peuvent être solubilisées par un détergent.

Dans le passé, il a été observé que les polymères hélicoïdaux ESCRT-III ne formaient que des protubérances tubulaires droites à la surface des vésicules. Les tubes hélicoïdaux constituent une forme inhabituelle pour les membranes, car ils coûtent plus cher en énergie de courbure par rapport aux protubérances tubulaires relativement droites qui ont été observées dans les expériences précédentes. Cependant, les hélices Snf7/Vps24/Vps2 ne forment jamais des tubes de membrane droits. Pourquoi ? Nous abordons cette question dans le chapitre 9.

Tout d'abord, dans la section 9.1, nous dérivons quelques résultats sur la géométrie différentielle des tubes hélicoïdaux qui sont utilisés dans la suite du chapitre.

Pourquoi les hélices Snf7/Vps24/Vps2 forment-elles systématiquement des tubes de membrane hélicoïdaux plutôt que droits ? Dans la section 9.2, nous proposons que la réalisation expérimentale de tubes exclusivement hélicoïdaux puisse être expliquée sur la base d'une énergie de liaison membranaire asymétrique des filaments polaires et équatoriaux [section 8.2]. Nous en déduisons un diagramme de phase, dans lequel la stabilité relative des tubes droits et hélicoïdaux supportés par des hélices rigides Snf7/Vps24/Vps2 est comparée. A partir du diagramme de phase, nous déduisons une limite inférieure sur la différence d'énergie de liaison membranaire par monomère entre les filaments polaires et équatoriaux.

Quelle est la rigidité des hélices Snf7/Vps2/Vps24 ? Dans la section 9.3, nous répondons à cette question en développant un modèle élastique dans lequel un tube hélicoïdal est stabilisé par un échafaudage flexible d'hélices polaires et équatoriales Snf7/Vps24/Vps2. En connaissant de ces expériences combien les hélices Snf7/Vps24/Vps2 s'écartent de leur configuration de repos lorsqu'elles stabilisent des tubes hélicoïdaux, nous estimons une limite inférieure sur la rigidité des hélices à partir des équations d'équilibre des forces. De plus, en utilisant une estimation précédente de la rigidité, nous estimons la rigidité en torsion des hélices Snf7/Vps24/Vps2, ainsi que la différence en énergie de liaison à la membrane entre monomères polaires et équatoriaux.

Dans le chapitre 10, nous discutons nos résultats et proposons des perspectives futures. La principale conclusion théorique est qu'il existe une différence d'énergie de liaison membranaire significative entre les deux interfaces des hélices Snf7/Vps24/Vps2, sur laquelle se fonde la stabilité des tubes hélicoïdaux [section 9.2]. Cette différence d'énergie (entre 5 et 15  $k_B T$ ) est plus grande que l'énergie de liaison membranaire des monomères Snf7 seuls (4  $k_B T$ , Chiaruttini et al. 2015), ce qui suggère que Vps24 et Vps2 contribuent considérablement à l'adhésion des membranes ESCRT-III [section 9.3].

Nous avons modélisé la transition du tube droit au tube hélicoïdal dans le cas simplifié où la fonction d'échafaudage de plusieurs polymères hélicoïdaux est condensée en un seul filament. Comment la transition change-t-elle si l'échafaudage hélicoïdal comporte plusieurs filaments ? La capacité d'un échafaudage composé de plusieurs filaments à stabiliser des tubes droits et hélicoïdaux est liée de façon critique à l'arrangement spatial des filaments sur la surface des tubes. Un échafaudage d'hélices espacées de manière homogène le long de l'axe vertical convient aux tubes de membranes droits [Fig. 10.2]. Inversement, un échafaudage d'hélices condensées en un ruban hélicoïdal convient aussi bien aux tubes de membrane droits qu'hélicoïdaux, et la stabilité relative des deux formes dépend d'autres facteurs, comme la tension de la membrane. On peut donc prédire une transition du tube droit à hélicoïdal entraînée par la condensation spatiale de multiples filaments hélicoïdaux de l'échafaudage, ce qui peut être dû à des fluctuations thermiques. Il faut noter que la condensation exige que la densité de surface des filaments ne soit pas trop élevée, *i.e.* que les filaments soient peu nombreux et que leur rapport pas/rayon soit assez grand. Nous sommes en train de travailler sur cette théorie, afin d'étendre notre compréhension des tubes de membrane stabilisés par des filaments hélicoïdaux au-delà du cas spécifique de l'ESCRT-III. En fait, les tubes hélicoïdaux de membrane sont également observés dans les mitochondries ciliées [Allen, 1995; Mühleip et al., 2016]. Ces tubes hélicoïdaux (*crystae*) sont stabilisés par un échafaudage hélicoïdal rigide de dimères de ATPases  $F_0F_1$  qui sont disposés sur la surface extérieure des tubes (comme dans la partie inférieure droite du schéma de la figure 10.2). Dans le même organisme, on trouve des tubes à membrane droite dans le complexe vacuolaire contractile (CVC), cette fois-ci stabilisé par un échafaudage hélicoïdal rigide de dimères de ATPases  $V_0V_1$  [Allen, 1995]. Contrairement aux hélices  $F_0F_1$ , qui recouvrent de façon pas homogène la surface des tubes, les hélices  $V_0V_1$  recouvrent de façon homogène la surface (comme dans le panneau gauche de la figure 10.2).

En conclusion, dans cette partie de la thèse nous déduisons la force de liaison entre ESCRT-III et membrane à partir de données géométriques sur la forme des tubes hélicoïdaux stabilisés par l'ESCRT. Nous contribuons au débat actuel sur le remodelage des membranes à médiation ESCRT en proposant que les hélices Snf7/Vps24/Vps2 disposent de deux interfaces de liaison membranaire, dont le positionnement à la sur-

face des polymères leur permet d'engager des membranes avec des courbures inattendues auparavant. De plus, nous faisons des prédictions sur la force de liaison asymétrique de ces deux interfaces, ainsi que sur les rigidités des hélices Snf7/Vps24/Vps2. Nous espérons que le cadre théorique proposé ici pourra aider à clarifier la stabilité mécanique d'autres tubes de membrane, hélicoïdaux et droits, présents dans les cellules, comme dans les mitochondries ciliées et dans le complexe vacuole contractile.

Tout au long de cette thèse, nous abordons des problèmes biologiques avec un effort expérimental et théorique conjoint. Nous déduisons des forces et des mécanismes physiques qui jouent des rôles importants dans les cellules en développant des modèles mécaniques simples. Notre approche théorique minimale nous permet de cerner les causes et les effets, ainsi que de démêler la complexité intrinsèque des systèmes biologiques en nous concentrant sur un petit nombre d'ingrédients physiques en même temps. Nos modèles peuvent facilement être enrichis et, dans certains cas, adaptés à différents systèmes biologiques. Nous espérons que nos conclusions et nos suggestions seront utiles à d'autres chercheurs dans ce domaine.

# Bibliography

- R. D. Allen. Membrane tubulation and proton pumps. *Protoplasma*, 189:1–8, 1995. ISSN 0006-3568. doi: 10.1007/bf01280286.
- B. N. Ames and D. T. Dubin. The role of polyamines in the neutralization of bacteriophage deoxyribonucleic acid. *The Journal of biological chemistry*, 235(3):769–775, 1960. ISSN 00219258.
- B. N. Ames, D. T. Dubin, and S. M. Rosenthal. Observations on flea transfer between hosts; a mechanism in the spread of bubonic plague. *Science*, 127(3302):814, 1958. ISSN 00368075. doi: 10.1126/science.127.3302.814.
- D. W. Atkinson, C. D. Santangelo, and G. M. Grason. Constant spacing in filament bundles. *New Journal of Physics*, 21(6):062001, 2019. doi: 10.1088/1367-2630/ab1c2d.
- M. Babst, D. J. Katzmann, E. J. Estepa-Sabal, T. Meerloo, and S. D. Emr. ESCRT-III: An endosome-associated heterooligomeric protein complex required for MVB sorting. *Developmental Cell*, 3(2):271–282, 2002. ISSN 15345807. doi: 10.1016/S1534-5807(02)00220-4.
- R. Balhorn. The protamine family of sperm nuclear proteins. *Genome Biology*, 8(9), 2007. ISSN 14747596. doi: 10.1186/gb-2007-8-9-227.
- S. Banjade, S. Tang, Y. H. Shah, and S. D. Emr. Electrostatic lateral interactions drive ESCRT-III heteropolymer assembly. *eLife*, 8(2015):1–25, 2019. doi: 10.7554/elife.46207.
- K. Besteman, K. Van Eijk, and S. G. Lemay. Charge inversion accompanies DNA condensation by multivalent ions. *Nature Physics*, 3(9):641–644, 2007. ISSN 17452481. doi: 10.1038/nphys697.
- A. G. Cashikar, S. Shim, R. Roth, M. R. Maldazys, J. E. Heuser, and P. I. Hanson. Structure of cellular ESCRT-III spirals and their relationship to HIV budding. *eLife*, 3: 1–17, 2014. ISSN 2050084X. doi: 10.7554/eLife.02184.
- M. Cha, S. Ro, and Y. W. Kim. Rodlike Counterions near Charged Cylinders: Counterion Condensation and Intercylinder Interaction. *Physical Review Letters*, 121(5): 58001, 2018. ISSN 10797114. doi: 10.1103/PhysRevLett.121.058001.
- P. M. Chaikin and T. C. Lubensky. *Principles of condensed matter physics*. Cambridge University Press, Cambridge, 1995. ISBN 9780511813467. doi: 10.1017/CBO9780511813467.

- D. K. Chattoraj, L. C. Gosule, and J. A. Schellman. DNA condensation with polyamines. II. Electron microscopic studies. *Journal of Molecular Biology*, 121(3): 327–337, 1978. ISSN 00222836. doi: 10.1016/0022-2836(78)90367-4.
- A. G. Cherstvy. DNA cholesteric phases: The role of DNA molecular chirality and DNA-DNA electrostatic interactions. *Journal of Physical Chemistry B*, 112(40):12585–12595, 2008. ISSN 15206106. doi: 10.1021/jp801220p.
- N. Chiaruttini and A. Roux. Dynamic and elastic shape transitions in curved ESCRT-III filaments. *Current Opinion in Cell Biology*, 47:126–135, 2017. ISSN 18790410. doi: 10.1016/j.ceb.2017.07.002.
- N. Chiaruttini, L. Redondo-Morata, A. Colom, F. Humbert, M. Lenz, S. Scheuring, and A. Roux. Relaxation of Loaded ESCRT-III Spiral Springs Drives Membrane Deformation. *Cell*, 163(4):866–879, 2015. ISSN 10974172. doi: 10.1016/j.cell.2015.10.017.
- L. Christ, C. Raiborg, E. M. Wenzel, C. Campsteijn, and H. Stenmark. Cellular Functions and Molecular Mechanisms of the ESCRT Membrane-Scission Machinery. *Trends in Biochemical Sciences*, 42(1):42–56, 2017. ISSN 13624326. doi: 10.1016/j.tibs.2016.08.016.
- A. C. Cowley, N. L. Fuller, and V. A. Parsegian. Measurement of Repulsive Forces between Charged Phospholipid Bilayers. *Biochemistry*, 17(15):3163–3168, 1978. ISSN 15204995. doi: 10.1021/bi00608a034.
- M. De Frutos, S. Brasiles, P. Tavares, and E. Raspaud. Effect of spermine and DNase on DNA release from bacteriophage T5. *European Physical Journal E*, 17(4):429–434, 2005. ISSN 12928941. doi: 10.1140/epje/i2005-10019-5.
- M. Egli. Review DNA-Cation Interactions: Quo Vadis? of selected papers in the field since 1997 in chronologi. *Chemistry & Biology*, 9(02):277–286, 2002. ISSN 10745521. doi: 10.1016/S1074-5521(02)00116-3.
- A. Evilevitch, L. Lavelle, C. M. Knobler, E. Raspaud, and W. M. Gelbart. Osmotic pressure inhibition of DNA ejection from phage. *Proceedings of the National Academy of Sciences*, 100(16):9292–9295, 2003. ISSN 0027-8424. doi: 10.1073/pnas.1233721100.
- G. M. Grason. Colloquium: Geometry and optimal packing of twisted columns and filaments. *Reviews of Modern Physics*, 87(2):401–419, 2015. ISSN 15390756. doi: 10.1103/RevModPhys.87.401.
- N. Grønbech-Jensen, R. J. Mashl, R. F. Bruinsma, and W. M. Gelbart. Counterion-induced attraction between rigid polyelectrolytes. *Physical Review Letters*, 78(12): 2477–2480, 1997. ISSN 10797114. doi: 10.1103/PhysRevLett.78.2477.
- S. Guilbaud, L. Salomé, N. Destainville, M. Manghi, and C. Tardin. Dependence of DNA Persistence Length on Ionic Strength and Ion Type. *Physical Review Letters*, 122(2):1–6, 2019. ISSN 10797114. doi: 10.1103/PhysRevLett.122.028102.
- J. Guizetti, L. Schermelleh, J. Mantler, S. Maar, I. Poser, H. Leonhardt, T. Muller-Reichert, and D. W. Gerlich. Cortical constriction during abscission involves helices of ESCRT-III-dependent filaments. *Science*, 331(6024):1616–1620, 2011. ISSN 00368075. doi: 10.1126/science.1201847.

- P. I. Hanson, R. Roth, Y. Lin, and J. E. Heuser. Plasma membrane deformation by circular arrays of ESCRT-III protein filaments. *Journal of Cell Biology*, 180(2):389–402, 2008. ISSN 00219525. doi: 10.1083/jcb.200707031.
- L. Harker-Kirschneck, B. Baum, and A. Saric. Transitions in filament geometry drive ESCRT-III-mediated membrane remodelling and fission. *bioRxiv*, 2019. doi: 10.1101/559898.
- W. Helfrich. Elastic Properties of Lipid Bilayers: Theory and Possible Experiments. *Zeitschrift für Naturforschung*, 28 c:693 – 703, 1973.
- W. M. Henne, N. J. Buchkovich, Y. Zhao, and S. D. Emr. The endosomal sorting complex ESCRT-II mediates the assembly and architecture of ESCRT-III helices. *Cell*, 151(2):356–371, 2012. ISSN 00928674. doi: 10.1016/j.cell.2012.08.039.
- N. V. Hud, M. J. Allen, K. H. Downing, and J. Lee. Identification of the elemental packing unit of DNA in mammalian sperm cells by AFM. *Biochemical and Biophysical Research Communications*, 193(3):1347–1354, 1993.
- Y. W. Kim, J. Yi, and P. A. Pincus. Attractions between Like-Charged Surfaces with Dumbbell-Shaped Counterions. *Physical Review Letters*, 101(20):1–4, 2008. ISSN 00319007. doi: 10.1103/PhysRevLett.101.208305.
- J. K. Koehler. Fine structure observations in frozen-etched bovine spermatozoa. *Journal of Ultrastructure Research*, 16(3-4):359–375, 1966. ISSN 00225320. doi: 10.1016/S0022-5320(66)80068-0.
- J. K. Koehler. A Freeze-Etching Study of Rabbit Spermatozoa with Particular Reference to Head Structures 1. *Journal of Ultrastructure Research*, 33:598–614, 1970.
- J. K. Koehler. Human sperm head ultrastructure: A freeze-etching study. *Journal of Ultrastructure Research*, 39(5-6):520–539, 1972. ISSN 00225320. doi: 10.1016/S0022-5320(72)90118-9.
- J. K. Koehler, U. Würschmidt, and M. P. Larsen. Nuclear and chromatin structure in rat spermatozoa. *Gamete Research*, 8(4):357–370, 1983. ISSN 15543919. doi: 10.1002/mrd.1120080406.
- V. Koning, B. C. Van Zuiden, R. D. Kamien, and V. Vitelli. Saddle-splay screening and chiral symmetry breaking in toroidal nematics. *Soft Matter*, 10(23):4192–4198, 2014. ISSN 17446848. doi: 10.1039/c4sm00076e.
- A. A. Kornyshev and S. Leikin. Fluctuation theory of hydration forces: The dramatic effects of inhomogeneous boundary conditions. *Physical Review A*, 40(11):6431–6437, 1989. ISSN 10502947. doi: 10.1103/PhysRevA.40.6431.
- A. A. Kornyshev and S. Leikin. Theory of interaction between helical molecules. *The Journal of Chemical Physics*, 107(9):3656–3674, 1997. ISSN 0021-9606. doi: 10.1063/1.475320.
- A. A. Kornyshev and S. Leikin. Electrostatic zipper motif for DNA aggregation. *Physical Review Letters*, 82(20):4138–4141, 1999. ISSN 10797114. doi: 10.1103/PhysRevLett.82.4138.
- E. Kreyszig. *Differential geometry*. Dover Publications, 1991. ISBN 0486318621.

- F. Kriegel, N. Ermann, R. Forbes, D. Dulin, N. H. Dekker, and J. Lipfert. Probing the salt dependence of the torsional stiffness of DNA by multiplexed magnetic torque tweezers. *Nucleic Acids Research*, 45(10):5920–5929, 2017. ISSN 13624962. doi: 10.1093/nar/gkx280.
- I. M. Kulić, D. Andrienko, and M. Deserno. Twist-bend instability for toroidal DNA condensates. *Europhysics Letters*, 67(3):418–424, 2004. ISSN 02955075. doi: 10.1209/epl/i2004-10076-x.
- U. K. Laemmli. Characterization of DNA condensates induced by poly ( ethylene oxide ) and polylysine. *Biochemistry*, 72(11):4288–4292, 1975.
- O. Lambert, L. Letellier, W. M. Gelbart, and J.-L. Rigaud. DNA delivery by phage as a strategy for encapsulating toroidal condensates of arbitrary size into liposomes. *Proceedings of the National Academy of Sciences*, 97(13):7248–7253, 2000. ISSN 0027-8424. doi: 10.1073/pnas.130187297.
- L. D. Landau, E. M. Lifshitz, A. M. Kosevich, and L. P. Pitaevskii. *Theory of elasticity*. Butterworth-Heinemann, 1986. ISBN 9780750626330.
- S. Lata, G. Schoehn, A. Jain, R. Pires, J. Piehler, H. G. Gottlinger, and W. Weissenhorn. Helical structures of ESCRT-III are disassembled by VPS4. *Science*, 321(5894):1354–1357, 2008. ISSN 00368075. doi: 10.1126/science.1161070.
- A. Leforestier and F. Livolant. Structure of toroidal DNA collapsed inside the phage capsid. *Proceedings of the National Academy of Sciences*, 106(23):9157–9162, 2009. ISSN 0027-8424. doi: 10.1073/pnas.0901240106.
- S. Leikin, V. A. Parsegian, D. C. Rau, and R. P. Rand. Hydration Forces. *Annual Review of Physical Chemistry*, 44(1):369–395, 1993. ISSN 0066426X. doi: 10.1146/annurev.physchem.44.1.369.
- D. M. Leneveu, R. P. Rand, and V. A. Parsegian. Measurement of forces between lecithin bilayers. *Nature*, 259(5544):601–603, 1976. ISSN 00280836. doi: 10.1038/259601a0.
- M. Lenz. *Shaping tubes in cells*. PhD thesis, Université Pierre et Marie Curie - Paris VI, 2010. URL <https://tel.archives-ouvertes.fr/tel-00541655Submitted>.
- M. Lenz, D. J. Crow, and J. F. Joanny. Membrane Buckling Induced by Curved Filaments. *Physical Review Letters*, 103(3):1–4, 2009. ISSN 00319007. doi: 10.1103/PhysRevLett.103.038101.
- Y. Levin. Electrostatic correlations: From plasma to biology. *Reports on Progress in Physics*, 65(11):1577–1632, 2002. ISSN 00344885. doi: 10.1088/0034-4885/65/11/201.
- M. Mandelkern, J. G. Elias, D. Eden, and D. M. Crothers. The dimensions of DNA in solution. *Journal of Molecular Biology*, 152(1):153–161, 1981. ISSN 00222836. doi: 10.1016/0022-2836(81)90099-1.
- G. S. Manning. Limiting laws and counterion condensation in polyelectrolyte solutions I. Colligative properties. *The Journal of Chemical Physics*, 51(3):924–933, 1969. ISSN 00219606. doi: 10.1063/1.1672157.

- S. Marčelja and N. Radić. Repulsion of interfaces due to boundary water. *Chemical Physics Letters*, 32(1):129–130, 1976.
- J. McCullough, A. K. Clippinger, N. Talledge, M. L. Skowrya, M. G. Saunders, T. V. Naismith, L. A. Colf, P. Afonine, C. Arthur, W. I. Sundquist, P. I. Hanson, and A. Frost. Structure and membrane remodeling activity of ESCRT-III helical polymers. *Science*, 350(6267):1548–1551, 2015. ISSN 10959203. doi: 10.1126/science.aad8305.
- Z. A. McDargh and M. Deserno. Dynamin’s helical geometry does not destabilize membranes during fission. *Traffic*, 19(5):328–335, 2018. ISSN 16000854. doi: 10.1111/tra.12555.
- T. J. McIntosh, A. D. Magid, and S. A. Simon. Repulsive interactions between uncharged bilayers. Hydration and fluctuation pressures for monoglycerides. *Biophysical Journal*, 55(5):897–904, 1989. ISSN 00063495. doi: 10.1016/S0006-3495(89)82888-7.
- B. E. Mierzwa, N. Chiaruttini, L. Redondo-Morata, J. Moser Von Filseck, J. König, J. Larios, I. Poser, T. Müller-Reichert, S. Scheuring, A. Roux, and D. W. Gerlich. Dynamic subunit turnover in ESCRT-III assemblies is regulated by Vps4 to mediate membrane remodelling during cytokinesis. *Nature Cell Biology*, 19(7):787–798, 2017. ISSN 14764679. doi: 10.1038/ncb3559.
- J. Moser Von Filseck, L. Barberi, N. Talledge, I. Johnson, A. Frost, M. Lenz, and A. Roux. Anisotropic ESCRT-III architecture governs helical membrane tube formation. *bioRxiv*, page 716308, jul 2019. doi: 10.1101/716308.
- A. W. Mühleip, F. Joos, C. Wigge, A. S. Frangakis, W. Kühlbrandt, and K. M. Davies. Helical arrays of U-shaped ATP synthase dimers form tubular cristae in ciliate mitochondria. *Proceedings of the National Academy of Sciences of the United States of America*, 113(30):8442–8447, jul 2016. ISSN 10916490. doi: 10.1073/pnas.1525430113.
- A. Najj, M. Kanduč, J. Forsman, and R. Podgornik. Perspective: Coulomb fluids - Weak coupling, strong coupling, in between and beyond. *Journal of Chemical Physics*, 139(15), 2013. ISSN 00219606. doi: 10.1063/1.4824681.
- T. T. Nguyen, I. Rouzina, and B. I. Shklovskii. Reentrant condensation of DNA induced by multivalent counterions. *Journal of Chemical Physics*, 112(5):2562–2568, 2000. ISSN 00219606. doi: 10.1063/1.480819.
- T. Odijk and F. Slok. Nonuniform Donnan Equilibrium within Bacteriophages Packed with DNA. *The Journal of Physical Chemistry B*, 107(32):8074–8077, aug 2003. ISSN 1520-6106. doi: 10.1021/jp0224822.
- R. Oliva. Protamines and male infertility. *Human Reproduction Update*, 12(4):417–435, 2006. ISSN 13554786. doi: 10.1093/humupd/dml009.
- F. Oosawa. Interaction between parallel rodlike macroions. *Biopolymers*, 6(11):1633–1647, 1968. ISSN 10970282. doi: 10.1002/bip.1968.360061108.
- A.-K. Pfitzner, V. Mercier, and A. Roux. Vps4 triggers sequential subunit exchange in ESCRT-III polymers that drives membrane constriction and fission. *bioRxiv Biochemistry*, 2019. doi: 10.1101/718080.

- R. Phillips, J. Kondev, J. Theriot, and H. G. Garcia. *Physical Biology of the Cell*. Garland Science, Taylor & Francis Group, New York, 2 edition, 2012. ISBN 9783540773405.
- R. Podgornik and V. A. Parsegian. Charge-fluctuation forces between rodlike polyelectrolytes: Pairwise summability reexamined. *Physical Review Letters*, 80(7):1560–1563, 1998. ISSN 10797114. doi: 10.1103/PhysRevLett.80.1560.
- R. Podgornik, H. H. Strey, K. Gawrisch, D. C. Rau, A. Rupprecht, and V. A. Parsegian. Bond orientational order, molecular motion, and free energy of high-density DNA mesophases. 93(April):4261–4266, 1996.
- R. P. Rand and V. A. Parsegian. Hydration forces between phospholipid bilayers. *BBA - Reviews on Biomembranes*, 988(3):351–376, 1989. ISSN 03044157. doi: 10.1016/0304-4157(89)90010-5.
- R. P. Rand, N. Fuller, V. A. Parsegian, and D. C. Rau. Variation in Hydration Forces between Neutral Phospholipid Bilayers: Evidence for Hydration Attraction. *Biochemistry*, 27(20):7711–7722, 1988. ISSN 15204995. doi: 10.1021/bi00420a021.
- E. Raspaud, D. Durand, and F. Livolant. Interhelical spacing in liquid crystalline spermine and spermidine-DNA precipitates. *Biophysical Journal*, 88(1):392–403, 2005. ISSN 00063495. doi: 10.1529/biophysj.104.040113.
- D. C. Rau and V. A. Parsegian. Direct measurement of the intermolecular forces between counterion-condensed DNA double helices. Evidence for long range attractive hydration forces. *Biophysical Journal*, 61(1):246–259, 1992a. ISSN 00063495. doi: 10.1016/S0006-3495(92)81831-3.
- D. C. Rau and V. A. Parsegian. Direct measurement of temperature-dependent solvation forces between DNA double helices. *Biophysical Journal*, 61:260–271, 1992b.
- D. C. Rau, B. Lee, and V. A. Parsegian. Measurement of the repulsive force between polyelectrolyte molecules in ionic solution: Hydration forces between parallel DNA double helices. *Proceedings of the National Academy of Sciences of the United States of America*, 81(9 I):2621–2625, 1984. ISSN 00278424. doi: 10.1073/pnas.81.9.2621.
- I. Rouzina and V. A. Bloomfield. Macroion attraction due to electrostatic correlation between screening counterions. 1. Mobile surface-adsorbed ions and diffuse ion cloud. *Journal of Physical Chemistry*, 100(23):9977–9989, 1996. ISSN 00223654. doi: 10.1021/jp960458g.
- S. Saksena, J. Wahlman, D. Teis, A. E. Johnson, and S. D. Emr. Functional Reconstitution of ESCRT-III Assembly and Disassembly. *Cell*, 136(1):97–109, 2009. ISSN 00928674. doi: 10.1016/j.cell.2008.11.013.
- A. Schellman and N. Parthasarathy. X-ray Diffraction Studies on Cation-collapsed DNA. *Journal of Molecular Biology*, 175(3):313–329, 1984.
- J. Schöneberg, I. H. Lee, J. H. Iwasa, and J. H. Hurley. Reverse-topology membrane scission by the ESCRT proteins. *Nature Reviews Molecular Cell Biology*, 18(1):5–17, 2016. ISSN 14710080. doi: 10.1038/nrm.2016.121.
- Q. T. Shen, A. L. Schuh, Y. Zheng, K. Quinney, L. Wang, M. Hanna, J. C. Mitchell, M. S. Otegui, P. Ahlquist, Q. Cui, and A. Audhya. Structural analysis and modeling

- reveals new mechanisms governing ESCRT-III spiral filament assembly. *Journal of Cell Biology*, 206(6):763–777, 2014. ISSN 15408140. doi: 10.1083/jcb.201403108.
- B. I. Shklovskii. Wigner crystal model of counterion induced bundle formation of rodlike polyelectrolytes. *Physical Review Letters*, 82(16):3268–3271, 1999a. ISSN 10797114. doi: 10.1103/PhysRevLett.82.3268.
- B. I. Shklovskii. Screening of a macroion by multivalent ions: Correlation-induced inversion of charge. *Physical Review E - Statistical Physics, Plasmas, Fluids, and Related Interdisciplinary Topics*, 60(5):5802–5811, 1999b. ISSN 1063651X. doi: 10.1103/PhysRevE.60.5802.
- D. E. Smith, S. J. Tans, S. B. Smith, S. Grimes, D. L. Anderson, and C. Bustamante. The bacteriophage phis29 portal motor can package DNA against a large internal force. *Nature*, 413(6857):748–752, 2001. ISSN 0028-0836. doi: 10.1038/413748A0.
- C. W. Tabor and H. Tabor. Polyamines in microorganisms. *Microbiological Reviews*, 49(1):81–99, 1985. ISSN 01460749.
- S. Tang, W. M. Henne, P. P. Borbat, N. J. Buchkovich, J. H. Freed, Y. Mao, J. C. Fromme, and S. D. Emr. Structural basis for activation, assembly and membrane binding of ESCRT-III Snf7 filaments. *eLife*, 4(DECEMBER2015):1–22, 2015. ISSN 2050084X. doi: 10.7554/eLife.12548.
- D. Teis, S. Saksena, B. L. Judson, and S. D. Emr. ESCRT-II coordinates the assembly of ESCRT-III filaments for cargo sorting and multivesicular body vesicle formation. *The EMBO Journal*, 29:871–883, 2010. doi: 10.1038/emboj.2009.408.
- B. A. Todd, V. A. Parsegian, A. Shirahata, T. J. Thomas, and D. C. Rau. Attractive forces between cation condensed DNA double helices. *Biophysical Journal*, 94(12):4775–4782, 2008. ISSN 15420086. doi: 10.1529/biophysj.107.127332.
- C. Tongu, T. Kenmotsu, Y. Yoshikawa, A. Zinchenko, N. Chen, and K. Yoshikawa. Divalent cation shrinks DNA but inhibits its compaction with trivalent cation. *Journal of Chemical Physics*, 144(20), may 2016. ISSN 00219606. doi: 10.1063/1.4950749.
- E. Trizac and G. Téllez. Onsager-manning-oosawa condensation phenomenon and the effect of salt. *Physical Review Letters*, 96(3):1–4, 2006. ISSN 10797114. doi: 10.1103/PhysRevLett.96.038302.
- A. C. Ugural and S. K. Fenster. *Advanced mechanics of materials and applied elasticity*. Prentice Hall, 2012. ISBN 0137079206.
- J. J. Widom and R. L. Baldwin. Cation-induced toroidal condensation of DNA. *Journal of Molecular Biology*, 144(4):431–453, 2004. ISSN 00222836. doi: 10.1016/0022-2836(80)90330-7.
- E. Wigner. On the interaction of electrons in metals. *Physical Review*, 46(11):1002–1011, 1934. ISSN 0031899X. doi: 10.1103/PhysRev.46.1002.
- D. C. Wright and N. D. Mermin. Crystalline liquids: The blue phases. *Reviews of Modern Physics*, 61(2):385–432, 1989. ISSN 00346861. doi: 10.1103/RevModPhys.61.385.

- Y. Xie, K. F. Ludwig, G. Morales, D. E. Hare, and C. M. Sorensen. Noncritical behavior of density fluctuations in supercooled water. *Physical Review Letters*, 71(13):2050–2053, 1993. ISSN 00319007. doi: 10.1103/PhysRevLett.71.2050.
- J. Yoo and A. Aksimentiev. The structure and intermolecular forces of DNA condensates. *Nucleic Acids Research*, 44(5):2036–2046, 2016. ISSN 13624962. doi: 10.1093/nar/gkw081.
- J. Zavadlav, R. Podgornik, and M. Praprotnik. Order and interactions in DNA arrays: Multiscale molecular dynamics simulation. *Scientific Reports*, 7(1):1–11, 2017. ISSN 20452322. doi: 10.1038/s41598-017-05109-2.

**Titre: Dédire les forces à partir de la géométrie en biologie**

**Mots clés: ADN, ESCRT-III, Membrane, Élasticité, Biophysique**

**Résumé:** Des forces intermoléculaires sur lesquelles nous avons peu de connaissances préalables sont souvent essentielles à la stabilité et à l'évolution des assemblages biologiques. Dans cette thèse, nous nous concentrons sur deux de ces forces qui sont impliquées de façon critique dans la déformation soit des biopolymères, soit des membranes. Nous déduisons ces forces en conciliant la géométrie d'une telle déformation avec des modèles mécaniques simples. Dans la première partie de la thèse, nous examinons la force d'attraction entre les molécules d'ADN médiées par des cations multivalents. Cette attraction est nécessaire pour compenser la rigidité de l'ADN lors du confinement de grandes quantités d'ADN dans des environnements relativement petits, tels que les noyaux des spermatozoïdes. In vitro, les cations multivalents causent la condensation de l'ADN en faisceaux toroïdaux denses. Grâce à des données sur la géométrie de ces faisceaux, nous pouvons étudier la compétition entre les forces at-

tractives et la rigidité de l'ADN. Nous inférons telles forces et proposons que la courbure toroïdale affaiblit l'adhésion entre les molécules d'ADN. Dans la deuxième partie de la thèse, nous nous intéressons à la force de liaison d'un complexe protéique de remodelage membranaire, ESCRT-III, aux membranes cellulaires. Les protéines ESCRT-III s'assemblent en polymères qui remodelent la membrane au cours de nombreux processus cellulaires, allant du bourgeonnement du VIH à la cytokinèse. Le mécanisme par lequel les polymères ESCRT-III déforment les membranes n'est toujours pas clair. In vitro, les polymères ESCRT-III peuvent transformer des vésicules membranaires sphériques en tubes hélicoïdaux. Nous proposons que les tubes hélicoïdaux résultent du positionnement particulier des sites de liaison membranaire sur la surface des polymères ESCRT-III. De plus, nous déduisons la force de liaison entre les monomères ESCRT-III et la membrane à partir de la géométrie des tubes hélicoïdaux.

**Title: Inferring forces from geometry in biology**

**Keywords: DNA, ESCRT-III, Membrane, Elasticity, Biophysics**

**Abstract:** Inter-molecular forces on which we have poor prior knowledge are often essential for the stability and evolution of biological assemblies. In this thesis, we focus on two such forces that are critically involved in the deformation of either biopolymers or membranes. We infer these forces by reconciling the geometry of such deformation with simple mechanical models. In the first part of the thesis, we consider the attractive force between DNA molecules mediated by multivalent cations. This attraction is required to compensate DNA bending rigidity when packaging large quantities of DNA in comparatively small environments, such as the nuclei of sperm cells. In vitro, multivalent cations drive DNA condensation into dense toroidal bundles. Geometrical data on DNA toroidal bundles give access to the competition between inter-helical attraction and DNA bending rigid-

ity. From these data, we infer inter-helical forces and argue that the toroid curvature weakens the adhesion between DNA molecules. In the second part of the thesis, we turn to the binding force of a membrane remodeling protein complex, ESCRT-III, to cellular membranes. ESCRT-III proteins assemble into membrane-remodeling polymers during many cellular processes, ranging from HIV budding to cytokinesis. The mechanism by which ESCRT-III polymers deform membranes is still unclear. In vitro, ESCRT-III polymers can reshape spherical membrane vesicles into helical tubes. We argue that helical tubes result from the peculiar positioning of membrane-binding sites on the surface of ESCRT-III polymers. Furthermore, we infer the binding force between ESCRT-III and membrane from the geometry of helical tubes.

